Wing Kinematics and Flexibility for Optimal Manoeuvring and Escape

by

Jaime Gustav Wong

A thesis submitted to the
Department of Mechanical and Materials Engineering
in conformity with the requirements for
the degree of Doctor of Philosophy

Queen's University
Kingston, Ontario, Canada
July 2017

Copyright © Jaime Gustav Wong, 2017

Abstract

Understanding how animals control the dynamic stall vortices in their wake is critical to developing micro-aerial vehicles and autonomous underwater vehicles, not to mention wind turbines, delta wings, and rotor craft that undergo similar dynamic stall processes. Applying this knowledge to biomimetic engineering problems requires progress in three areas: (i) understanding the flow physics of natural swimmers and flyers; (ii) developing flow measurement techniques to resolve this physics; and (iii) deriving low-cost models suitable for studying the vast parameter space observed in nature. This body of work, which consists of five research chapters, focuses on the leading-edge vortex (LEV) that forms on profiles undergoing rapid manoeuvres, delta wings, and similar devices. Lagrangian particle tracking is used throughout this thesis to track the mass and circulation transport in the LEV on manoeuvring profiles. The growth and development of the LEV is studied in relation to: flapping and plunging profile kinematics; spanwise flow from profile sweep and spanwise profile bending; and varying the angle-of-attack gradient along the profile span. Finally, scaling relationships derived from the observations above are used to develop a low-cost model for LEV growth, that is validated on a flat-plate delta wing. Together these results contribute to each of the three topics identified above, as a step towards developing robust, agile biomimetic swimmers and flyers.

Co-Authorship

Chapters 2-6 of this thesis consist of multi-authored works. Two have been published, while two have been submitted for publication and the last is in preparation for submission. The contributions of each co-author is listed below.

1. Wong, Jaime G. and Rival, David E. (2015) Determining the relative stability of leading-edge vortices on nominally two-dimensional flapping profiles. *Journal of Fluid Mechanics*. 766:611-625

The Cambridge University Press (UK) is the copyright holder. However permission to reproduce the article is retained following the transfer of copyright:

> *You* [the author] *may reproduce the article or an adapted version of it in any volume of which you are editor or author subject to normal acknowledgement.*

Dr. Rival contributed through helpful discussions and meetings, and in revisions and editing. I conducted the experiments, modelling and data treatment, and wrote the body text.

2. Wong, Jaime G. and Rival, David E. (2017) Rapid manoeuvring with spanwise-flexible wings. *Journal of Fluids and Structures*. (In press)

As the article is not published my co-author and I are the copyright holders. Dr. Rival contributed through helpful discussions and meetings, and in revisions and editing. I conducted the experiments, modelling and data treatment, and wrote the body text.

3. Wong, Jaime G., laBastide, Benen P. and Rival, David E. (2017) Flow separation on flapping and rotating profiles with spanwise gradients. *Bioinspiration & Biomimetics*. 12:026008

The Institute of Physics (UK) is the copyright holder. However permission to reproduce the article is retained following the transfer of copyright:

...To include the Article (all or part) in a research thesis or dissertation...

Mr. laBastide and I conducted experiments and data treatment together. Dr. Rival supervised the work, while I conducted all modelling work and wrote the body text.

4. Wong, Jaime G., Rosi, Giuseppe A., Rouhi, Amirreza and Rival, David E. (2017) Coupling Temporal and Spatial Gradient Information in High-Density Unstructured Lagrangian Measurements. *Experiments in Fluids*. (In revision)

As the article is not published my co-authors and I are the copyright holders. Dr. Rosi and I conducted the experiments and data treatment together. Dr. Rouhi provided the numerical data set, and contributed the section describing the numerical methods. Dr. Rival supervised the work, while I derived the methodology presented in the work and wrote the body text with the exception above.

5. Wong, Jaime G., Gillespie, Graeme and Rival, David E. (2017) Modelling Circulation Redistribution in Leading-Edge Vortices with Spanwise Flow. *AIAA Journal* (In preparation)

As the article is not published my co-authors and I are the copyright holders. Dr. Rival contributed through helpful discussions and meetings, and in revisions and editing. Mr. Gillespie and I conducted experiments and data treatment together, while I developed the model and wrote the body text.

Acknowledgments

Just as it is said that it takes a village to raise a child, that only my own name appears at the front of this thesis is an injustice to each of my friends, family, and colleagues (three groups with surprising overlap) who have supported me throughout this work.

An immense debt of gratitude is owed to Dr. David Rival, whose tutelage has shaped not only the work found herein, but also my personal philosophy as an academic at the start of my career. I am aware that I did not fit the typical profile for graduate studies, and I appreciate that taking me on as a student was a risk.

Every topic in this field that was not introduced to me by Dr. Rival was probably introduced to me by Dr. Jochen Kriegseis, who has gradually transitioned from teacher to friend and colleague. For this I am grateful.

To John Fernando and Giuseppe Rosi: I cannot imagine the past six years without your friendship, assistance and encouragement. I am proud to have grown with you, to have learned with you, and to have shared this experience with you.

A very special thanks is owed to Elizabeth Stanley, for her unwaivering patience. For all of my friends and family, who have supported me since before this chapter began and who will remain there for me well after this chapter is over, here's to making up for lost time.

To my late father, for introducing me to science, mathematics and engineering.

Contents

Abstract **i**

Co-Authorship **ii**

Acknowledgments **iv**

Contents **v**

List of Tables **viii**

List of Figures **ix**

List of Abbreviations, Acronyms and Symbols **xxiv**

Chapter 1: Introduction **1**

1.1 The aerodynamic and hydrodynamic performance of natural flyers and swimmers 2

1.1.1 Evolutionary convergence in flexibility, profile shape and stroke amplitude 3

1.1.2 Variations in flow topology between manoeuvring and cruising 7

1.1.3 The role of the circulation budget in determining wing kinematics and shape 9

1.2 Engineering applications of the flow physics of natural swimming and flight 10

1.2.1 The performance of engineered vehicles at comparable Reynolds numbers 12

1.2.2 Limitations of current engineering applications 14

1.3 Contributions of the Current Thesis 17

Chapter 2: Determining the Relative Stability of Leading-Edge Vortices on Nominally Two-Dimensional Flapping Profiles **21**

2.1 Abstract 21

2.2 Introduction 22
2.3 The Moderation of LEV Growth with Vorticity Transport 24
2.3.1 The Effect of Reduced Frequency on LEV Saturation 25
2.3.2 The Effect of Vorticity Convection on LEV Circulation 28
2.3.3 The Effect of Vortex Stretching on LEV Cross-Sectional Area 28
2.4 Methods 29
2.4.1 Parameter Space 31
2.4.2 PIV Setup 32
2.4.3 3D-PTV Setup 34
2.5 Results 35
2.5.1 The Effect of the Modified Strouhal Number and Reduced Frequency on Vortex Development 35
2.5.2 The Effect of Vorticity Transport on Vortex Development . . . 36
2.6 Discussion 41
2.7 Conclusions 43
2.8 Acknowledgements 43

Chapter 3: Rapid manoeuvring with spanwise-flexible wings 44
3.1 Abstract 44
3.2 Introduction 45
3.3 Methods 49
3.4 Results 56
3.5 Discussion 59
3.6 Conclusions 60
3.7 Acknowledgements 61

Chapter 4: Flow separation on flapping and rotating profiles with spanwise gradients 62
4.1 Abstract 62
4.2 Introduction 63
4.3 Background 66
4.4 Methods 70
4.5 Results 75
4.6 Conclusions 80
4.7 Acknowledgements 82

Chapter 5: Coupling Temporal and Spatial Gradient Information in High-Density Unstructured Lagrangian Measurements 83
5.1 Abstract 83
5.2 Introduction 84
5.3 Gradient Optimization Methodology 87

5.4 Numerical Test Case: Dissipating Taylor-Green Vortex 91
5.4.1 Computational Methodology 92
5.4.2 Results: Proposed Method Operating on the Dissipating Taylor-Green Vortex 94
5.5 Experimental Test Case: Starting Vortex on an Accelerating Circular Plate 98
5.5.1 Experimental Apparatus and Image-Processing Methodology . 98
5.5.2 High-Fidelity Measurements of the Starting Vortex Growth . . 100
5.6 Conclusions 103

Chapter 6: Modelling Circulation Redistribution in Leading-Edge Vortices with Spanwise Flow 105
6.1 Abstract 105
6.2 Introduction 106
6.3 A One-Dimensional Monte-Carlo Simulation of Circulation Transport 109
6.3.1 Shear-Layer Feeding 109
6.3.2 Spanwise Circulation Transport 112
6.4 Experimental Methods 115
6.4.1 High-Speed Shear-Layer Measurements 116
6.4.2 Spanwise-Resolved Circulation advection Measurements 117
6.5 Results and Discussion 119
6.5.1 Shear-layer flux 119
6.5.2 Spanwise Flow and Circulation Redistribution 121
6.6 Conclusions 124
6.7 Acknowledgements 126

Chapter 7: Synthesis 127
7.1 Wing Shape and Kinematics as Flow Control 128
7.2 Analysing Unsteady Separated Flows 130
7.3 Applications Outside of Biomimetic Locomotion 131
7.4 Outlook 132
7.5 Closing remarks 133

Bibliography 134

Appendix A: The non-dimensionalization of Euler-Bernoulli beam theory and typical examples 150

Appendix B: Comparing Optical Measurement Techniques 156

List of Tables

6.1 Circulation, circulation transport, and shear layer properties for a flat plate delta wing are estimated with a low-cost Monte Carlo simulation. The results of that simulation are compared here to 4D-PTV measurements for the case of a non-slender flat-plate delta wing. . . . 123

A.1 Structural properties of several insect species, organized by order: dragonflies, lacewings, bees and wasps, flies, and butterflies and moths. . . 153

B.1 Physical parameters of the optical measurement techniques used in this thesis. 157

List of Figures

1.1 The *Great Flight Diagram* demonstrates scaling of flying machines, engineered and natural, follow L^3 over twelve orders of magnitude. Taken from Tennekes (2009). 4

1.2 Relative forearm length of five bird species: (a) Calliope hummingbird; (b) Rock dove; (c) Blue grouse; (d) European starling; (e) Laysan albatross. Taken from Dial (1992). 6

1.3 The LEV, shown here as the spiralling blue pattern of streamlines, is continuously fed vorticity-containing mass from the leading-edge shear layer. Despite this injection of both circulation and mass, many LEVs remain at a constant strength and size on rotating wings. 10

1.4 Mass is fed into an LEV through the leading-edge shear layer, carrying with it vorticity ω_z. In order for the LEV to be stationary, both the vorticity and mass entering the LEV must be balanced either by vorticity annihilation or spanwise circulation transport. The spanwise flow w shown here facilitates that balance by convecting vorticity along the span. 11

1.5 A vortex street is shed from a D-cylinder upstream of an euthanized trout. The body flexibility of this trout is able to extract sufficient energy from this oscillating flow field to swim upstream against drag. Taken from Beal et al. (2006). 13

1.6 Chapters 2, 4 and 3 of this thesis contribute to understanding biological propulsion phenomenologically. This phenomenological understanding is used to develop low-cost models presented in Chapters 2 and 6. The high-resolution measurement techniques used for such studies are advanced in Chapters 5 and 6. 18

2.1 A flat-plate profile undergoing a flapping motion has a spanwise variation in effective velocity and spanwise flow, resulting in vortex stretching ($\omega_z(\partial w/\partial z)$) and vorticity convection ($w(\partial \omega_z/\partial z)$). The balance between the spanwise transport of vorticity and vorticity flux through the leading-edge shear layer is hypothesized here as the mechanism of LEV stability. 25

2.2 The integration of vorticity within a shear-layer segment of length l and thickness d. For a fluid of density ρ, this results in a rate of circulation growth $\frac{\partial \Gamma}{\partial t} = \frac{\partial \Gamma}{\partial m'}\frac{\partial m'}{\partial t}$ of approximately the square of effective velocity u_{eff}^2. 27

2.3 The prescribed velocity of the flat-plate profiles follow three sections: a sinusoidal ramp-up from zero velocity to maximum velocity over a period t_r; a constant velocity section over a period t_c; and a sinusoidal ramp-down over a period t_r. The duration of the constant-velocity section is varied in order to vary Strouhal number. 31

2.4 The $k - St^*$ parameter space for the current study. The $k - St$ parameter space of the two-dimensional study by Baik et al. (2012) is superimposed for comparison. The first stage of this study is to determine when three-dimensional effects begin to dominate vortex growth. 33

2.5 Swept and unswept flat-plate profiles (A) manoeuvre through the cylindrical PTV control volume of length $l = 200mm$ and diameter $d = 80mm$. The volume is illuminated with the aid of a mirror (B) reflecting light upstream from a HID lightsource collimated with 40mm and 300mm lenses (C). Also shown are the four pco.Edge sCMOS cameras (D) and the hexapod manipulator (E). The mirror (B) was moved upstream relative to the real experimental setup for the purposes of this photo. 35

2.6 Vortex-core locations were determined with the $|\gamma_1|$ criterion and tracked through time, shown here for all modified Strouhal numbers St^* and reduced frequencies k tested, at the phase $t/T = 0.5$. The modified Strouhal number does not effect vortex convection speed. 37

2.7 Vortex locations are tracked, relative to $t/T = 0.1$, showing a collapse of LEV displacement as a function of reduced frequency k (left). Vortex circulation is affected by both modified Strouhal number St^* and reduced frequency k: larger k results in a lower circulation Γ; sensitivity to St^* is low until $St^* = 0.54$, at which point dramatic increases in circulation are observed (right). 38

2.8 Isosurfaces of vorticity magnitude ($\omega c/U_\infty = 5$, 10, and 20) are shown for phase $t/T = 0.5$ in the left column, and isosurfaces of vorticity convection ($w\frac{\partial \omega_z}{\partial z}\frac{c^2}{U_\infty^2} = 20$, 50, and 100) are shown in the right column. From top to bottom the four cases shown are: $k = 0.89,\ \Lambda = 0°$; $k = 1.33,\ \Lambda = 0°$; $k = 0.89,\ \Lambda = 45°$; and $k = 1.33,\ \Lambda = 45°$. 39

2.9 Spanwise flow, vortex circulation, vorticity transport and vortex location are plotted for four test cases. Streamwise vortex position shows a large dependence on both sweep angle and reduced frequency. This sensitivity to reduced frequency can be explained in terms of the limiting length scale of the profile chord for stable LEV growth. 40

3.1 A two-dimensional plunging wing provides a reference with which to compare tip-leading and tip-lagging kinematics (grey). It is hypothesized that a tip-leading motion directs vorticity convection towards the wing root, reducing LEV stability (red). Meanwhile, a tip-lagging case is expected to direct vorticity convection away from the wing root, improving LEV stability by balancing the circulation generated at the leading-edge (blue). Here, U_∞ is the free-stream velocity, while v is a vertical velocity from plunging of flapping motions at points along the span 1 and 2. 48

3.2 The angle of attack experienced at the tip of a flexible profile has a phase-lead or lag relative to the root, as well as a change in magnitude (left). The effective incidence at the root and the tip, shown in blue and red, respectively, can be recorded (centre). By carefully combining pitching and plunging motions, the same angle-of-attack history can be prescribed onto the root and tip of a rigid wing through combined pitching and flapping (right). 51

3.3 (left) The modelled motion consisted of a common effective incidence α_{eff} at the root for all three cases (black). Meanwhile, the modelled deformation resulted in a different effective incidence history at the profile tip for the tip-leading case (red) and tip lagging case (blue). (right) This effective incidence history resulted in a common pitching angle α_{geo} (black) for all three cases, and flapping angles θ for the tip-leading (red) and tip lagging (blue) cases as shown. 53

3.4 (a) A pitching-flapping mechanism (I) was use to actuate the NACA0012 profile (II) as it was towed along the 15m-long optical towing tank (b). Pitching and flapping axes are labeled ϕ and θ, respectively. The flow-field around the profile was illuminated from the side-wall with a high-speed laser, and was subsequently captured with a four-camera 4D-PTV setup (III), which was located below the glass floor. 54

3.5 Three snapshots centred about $s/c = 1.5$ of highly-rotational tracked particles are highlighted here with the gamma criterion for the tip-leading case (red, left), two-dimensional reference case (grey, centre), and tip-lagging case (blue, right), respectively. All low-vorticity particles are removed for clarity. The tip-lagging case, similar to kinematics found in nature, exhibits a compact LEV closer to the profile surface than either of the other cases. As a faster-growing LEV is likely to reach the limiting $1c$ length-scale earlier, this indicates that it will not remain attached for as long into the motion. 56

3.6 Vortex circulation is highest for the tip-leading case, and lowest for the tip-lagging case, similar to the results seen for the cross-sectional vortex area. 58

3.7 Vorticity convection is large and negative for tip-leading kinematics. Meanwhile, vortex stretching has the same sign for both tip-leading and tip-lagging kinematics. Therefore, as the flexible cases differ from the two-dimensional case in opposite ways, the two cases cannot be differentiated through vortex stretching. 58

4.1 The angle of attack change is shown here for a flapping wing case (left) and a rotor case experiencing a gust (right). The angle of attack change on a flapping wing grows towards the tip of the profile, whereas the angle of attack change for a rotor with gust is greatest towards the root. 64

4.2 The angle-of-attack (α) change is shown for both the rotor case and the flapping case (left). A change in the axial velocity (gust) ΔU has an opposite effect on the angle-of-attack distribution for a rotor compared to the distribution formed from a flapping motion. An example of the spanwise distribution of angle-of-attack is shown for the rotor and flapping cases in red and green, respectively (right). 66

4.3 A section of a rotating profile experiencing a spanwise variation in angle-of-attack in the presence of radial flow, resulting in vorticity convection ($u_r \partial \omega_r / \partial r$) towards the profile tip. 70

4.4 In order to test the hypothesis for conditions relevant to large wind turbines, change of angle of attack $\Delta\alpha$ and angle of attack gradient $\frac{\partial}{\partial r}\Delta\alpha$ were chosen based on an axial gust impinging on the NREL 5MW turbine. Specifically, the parametric values selected were equivalent to those at the $r/R = 0.3$ spanwise position, where large gradients are observed. The spanwise variation in $\Delta\alpha$ and angle of attack gradient $\frac{\partial}{\partial r}\Delta\alpha$ are shown on the left for a gust of $\Delta U = U_\infty$, and is shown on the right resolved in time. 71

4.5 The pitching program for the two-dimensional reference case follows the angle-of-attack program exactly, and has a flapping angle of exactly zero. Meanwhile, the turbine and flapping cases each have an equal and opposite flapping angle in order to produce the appropriate spanwise gradients. In turn, their pitching programs are adjusted in order to maintain angle-of-attack programs identical to the reference case. . . 72

4.6 All test cases were conducted in a 15m-long towing tank with a 1m × 1m cross section with a semi-enclosed ceiling to minimize free-surface effects. The model (II) was actuated using a robotic pitching-flapping mechanism (I), which was towed from right to left along the upper traverse. A four-camera setup (III) was used to capture the motion of the seeding particles. 73

4.7 The profile is mounted to a mechanism capable of actuating the profile in both flapping and pitching (left). The blade motion intersects two adjacent measurement fields of view taken over separate runs, located at the half-span position. An exemplary volumetric vector field is shown, with the profile indicated for scale (right). 74

4.8 Regions of high rotation are visualized here for the turbine case (left) and the flapping case (right), with the γ_2-criterion for $t^* = 0.8$. This time step is near the end of the measurement period representing the highest observed angle of attack $\alpha \approx 18°$, and thus the largest extent of vortex growth in either test case. The vortex core, defined as $|\gamma_2| > 2/\pi$, is clear for the turbine case, whereas the flapping case exhibits an extended shear layer with no clear roll-up. 76

4.9 Both the spatially-averaged spanwise flow and vorticity gradient within the dynamic stall vortex was found to be similar between the turbine and flapping cases. Please note that the magnitude of the vorticity gradient is plotted here for comparison purposes, and that the vorticity gradient is negative in the turbine case. In both rotational cases the spanwise flow and vorticity gradient both increase as a function of convective time. For spanwise flow this was on the order of the rotational velocity (Ωr), in close agreement with literature (Maxworthy 2007). The reference case exhibited negligible spanwise flow and vorticity gradient. The run-to-run variation was estimated by the standard deviation of the 10 runs, and is plotted every 20 frames. 78

4.10 The growth rate of circulation in the turbine case was found to be greater than that of the reference case. In contrast, the growth rate of circulation in the flapping case was lower than that of the reference case. The difference in circulation growth is a result of the relative alignment of spanwise flow and the spanwise-vorticity gradient between the cases. The error bars denote the standard deviation of the 10 runs plotted every 20 frames. 79

5.1 (a) A vortex-pair forming on a flat plate is illustrated in the familiar Eulerian frame. (b) The same vortex-pair can be studied in a Lagrangian frame: at $t = t_1$ two control masses gain vorticity through the leading and trailing-edge shear layers, respectively, and are tracked forward in time into the vortex core at $t = t_2$. In this way the Lagrangian data can be used to determine the origin of vorticity-containing mass (by tracking structures backwards in time), or to study the evolution of mass gaining vorticity through time (by tracking mass through a shear layer). 86

5.2 A schematic of one of N pathlines acquired within a PTV data set. The number of timesteps within each pathline are contained within the $1 \times N$ vector array $\vec{L}$, while the pathlines themselves are enumerated by counter p. As such, the number of timesteps in which the current pathline is observed is given by $\vec{L}(p)$. The timesteps along pathline p are enumerated by the counter i, and at each timestep the three-dimensional position $\vec{X}(p,i)$, velocity $\vec{U}(p,i)$ and acceleration $\vec{a}(p,i)$ have been measured. With this data set, the velocity-gradient tensor $\nabla\vec{U}(p,i)$ is to be calculated. 89

5.3 Iso-surfaces of $u-$component of velocity with levels 0.25 (yellow) and -0.25 (blue) at $Re_c = 100$. Left: initial flow field at $t = 0$. Middle: current simulation at $t = 5.0$. Right: Brachet et al. (1983) at $t = 5.0$. 94

5.4 Dissipation rate for Taylor-Green vortex at $Re_c = 100$. Current study (solid); Brachet et al. (1983) (dashed). 94

5.5 Particles were advected through the dissipating Taylor-Green vortex field with some artificial noise, and the resulting tracks were processed as if they were PTV data. The resulting RMS error in velocity-gradient components is shown for $t = 5$. The upper row shows a high particle-density case before (left) and after (right) the vorticity correction scheme was applied. The scatter plots on the second row shows a intermediate particle-density case. In both cases, the vorticity correction scheme shows a dramatic reduction in RMS error. For each seeding density, the side-by-side comparison before and after correction can be viewed as a time sequence in the supplementary videos "*Supplementary_Video_5-1.mp4*" and "*Supplementary_Video_5-2.mp4*" 96

5.6 Vorticity magnitude is shown here for the plane $z = \pi/2$ for the high particle-density case. While the recovery if the vorticity pattern is not perfect, the alternating circular pattern is much more evident after the correction scheme is applied. 97

5.7 The per-particle RMS error averaged across the whole computational domain for four different seeding densities. The vorticity-correction method reduced error across all seeding densities (left). The highest and second-lowest seeding densities in this Figure are those shown in Figure 5.5 as high-density and intermediate-density, respectively. The reduction in the objective function is also shown here, as a function of iteration (right). 98

5.8 Schematic of the experimental apparatus: (a) A $D = 30$cm circular plate was accelerated at at a non-dimensional rate of $a^* = aD^3/\nu^2 = 1.1 \times 10^{10}$ through a 15m-long, 1m $\times$ 1m square cross-section optical towing tank; (b) Particles were illuminated with a 40mJ per-pulse laser and captured using four Photron SA-4 cameras. 99

5.9 An instantaneous snapshot of the vorticity field captured from a single image sequence is shown here (a) before and (b) after vorticity-correction on flow-compiled PTV data. The correction scheme allows for the identification of individual instabilities in the shear layer, and the clear identification of the vortex core. This side-by-side comparison is available as a time sequence in the supplementary video "*Supplementary_Video_5-3.mp4*" 101

5.10 The magnitude of the objective function along an individual pathline is shown here as a function of iteration to visualize both the noise reduction observed and the computational speed. The 40% reduction in the objective is similar to the 40% reduction in error observed in synthetic data. 102

5.11 Utilizing the pathline information can elucidate material transport within a flow. For instance, on the left (a) particles are tracked forward in time from the shear layer to a later time-step, shown here overlayed on the vorticity field at that later time-step. This shows the advection of material from a vorticity source. Alternatively, particles can be tracked from the vortex core backwards in time, shown in the right (b), to identify the origin of that vorticity-containing mass. 103

6.1 The LEV formed on the suction side of a delta wing is fed by a leading-edge shear layer. In order fo this LEV to remain stationary, the vorticity-containing mass fed into the LEV must be balanced by spanwise transport of vorticity-containing mass or vorticity annihilation. ξ is the coordinate along the shear layer. 107

6.2 The vorticity entering the leading-edge vortex can be determined by integrating around a shear layer of length l and thickness d. Although these values are important for intermediate steps, all geometric constraints ultimately cancel out in the derivation. ξ is the coordinate along the shear layer. 111

6.3 In the proposed model, particles representing vorticity-containing mass are initialized randomly along the span of the profile at every timestep. As the local circulation generated at any timestep is $\Delta t u_{\text{eff}}^2$, this circulation is divided equally among all the particles within a spanwise bin. 112

6.4 At each timestep, particles from previous timesteps are advected along the span of the profile by the spanwise flow w. Each spanwise location has a total circulation Γ determined by all the particles in that bin, both from the current timestep and all prior timesteps. 114

6.5 The time- and spanwise-resolved solution to the vortex growth on a delta wing converges upon a conical circulation distribution. This conical circulation distribution satisfies the vorticity transport equation when diffusion and vortex tilting are neglected. 114

6.6 A rack-and-pinion traverse is used to tow a flat-plate delta wing at a Reynolds number of Re =250,000. The wing was mounted to a sting by its pressure-side, which extended up 0.5 m to the high-speed traverse. 116

6.7 The shear layer on a flat-plate delta wing is captured using time-resolved PIV. 100μm hollow glass microspheres were illuminated with a 40mJ per-pulse high-speed laser and captured using a Photron SA-Z camera at 10,000 Hz. The field of view on the suction side (bottom) is approximately 30×30 mm^2. 117

6.8 Volumetric, time-resolved 4D-PTV measurements were used to characterize the velocity gradient tensor, in order to validate the Monte Carlo simulation described in Section 6.3. 100μm hollow glass microspheres were illuminated with a 40mJ per-pulse high-speed laser and captured using four Photron SA-4 cameras at 1,500 Hz. The field of view as approximately 120×120×10 mm^3, located on the suction side (bottom) of the model. 118

6.9 The shear-layer feeding rate can be characterized in one of two ways: (a) the rate of circulation feeding is proportional to the square of the effective velocity u_{eff}^2 following Equation (6.4), or; (b) the rate of circulation feeding is the integral of the product of chordwise-velocity and vorticity following Equation (6.11). While the first method avoids any empirical dependence on the shear-layer thickness, its accuracy must be validated. 120

6.10 The velocity profiles sampled in Figure 6.9 are shown here as a function of the shear-layer coordinate ξ. The velocity profile u_{eff} and the vorticity flux $u_x\omega_z$ produce nearly identical circulation feeding rates. . 121

6.11 The three-dimensional vorticity field is shown here projected onto a single plane. Vorticity values below and upstream of the wing have been masked. The domain used to integrate circulation values and compute spanwise flow and circulation gradient values tabulated in Table 6.1 is shown as the dashed box. 122

7.1 A delta wing exhibits a stationary LEV, similar to the flapping propulsors of natural swimmers and flyers. This LEV must also satisfy the conservation of mass and circulation, and therefore can be modelled using similar techniques to those developed for biomimetic propulsion. 132

A.1 The tip amplification can be parameterized in terms of dimensionless stiffness and density ratio, as shown on the left. Choosing stiffness and density ratios within the range of swimmers, birds, and insects, this tip amplification can be visualized by the tip path, shown on the right. 155

A.2 Given the same stiffness landscape as in Figure A.1, small changes in the selection of stiffness and density can be chosen in order to collapse the resulting tip paths. Thus, regardless of the environment, it would be possible for animals to converge upon the same optimum gradient in effective incidence. 155

List of Abbreviations, Acronyms and Symbols

Acronyms

AUV	Autonomous underwater vehicle,
LEV	Leading-edge vortex,
MAV	Micro-aerial vehicle,
NACA	National Advisory Committee for Aeronautics (airfoil series),
Nd:YLF	Neodymium-doped yttrium lithium fluoride (lasing medium),
PIV	Particle image velocimetry,
· Stereo-PIV	Stereoscopic particle image velocimetry,
· Tomo-PIV	Tomographic particle image velocimetry,
PTV	Particle tracking velocimetry,
· 3D-PTV	Three-dimensional particle tracking velocimetry,
· 4D-PTV	Four-dimensional particle tracking velocimetry (syn. for *STB*),
RMS	Root-mean-square,
STB	Shake-the-Box,
UAV	Unmanned aerial vehicle,
VIC+	Vortex-in-Cell

Symbols

Latin

a	Acceleration,
· a^*	Dimensionless acceleration (linear),
· a_{ang}	Angular acceleration ,
· a_{cen}	Centripetal acceleration,
· a_{Cor}	Coriolis acceleration,
A	Area (of a vortex),
AR	Aspect ratio,
c	Chord,
C_F	Force coefficient,
d	Shear-layer thickness,
D	Diameter,
EI	Stiffness,
f	Frequency,
F	Force,
g	Acceleration due to gravity,
h_0	Heaving amplitude,
H_n	Helicity,
k	Reduced frequency,
l	Length,
L	Length scale,
m'	Mass per unit span,
O	Objective function,

p	Pathline,
· $\vec{X}(p,i)$	Position along pathline p,
· $\vec{U}(p,i)$	Velocity along pathline p,
· $\vec{a}(p,i)$	Acceleration along pathline p,
· $\vec{L}(p)$	Length of pathline p,
px	Pixel,
R	Profile span,
$R(p,i)$	Residual (of vorticity equation),
Re	Reynolds Number,
Ro	Rossby Number,
St	Strouhal Number,
· St^*	Strouhal Number (modified for rotation),
t	Time,
· t^*	Dimensionless time,
· t_r	Ramp time,
· t_c	Time at constant velocity,
T	Period of motion,
$\hat{T}$	Formation time,
u, v, w	Velocity components,
· u_{eff}, U_{eff}	Effective velocity,
· U_∞	Free-stream velocity,
· ΔU	Change in velocity (gust),
x, y, z	Cartesian coordinates,
· r, θ, z	Polar coordinates

Greek

α	angle-of-attack (or step size in Chapter 5 only),
· α_0	initial angle-of-attack,
· α_{eff}	effective angle-of-attack,
· α_{geo}	geometric angle-of-attack,
· $\Delta\alpha$	change in angle-of-attack (gust),
γ_1, γ_2	vortex centre and vortex core identification criterions,
· M	test point in region S,
· N	number of points in region S,
· P	point at which γ_1 or γ_2 is being computed
· S	region about point P,
· θ_m	angle between the velocity at M and the vector from P to M,
Γ	Circulation,
δ	Thickness, shear layer thickness,
ϵ	Dissipation rate,
Λ	Sweep angle,
ν	Kinematic viscosity,
ξ	Shear layer coordinate,
Π_1	Dimensionless stiffness,
ρ	Density,
· ρ^*	Density ratio,
$\phi_{\max}$	Maximum rotational displacement,
ω_x, ω_y, ω_z	Vorticity coordinates in x, y and z,
Ω	Angular velocity (flapping)

Chapter 1

Introduction

Flying and swimming animals have inspired engineers for as long as there have been engineers, even well before the earliest gliding experiments of Lilienthal (1889). Modern engineered vehicles far outperform biological locomotion at the upper bounds of velocity and altitude. However, natural flyers and swimmers still maintain significant performance advantages at low-speeds and at small scales. For instance, Shelton et al. (2014) observed cliff swallows in tandem flight performing manoeuvres of up to $7.8g$. Those fixed-wing aircraft that are capable of matching the high-speed accelerations of these small birds are not capable of similar low-speed manoeuvring, as demonstrated by recent attempts to emulate bird-like control in perching by Moore et al. (2014). In fact, Carruthers et al. (2007) have shown that birds of prey such as *Aquila nipalensis* utilize sophisticated control devices, both passive separation of specialized feathers, and active manipulation of the alula (a small stub-wing that can be manipulated like a thumb), specifically for such low-speed perching. Meanwhile, rotary-wing aircraft that are capable of bird-like, low-speed performance, like the perching demonstrated by Doyle et al. (2012), have thrust-to-weight ratios rarely exceeding three (see Stingu and Lewis (2009)). Therefore, such rotary-wing unmanned aerial vehicles (UAVs)

cannot match the high-speed accelerations of the cliff swallow. Natural flyers achieve the above performance efficiently and silently, and there are ongoing efforts to not only understand the performance of biological propulsion, but to adopt biomimetic noise-reduction and flow-control techniques into UAV design as well, as described by Anders (2000).

This chapter will summarize the performance of natural flyers and swimmers, in relation to both their closest engineering equivalents and in the context of their natural environment. Particular attention will be given to instances of evolutionary convergence, as these scenarios are most likely to provide examples of robust aerodynamic and hydrodynamic optimizations that may be borrowed by engineers. Subsequently, the current limitations of engineered vehicles will be outlined and the contributions of the current thesis will be set out in relation to these ongoing challenges.

1.1 The aerodynamic and hydrodynamic performance of natural flyers and swimmers

Aerodynamic and hydrodynamic constraints dominate the body layout of flyers and swimmers. For instance, Hartloper and Rival (2013) were inspired by the fact that swimming animals had converged upon a lunate shape for four species of completely separate evolutionary lineage. Maurer et al. (2004) further showed that the body-mass of small vertebrates were split along the lines of flying versus non-flying species, rather than the evolutionary origin of a particular organism. Whereas the body mass of terrestrial animals scales with both their length scale and ecological niche, Tennekes (2009) noted that winged flyers (biological or otherwise) scale with their length scale L^3, as shown in his *Great Flight Diagram* in Figure 1.1. The above

examples demonstrate extreme environmental pressures. The evolutionary response to this pressure is detailed in the following section.

1.1.1 Evolutionary convergence in flexibility, profile shape and stroke amplitude

Due to their reliance on buoyancy, swimmers do not exhibit the same convergence with respect to body mass that has been observed in flyers. However, Lucas et al. (2014) has observed similar levels of propulsor flexibility under cruising conditions, across insects, avians, fish, and both swimming and flying mammals in Reynolds numbers ranging from $10^2 \leq Re \leq 10^8$. It is not surprising that the propulsive efficiency of a flexible propulsor dictates an optimal bending, as this has previously been identified by Heathcote et al. (2007). However, it is remarkable that this optimum does not appear to change over such a broad range of Reynolds numbers, dimensionless stiffnesses, or mass ratios. Definitions for dimensionless stiffness and mass ratio can be found in Appendix A. The observation included both small aquatic swimmers, for whom propulsion is dominated by added mass, as shown by Eloy (2013), as well as high Reynolds number flyers, for whom propulsion is dominated by circulatory effects, as shown by Sane and Dickinson (2002).

Heathcote et al. (2007) found that for the cases they investigated, efficiency only improved for spanwise flexible profiles over a narrow range of plunging kinematics, specifically defined by the Strouhal number:

$$St = \frac{f(2h_0)}{U_\infty} \ , \tag{1.1}$$

where f is the frequency of motion, $2h_0$ is the plunging amplitude or wake width,

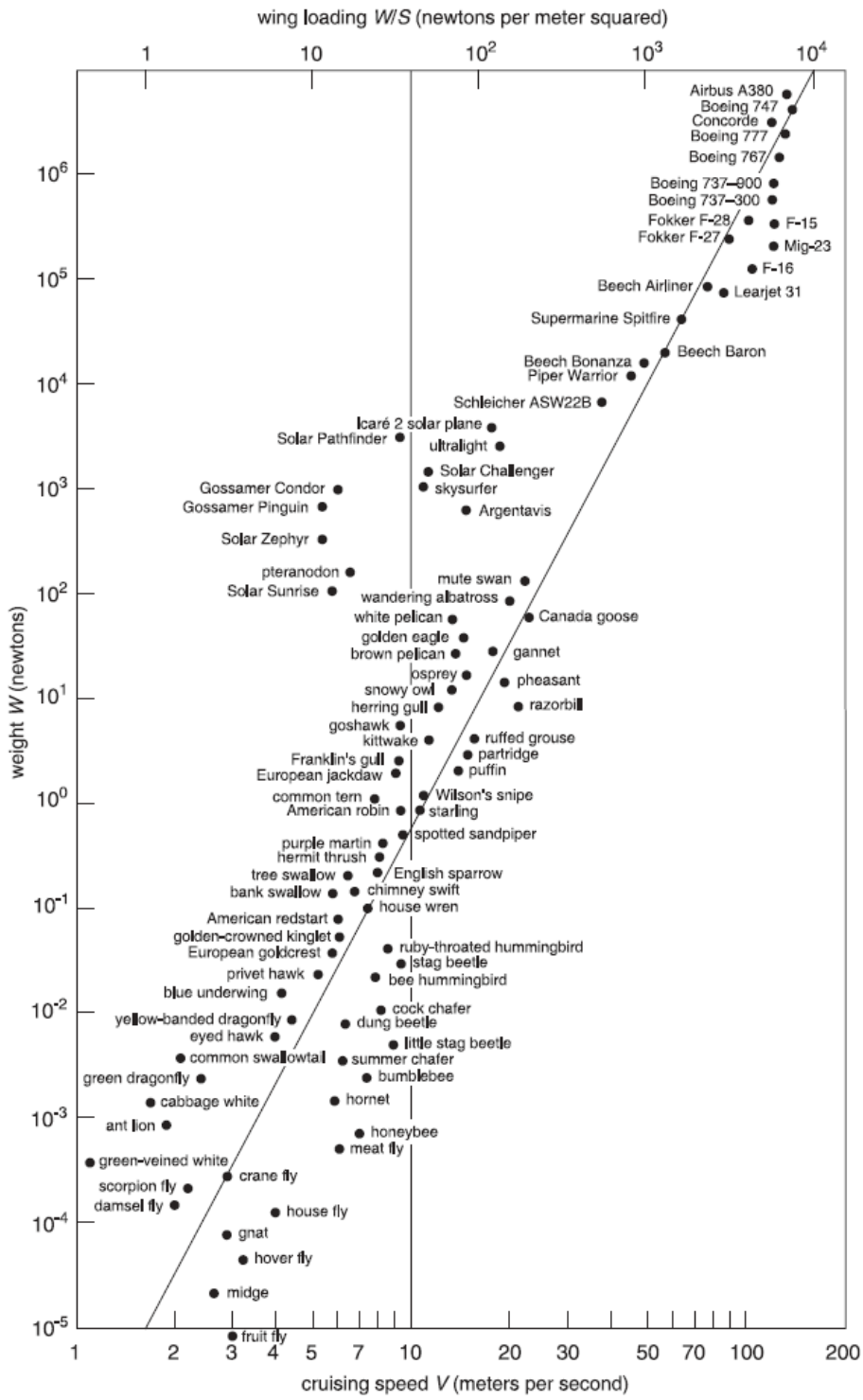

Figure 1.1: The *Great Flight Diagram* demonstrates scaling of flying machines, engineered and natural, follow L^3 over twelve orders of magnitude. Taken from Tennekes (2009).

and U_∞ is the free-stream velocity. Heathcote and co-authors found that flexibility only improved propulsive efficiencies within the range $0.2 \leq St \leq 0.4$. This range of Strouhal numbers happens to coincide with the cruise conditions of nearly all flapping flyers and swimmers, identified by Taylor et al. (2003) to be approximately $St \approx 0.3$. The exact same range $0.2 \leq St \leq 0.4$ had previously been identified by Triantafyllou et al. (1991) to provide optimal propulsive efficiency on rigid, two-dimensional wings. This behavioural convergence is so distinct that Nudds et al. (2004) utilized the near-constant Strouhal number as a predictive tool for determining scaling laws in avian flight. As the loading on a two-dimensional pitching and heaving profile is governed primarily by the Strouhal number, as shown by Baik et al. (2012), obtaining the same spanwise bending at the same Strouhal numbers across such a broad range of length scales would require significant tuning of dimensionless stiffness. The stiffness of select insect wings are compiled in Table A.1 of Appendix A.

Dabiri (2009) identified this critical Strouhal number to be equivalent to the so-called *optimal vortex formation*:

$$\hat{T} = \frac{1}{St} \approx 4 \ , \tag{1.2}$$

where the formation number $\hat{T}$ is the timescale of circulation production for a particular vortex. *Optimal vortex formation*, the particular formation number of $\hat{T} \approx 4$, was previously identified by Gharib et al. (1998) as the point at which a vortex generated by a piston-cylinder no longer accepted additional circulation from the shear-layer, known as pinch-off. Even though the above formation number was determined for piston-cylinders, the same formation number $\hat{T} \approx 4$ has been found by Milano and Gharib (2005) to maximize the lift coefficient of a flapping flat plate with kinematics

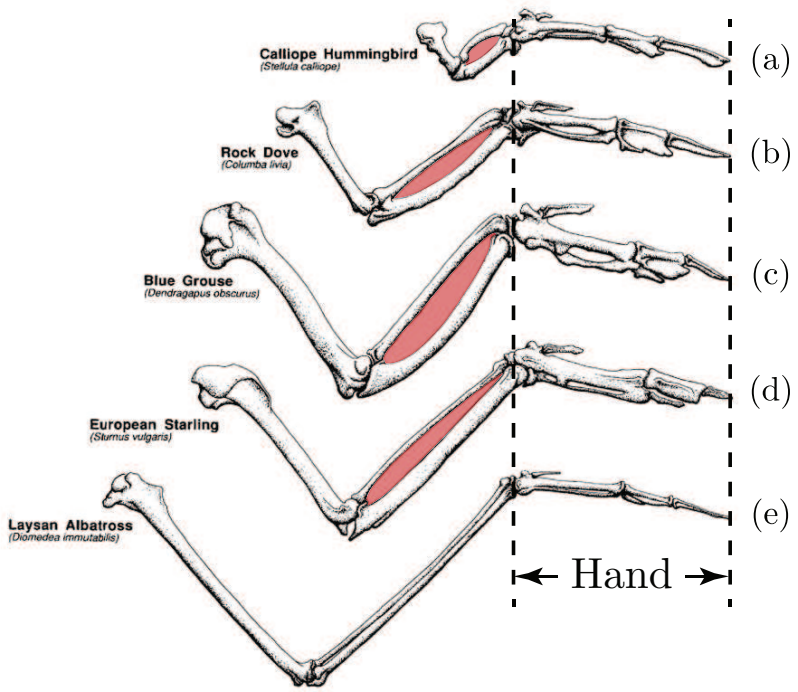

Figure 1.2: Relative forearm length of five bird species: (a) Calliope hummingbird; (b) Rock dove; (c) Blue grouse; (d) European starling; (e) Laysan albatross. Taken from Dial (1992).

similar to a hovering insect.

The collapse upon specific profile kinematics across many diverse species, environments and length-scales suggests that biological locomotion is highly optimized specifically for aerodynamic and hydrodynamic performance. However, much of the evolutionary convergence listed above is only observed in cruising conditions. For instance, Dabiri (2009) noted that during escape manoeuvres, jellyfish swam with formation numbers of up to $\hat{T} \approx 8$. Therefore, it is worth also considering how the strategies used in nature differ between cruising and manoeuvring.

1.1.2 Variations in flow topology between manoeuvring and cruising

The convergence upon similar wing kinematics and flexibility is remarkable given the range of environments encountered in nature. For instance, consider the diagram of forelimb skeletons for five avian species taken from Dial (1992) shown in Figure 1.2, normalized by the hand length. The wing hand is critical for flight control during take-off, landing, and manoeuvring. As Videler (2005) notes, the space between the ulna and radius is occupied by the muscles that control the hand, and thus indicates the relative importance of manoeuvring. For the Calliope hummingbird, the hand is 60% of the total wingspan, whereas it is just 20% for the Laysan albatross. Clearly, body layout of the hummingbird is not meant for cruising flight.

Unlike in cruising flight, drag may be desirable, such as during perching (see Carruthers et al. (2007)). Alternatively, drag may be acceptable when very large force coefficients are required. For instance, insects may intentionally enter a stalled state by forming a leading-edge vortex (LEV) in order to achieve the forces required to hover, as described by Sane (2003). Pitt Ford and Babinsky (2013) showed that this LEV is the dominant contributor to circulation for stalled wings at low Reynolds numbers. This vortex dramatically reduces surface pressure on the suction-side of a profile, increasing lift. Significant attention has been given to the condition of *LEV stability*, where the LEV remains attached indefinitely to the profile of the wing, maintaining the lift enhancement of the LEV. As this LEV is being continually fed both circulation and mass, Ellington et al. (1996) suggested that spanwise flow is responsible for LEV stability following the same mechanism as delta wings. Lentink and Dickinson (2009b) determined that this spanwise flow was driven by large rotational accelerations, which are related to Coriolis forcing and scaled by the Rossby

number. In the specific case of rotating wings, the Rossby number reduces to the wing aspect ratio:

$$Ro = R/c \ , \tag{1.3}$$

where R is the profile span and c is the profile chord. The Rossby number gives the relative strength of inertial to Coriolis forces, with lower Rossby numbers representing greater rotational accelerations, and Rossby numbers on the order of one providing stable vortices.

Many authors have found stable LEVs at low Rossby numbers, such as Birch et al. (2004), Poelma et al. (2006), and even on samara seeds in the case of Lee et al. (2014). However, it does not appear the spanwise flow generated by rotation is alone responsible for LEV stabilization. For instance, both Beem et al. (2012) and Wong et al. (2013a) failed to observe any LEV stability on nominally two-dimensional plunging profiles with sweep angles as high as 45°. Moreover, in a waving-wing experiment with large rotational accelerations, Jones and Babinsky (2011) did not observe LEV stability within the range $10,000 \leq Re \leq 60,000$. Harbig et al. (2013) observed stable LEVs at Rossby numbers as high as $Ro = 7$. Rather, Rival et al. (2014) gave a topological constraint on LEV stability, whereby the physical size of the LEV had to be maintained below the chord length c. As the LEV approached this limiting length-scale, the streamline bounding the LEV could no longer be maintained on the profile surface, and instead formed a saddle-point in the flow, beginning the LEV detachment process. The possible mechanisms of maintaining this steady vortex size and strength is described in the following section.

1.1.3 The role of the circulation budget in determining wing kinematics and shape

A stable LEV is fed both mass and circulation continuously from a leading-edge shear layer, as shown in Figure 1.3, despite maintaining a constant size and strength. Therefore, as a minimum condition of LEV stability there must be a balance of circulation and mass entering and leaving the LEV, as illustrated in Figure 1.4, similar to the case of delta wings (see Ol and Gharib (2003)). However, axial flow along the vortex alone cannot balance either the mass or the circulation entering through the shear layer. Consider the $z-$component of the vorticity transport equation:

$$\frac{\partial \omega_z}{\partial t} + u\frac{\partial \omega_z}{\partial x} + v\frac{\partial \omega_z}{\partial y} + w\frac{\partial \omega_z}{\partial z} = \omega_x\frac{\partial w}{\partial x} + \omega_y\frac{\partial w}{\partial y} + \omega_z\frac{\partial w}{\partial z} \ , \tag{1.4}$$

where terms from left-to-right represent the rate of change of vorticity due to unsteadiness, advection of vorticity in the streamwise (x), chord-normal (y), and spanwise (z) directions, vortex tilting in the streamwise and chord-normal directions, and vortex stretching, respectively. The diffusion of vorticity is omitted from the above equation for clarity. The spanwise convection of vorticity $w\ {}^{\partial \omega_z}/_{\partial z}$ requires not just a spanwise flow, but also a gradient of vorticity. Without any mechanism to initiate the spanwise gradient of vorticity, in hindsight it is no surprise that Beem et al. (2012) and Wong et al. (2013a) were unable to generate stable LEVs on nominally two-dimensional plunging profiles.

While rotation can set up a spanwise gradient of vorticity, rotation is not necessary. For instance, Jain et al. (2015) demonstrated that spanwise flexible profiles dynamically redistributed circulation along their length. Alternatively, by careful selection

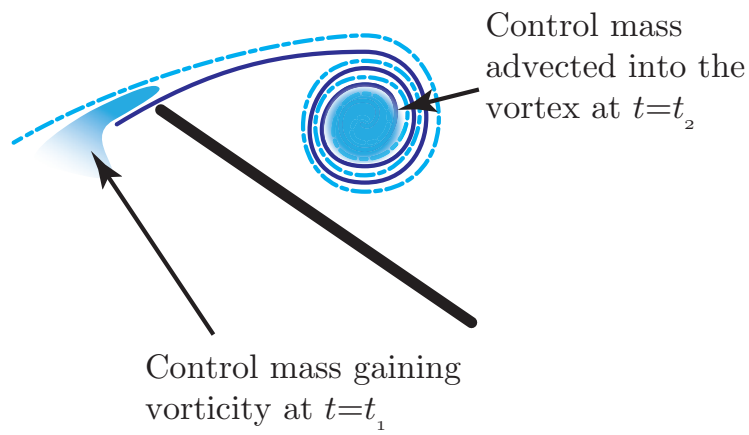

Figure 1.3: The LEV, shown here as the spiralling blue pattern of streamlines, is continuously fed vorticity-containing mass from the leading-edge shear layer. Despite this injection of both circulation and mass, many LEVs remain at a constant strength and size on rotating wings.

of the profile shape, Hartloper and Rival (2013) were able to convect circulation outboard and suppress the LEV from lifting off the profile surface. Vorticity convection is not alone in balancing the vorticity entering an LEV. For instance, Wojcik and Buchholz (2014) demonstrated that vorticity annihilation on an airfoil surface can be the dominant circulation-balancing mechanism, especially at low Reynolds numbers. Critically, these recent studies have shown that it is the circulation budget, and not inherently rotation, that dictates LEV stability. Rather, rotation produces the appropriate conditions for vorticity convection, annihilation, and stretching.

1.2 Engineering applications of the flow physics of natural swimming and flight

While biological locomotion is interesting in its own, the goal of this thesis is to advance the state of engineering as well. Therefore, we must consider how the physics of

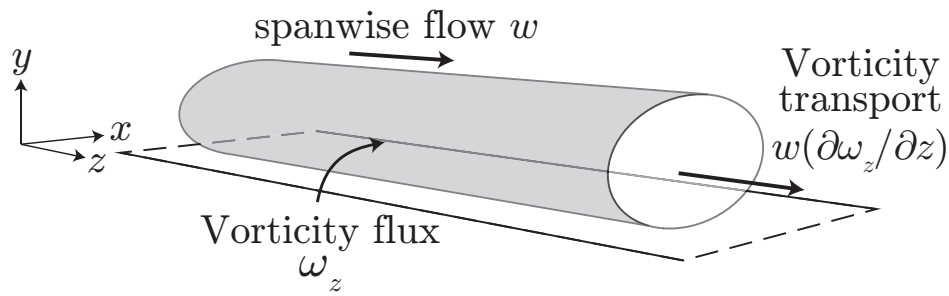

Figure 1.4: Mass is fed into an LEV through the leading-edge shear layer, carrying with it vorticity ω_z. In order for the LEV to be stationary, both the vorticity and mass entering the LEV must be balanced either by vorticity annihilation or spanwise circulation transport. The spanwise flow w shown here facilitates that balance by convecting vorticity along the span.

natural swimming and flying will influence design and engineering practice. Perhaps the most straightforward application of understanding small swimmers and flyers is in the *design* of small swimmers and flyers. Torres and Mueller (2004) define the micro-aerial vehicle (MAV) as a flying machine with a wingspan on the order of $15cm$, operating in the Reynolds number range $10^3 \leq Re \leq 10^5$, which is well within the range of avian flight. Autonomous underwater vehicles (AUVs) operate at a similar Reynolds number range of $10^3 \leq Re \leq 10^6$, overlapping that of fish (see MacIver et al. (2004)). These are far from the only applications of this physics, as similar flow structures such as LEVs form on delta wings, rotorcraft, and high-performance aircraft. Chapter 4 will focus on comparing the LEV formed on a flapping wing to that on a wind turbine encountering a gust, for example. However, given the clear relationship between these engineered vehicles and machines, and natural swimming and flying, it is worth considering a direct comparison of their respective performance.

1.2.1 The performance of engineered vehicles at comparable Reynolds numbers

Some flight characteristics of current engineered vehicles compare favourably to biological propulsion. For instance, free-flight measurements of the *DelFly II* MAV by Karàsek et al. (2016) gave a maximum acceleration of approximately $2g$. Meanwhile, large birds such as cockatoos rarely exceed accelerations of $1.5g$ in free flight (see Bowlin and Winkler (2004)), although hummingbirds are capable of $4g$ (see Tobalske et al. (2004)). While these are far from the maximum accelerations observed in birds, such as dive recoveries of nearly $10g$ observed by Clark (2009), this does demonstrate that engineered vehicles at least approach the wing actuation of natural flyers. As propulsive efficiency is dominated by kinematic parameters like the Strouhal number, it is also possible to match the propulsive efficiency of natural swimmers and flyers in cruise. Although this thesis will generally neglect non-aerodynamic considerations such as battery and motor performance, Hawkes and Lentink (2016) showed that biomimetic oscillatory machines were much more efficient than rotating machinery at insect length-scales.

More impressive is the performance of AUVs. An octopus-like, jet-based robot reported by Weymouth et al. (2015) achieved escape-accelerations as high as those found in cephalopods, and at efficiencies as high or even higher. Conte et al. (2010) also developed a robotic fish capable of fast-starts comparable to river pike. In both of these examples, matching the natural flexibility and deformation of swimmers was critical to achieving similar performance. Indeed, in their study of a robotic shark-tail, Flammang et al. (2011) noted that their model would have to mimic the active deformation of a real shark fin in order to achieve the same performance.

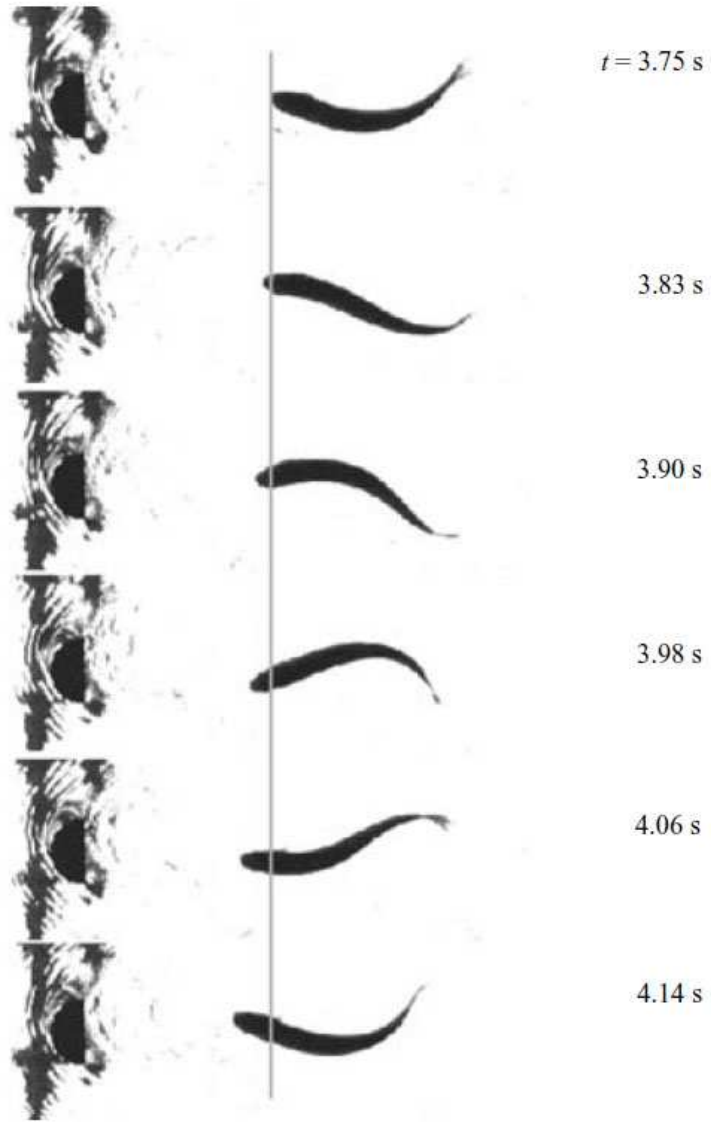

Figure 1.5: A vortex street is shed from a D-cylinder upstream of an euthanized trout. The body flexibility of this trout is able to extract sufficient energy from this oscillating flow field to swim upstream against drag. Taken from Beal et al. (2006).

One area where biological locomotion is well ahead of engineered vehicles is stability in gusty environments. With respect to flight, Fisher et al. (2016) noted that flapping wings themselves provide some inherent gust mitigation. Despite this, few flapping wing MAVs are able to operate outdoors due to the natural turbulence found in the atmospheric boundary layer. Riverine fish take this a step further, and instead of merely mitigating the turbulence in their environment, are able to extract energy from the turbulent wakes in the flow around them, as shown by Liao et al. (2003). The tuning of body flexibility in riverine fish is so profound that Beal et al. (2006) discovered that even a dead fish is capable of swimming upstream, as shown in Figure 1.5, as its body can efficiently and passively collect energy from its environment.

1.2.2 Limitations of current engineering applications

The previous section highlighted some ways natural swimmers and flyers exploit vortex flows, often with much greater effectiveness than engineered vehicles. However, translating this observed behaviour into engineering applications is by no means straightforward. This section will outline the primary challenges in adopting biomimetic strategies in MAV and UAV design, as well as in other machines.

Understanding swimming and flying strategies

The cases of evolutionary convergence discussed in Section 1.1.1 notwithstanding, the immense parameter variation observed in nature obfuscates the relationship between propulsion kinematics and the resulting flow. For instance, while Beal et al. (2006) were able to show that euthanized fish could extract energy from a flow, the study

only attempted to replicate this behaviour on a two-dimensional pitching and heaving foil. This pitching/heaving motion has just two degrees of freedom: pitch and heave. Replicating this energy extraction for a three-dimensional fish-like swimmer involves orders of magnitude more degrees of freedom, and thus requires a much more sophisticated understanding of the flow physics.

Similarly, while Fisher et al. (2016) were able to identify flapping wings as an inherently stabilizing mode of flight, they were unable to match the stability of real insects or birds. Insects in particular are *sensor rich*: Mohamed et al. (2014) identified visual and inertial sensing, wind-sensitive hairs, and wing-load sensors in the wing root as just some of the information available. Mohamed et al. (2014) further suggest that insects utilize all this information together in sensor-fusion to inform wing kinematics. In both of the above examples, the major engineering hurdle is the cost of studying a broad parameter space, in both resources and time, either computationally or experimentally, which is closely related to the next section on *low-cost modelling*.

Challenges in vortex modelling

If an engineer wished to explore the parameter space of energy extraction in fish or gust mitigation in insects, neither could be accomplished affordably with experiment nor numerical simulation. For instance, with enormous experimental cost, Kang et al. (2011) identified ten non-dimensional parameters governing the fluid-structure interaction of flapping wings, and this without any attempt to account for gusts. Therefore, reliable low-cost models are required to explore this immense parameter space both as an engineering tool, and to guide subsequent investigations into flow

physics.

Potential flow models, such as that of Hemati et al. (2014), are very attractive due to their rapid computational time, and extremely accurate force histories in two-dimensional flows. However, understanding the full three-dimensional flow is critical in predicting LEV stability, for instance, as described in Section 1.1.3. Therefore, advancing the current state of low-cost models will require the inclusion of three-dimensional effects in an computationally-efficient way, solving a minimum number of equations. Developing such models is limited in part by difficulty in determining transport phenomena within an LEV, requiring advancements in the measurement science itself.

Volumetric measurements of vortex topology and vorticity transport

The determination of vorticity transport in three-dimensional flows requires resolving every component of the velocity-gradient tensor. This can be accomplished through a variety of methods, such as using a minimum of two adjacent measurement planes with stereo particle image velocimetry (Stereo-PIV). For approximately a decade, time-resolved measurements of this type have been made possible through tomographic-PIV (see Elsinga et al. (2006)).

Such methods are perfectly adequate for determining vorticity transport. However, Lagrangian analysis is much more effective at capturing flow topology, for instance with Lagrangian coherent structures as demonstrated in Rockwood et al. (2016). Lagrangian measurement techniques, such as *'Shake-the-Box'* (STB) particle tracking velocimetry (PTV), as described by Schanz et al. (2016), are adept at capturing the Lagrangian flow-field, but most analysis tools still convert this data

back to the familiar Eulerian grid. Therefore, measurement techniques that retain this Lagrangian information must be developed in order to facilitate the simultaneous study of both vorticity transport and flow topology.

1.3 Contributions of the Current Thesis

The engineering challenges listed in Section 1.2.2 cannot be approached independently. Advancing knowledge in flow physics and flying of swimming strategies requires advances in measurement techniques and modelling in parallel. Meanwhile, advancing low-cost models requires a sophisticated understanding of the flow physics and advanced measurements for validation purposes. In turn, the current thesis makes contributions to each of the above areas: determination of flight strategies, modelling of separated flows, and advancing measurement techniques.

These three contributions are detailed in the following five chapters. These five chapters have been published or are under review in peer-reviewed journals, with the exception of Chapter 6, which is being prepared for submission. Therefore, the central chapters of this thesis constitute those manuscripts, appearing exactly as published or submitted. It should be noted that the parenthetical citation style used in Chapter 4 is to maintain similitude with its corresponding published article. Figure 1.6 highlights the relationship between each chapter and the three contribution areas outlined above.

Chapter 2 investigates the relative stability of LEVs on plunging and flapping profiles of varying sweep. A simple scaling rule is derived for the time-scale of LEV detachment on two-dimensional profiles, which is validated with planar PIV. Furthermore, it is hypothesized that spanwise flow along a profile can modulate the spanwise

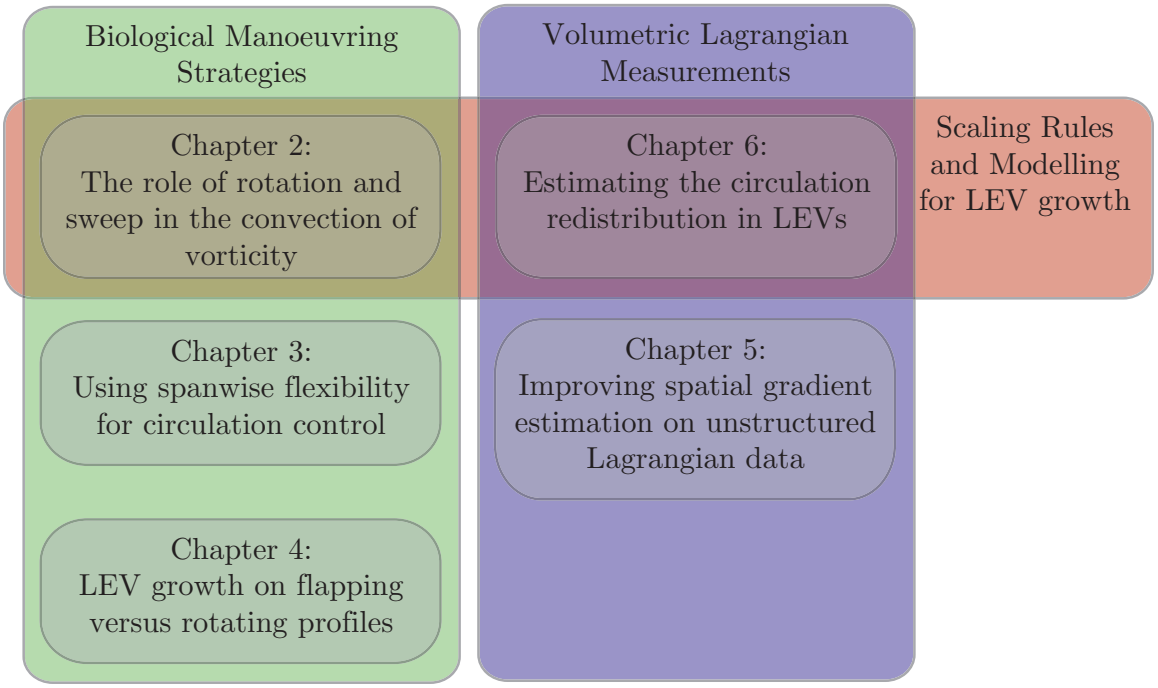

Figure 1.6: Chapters 2, 4 and 3 of this thesis contribute to understanding biological propulsion phenomenologically. This phenomenological understanding is used to develop low-cost models presented in Chapters 2 and 6. The high-resolution measurement techniques used for such studies are advanced in Chapters 5 and 6.

convection of vorticity, but cannot induce vorticity transport on its own, based on a model for the circulation budget of an LEV. The hypotheses and proposed model are confirmed and validated, respectively, utilizing 3D-PTV measurements of the LEV growth. This finding contributes to understanding the ubiquity of swept profiles found throughout flying and swimming animals, and provides two- and three-dimensional models for scaling LEV growth and stability, respectively.

Based on the use of vorticity convection to improve LEV stability, Chapter 3 investigates the use of flexibility in swimmers and flyers as a method of circulation control. By either bending their propulsors into or away from the direction of motion,

it is hypothesized that these animals can modulate their spanwise flow arbitrarily in order to control the strength of the LEV. This, in turn, can be utilized by the animal to either increase lift at the expense of LEV stability (higher lift forces for a shorter period of time), or increase LEV stability at the expense of lift (lower lift forces for a longer period of time). STB PTV is used to show that this spanwise profile bending can indeed modulate LEV circulation, providing new insight into the use of flexibility in swimming and flight.

Together, Chapters 2 and 3 provide the bulk of new insight into animal locomotion. Chapter 4, meanwhile, applies the knowledge from these previous two chapters to compare the separated flow observed on a bird's wing to that of a wind turbine experiencing an axial gust. In both cases the spanwise flow is directed from root to tip. However, the angle-of-attack gradient is reversed in each case. It is found that in the bird-like case the LEV circulation is reduced, while in the turbine-like case spanwise flow promotes LEV growth, increasing peak-to-peak loading and unsteadiness, both major causes of fatigue in wind-turbine gearboxes.

The above three chapters form the bulk of the phenomenological contributions of this thesis. The focus of Chapter 5, in contrast, is specifically on measurement techniques. In particular, a method is proposed to improve the quality of spatial gradients obtained from experimental PTV data that operates directly on unstructured Lagrangian pathlines without ensemble averaging. By doing so, the material transport information inherent to the pathline data is retained. The method operates by penalizing velocity-gradient estimates that do not satisfy the vorticity transport equation. Both measurement error and noise are reduced in both experimental and a synthetic test cases, allowing for the identification of flow structures that are otherwise

obscured by noise.

Finally, Chapter 6 builds on the modelling work of Chapter 2 by producing a predictive model for the spanwise transport of circulation within a vortex. Previously, this spanwise transport was modelled semi-empirically, requiring some measurement data as an input to produce useful results. This model is validated on the attached LEV found above a flat-plate delta wing, utilizing data collected with STB PTV, and corrected using the method from Chapter 5. This work presents the opportunities of low-cost modelling for optimizing leading-edge shape and profile kinematics.

Chapter 2

Determining the Relative Stability of Leading-Edge Vortices on Nominally Two-Dimensional Flapping Profiles

2.1 Abstract

It is hypothesized that the relative stability of leading-edge vortices (LEVs) on flapping profiles can be improved by moderating LEV growth through spanwise vorticity convection and vortex stretching. Moreover, it is hypothesized that the reduced frequency k and profile sweep Λ are critical in predicting relative LEV stability as determined by the aforementioned effects. These hypotheses are then confirmed experimentally with phase-averaged Particle Image Velocimetry and three-dimensional Particle Tracking Velocimetry. In particular, more stable LEVs are observed at higher reduced frequencies, which is argued to represent the ratio between the limiting vortex size and the rate of vorticity feeding. The introduction of profile sweep increased both relative LEV stability and spanwise vorticity transport. It is thought that spanwise vorticity transport improved LEV stability by acting as a sink for vorticity generated

in the leading-edge shear layer.

2.2 Introduction

In natural swimming and flying rapid maneuvering is generally achieved via undulating or flapping fins, flukes or wings, often with a swept leading edge. In particular, the flapping wings of insects are known to exploit leading-edge vortices (LEVs) for lift enhancement, as discussed by Ellington et al. (1996). These LEVs are the dominant contributor to circulation on stalled profiles at low Reynolds numbers, as demonstrated by Pitt Ford and Babinsky (2013), and have been observed on rotating and translating profiles over a broad range of Reynolds numbers ($200 \leq Re \leq 60,000$), such as by Garmann et al. (2013) and Lentink and Dickinson (2009b), Strouhal numbers ($0.1 \leq St \leq 0.6$) and reduced frequencies ($0.2 \leq k \leq 1$), by Rival and Tropea (2010) and Baik et al. (2012), and aspect ratios ($2.9 \leq AR \leq 7.3$), by Harbig et al. (2013). The above parameters vary the lift and drag production of an LEV, as observed by Garmann et al. (2013) with respect to Reynolds number, or alter the propulsive efficiency, as observed by Taylor et al. (2003) with respect to Strouhal number. However, the parameter of rotation is unique in that rotating cases often exhibit vortex stability, where both the convection speed of the LEV relative to the profile and the growth rate of the LEV are near zero, as observed by Ozen and Rockwell (2012), Wojcik and Buchholz (2014), and Cheng et al. (2013), to name a few.

A number of mechanisms for vortex stability have been proposed. Lentink and Dickinson (2009b) suggested that large rotational accelerations associated with low aspect-ratio profiles stabilized LEVs. However, Harbig et al. (2013) identified stable LEVs on profiles in the range of aspect ratios $2.9 \leq AR \leq 7.3$. Over a similar aspect

ratio range of $2 \leq AR \leq 4$, Jones et al. (2012) did not observe LEV stability. It has been suggested by Ellington et al. (1996) that spanwise flow transported vorticity to the tip vortex, and therefore was responsible for LEV stability. However, by translating profiles at sweep angles as high as $\Lambda = 45°$ Beem et al. (2012) showed that the spanwise flow in isolation was not responsible for vortex stability, which corroborated previous findings by Birch and Dickinson (2001) that spanwise flow was not responsible for LEV stability on rotating wings. However, nominally-two dimensional spanwise flow, such as that investigated by Beem et al. (2012), cannot result in three-dimensional effects such as the convection of spanwise-oriented vorticity, which depends also on a gradient of vorticity magnitude. Neglecting viscous diffusion, the transport of spanwise-oriented vorticity (ω_z) is governed by the spanwise component of the vorticity transport equation:

$$\frac{\partial \omega_z}{\partial t} + u\frac{\partial \omega_z}{\partial x} + v\frac{\partial \omega_z}{\partial y} + w\frac{\partial \omega_z}{\partial z} = \omega_x\frac{\partial w}{\partial x} + \omega_y\frac{\partial w}{\partial y} + \omega_z\frac{\partial w}{\partial z} \ , \tag{2.1}$$

where the terms from left-to-right represent the rate of change of vorticity due to unsteadiness, convection of vorticity in the streamwise (x), wall-normal (y), and spanwise (z) directions, vortex tilting in the streamwise and wall-normal directions, and vortex stretching, respectively. A hypothetical balance of vorticity is shown in Figure 2.1, where spanwise-oriented vorticity entering the LEV from the leading-edge shear layer is balanced by a spanwise convection of vorticity.

It has been shown by Rival et al. (2014) that LEV attachment is only topologically compatible with vortices smaller than one chord-length c in scale. The vorticity generated in the leading-edge shear layer of a rotating profile must therefore be balanced by either the transport or annihilation of vorticity in order to limit vortex growth as a

necessary condition to LEV stability. A recent study by Wojcik and Buchholz (2014) conducted a vorticity balance within the LEV on a rotating profile, utilizing direct measurements of the circulation transport through the leading-edge shear layer and via spanwise vorticity convection. It was concluded that spanwise vorticity convection was insufficient to balance vorticity production, and that the large residual in the vorticity balance must be accounted for by vorticity annihilation. Similarly, Cheng et al. (2013) found that spanwise vorticity convection was negligible relative to convection in the streamwise and wall-normal directions. However, in natural swimming and flight the full benefit of a stable LEV is realized when the LEV is maintained for at least one half-stroke of motion, rather than an indefinite period. Thus, it is sensible to measure the relative stability of an LEV in terms of its convection speed relative to the profile, as opposed to a binary stable or unstable condition. This relative LEV stability is an important characteristic of natural swimming and flight that has not been investigated in terms of vorticity transport. By comparing profiles of varying rotation rate and sweep angle, the current study investigates the role of both vortex stretching and vorticity convection on relative LEV stability.

2.3 The Moderation of LEV Growth with Vorticity Transport

Based on the limiting length-scale criterion of Rival et al. (2014), low vortex growth rates represent more stable LEVs. This can be accomplished by reducing the LEV feeding velocity, moderating LEV growth through vorticity convection, or contracting LEV size through vortex stretching. Figure 2.1 shows the hypothetical vorticity balance for a flapping profile. The rotational velocity Ω results in a spanwise variation in vorticity magnitude $\partial\omega_z/\partial z$, which couples with spanwise flow w from rotational

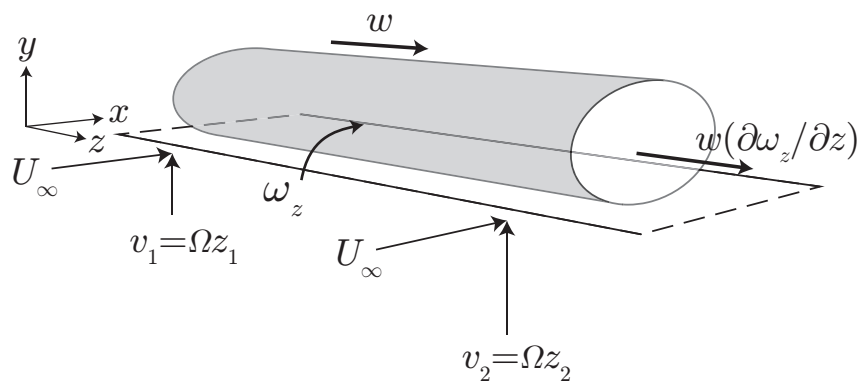

Figure 2.1: A flat-plate profile undergoing a flapping motion has a spanwise variation in effective velocity and spanwise flow, resulting in vortex stretching ($\omega_z(\partial w/\partial z)$) and vorticity convection ($w(\partial\omega_z/\partial z)$). The balance between the spanwise transport of vorticity and vorticity flux through the leading-edge shear layer is hypothesized here as the mechanism of LEV stability.

accelerations to convect vorticity down the span of the profile. This convection of vorticity balances the flux of vorticity into the vortex from the leading-edge shear layer. Vortex stretching acts to modify the size of the vortex, but does not alter the balance of circulation on any two-dimensional slice. It is hypothesized that spanwise vorticity convection moderates LEV strength, while simultaneously vortex stretching can act to limit LEV growth.

2.3.1 The Effect of Reduced Frequency on LEV Saturation

In order to compare the growth rate of an LEV to the limiting length scale of one chord c, it is necessary to produce an estimate for the circulation entering that LEV. A model for the vorticity flux into a leading-edge vortex was proposed and validated by Wong et al. (2013a), shown in Figure 2.2 for a profile experiencing an effective velocity u_{eff} and effective incidence α_{eff}. In the vorticity-flux model, the mass per unit

span m' entering the vortex was described as:

$$m' = \rho \int_0^{t_0}\int_0^{d} u(\xi, t)\ \mathrm{d}\xi \mathrm{d}t\ , \tag{2.2}$$

where ξ is the shear-layer coordinate as shown in Figure 2.2, ρ is the fluid density, d is the shear-layer thickness and u is the shear-layer velocity. Assuming that the shear-layer velocity scales with the effective velocity u_{eff}, this results in a mass flow into the vortex proportional to:

$$\frac{\partial m'}{\partial t} \propto \rho d u_{\text{eff}}. \tag{2.3}$$

Mass entering the vortex has an associated circulation Γ, which can be determined via a path integral around the shear layer. The rate of circulation growth within the LEV is therefore approximately:

$$\frac{\partial \Gamma}{\partial t} = \frac{\partial \Gamma}{\partial m'}\frac{\partial m'}{\partial t} \propto \left(\frac{u_{\text{eff}} l}{\rho d l}\right)(\rho d u_{\text{eff}}) = u_{\text{eff}}^2. \tag{2.4}$$

Didden (1979) derived a similar expression for the rate of circulation growth for a vortex ring generated by a piston-cylinder apparatus:

$$\frac{\partial \Gamma}{\partial t} = \frac{1}{2}U^2\ , \tag{2.5}$$

which scaled well with experimental data, where U was the piston velocity.

As vorticity-containing mass enters the LEV the vortex grows in size, and therefore it reaches its limiting length scale c with an area on the order of c^2. For a period of motion T, comparing the resulting maximum allowable LEV growth of c^2/T to

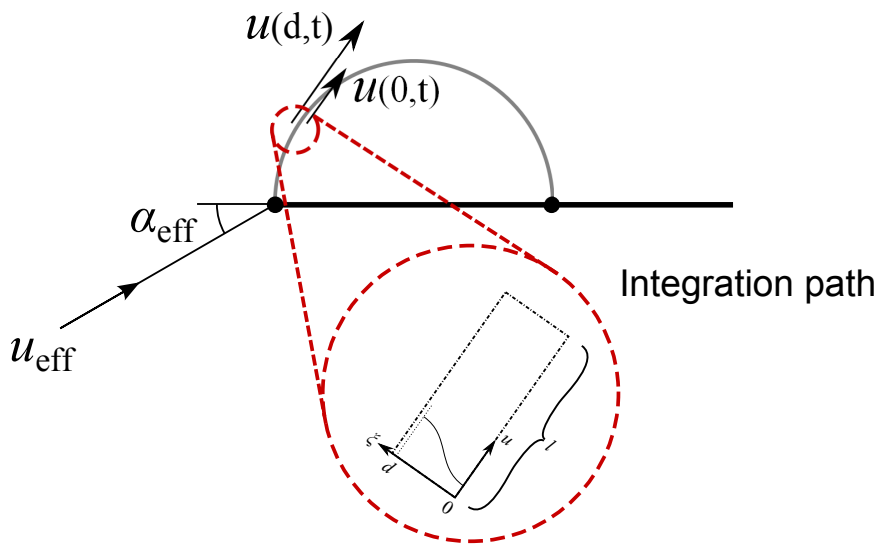

Figure 2.2: The integration of vorticity within a shear-layer segment of length l and thickness d. For a fluid of density ρ, this results in a rate of circulation growth $\frac{\partial \Gamma}{\partial t} = \frac{\partial \Gamma}{\partial m'} \frac{\partial m'}{\partial t}$ of approximately the square of effective velocity u_{eff}^2.

the circulation developed in one period of motion $u_{\text{eff}}^2 T$ gives a relationship analogous with reduced frequency $k = \pi f c / U_\infty$:

$$\frac{c^2/T}{u_{\text{eff}}^2 T} = \left(\frac{fc}{u_{\text{eff}}}\right)^2 \approx \frac{1}{\pi^2}\left(\frac{\pi f c}{U_\infty}\right)^2 = \frac{1}{\pi^2} k^2 \ , \tag{2.6}$$

where $f = 1/T$ is the frequency of motion and U_∞ is the free-stream velocity. Here, larger reduced frequencies represent a larger allowable vortex area for a given expected circulation, or in other words a more stable LEV. This is in agreement with the findings of Baik et al. (2012) that larger reduced frequencies result in more stable LEVs in two-dimensional plunging and pitching cases. It is therefore reasonable to expect that the same parameter is significant to LEV stability in flapping cases as well.

2.3.2 The Effect of Vorticity Convection on LEV Circulation

In addition to having a larger limiting length scale for a given circulation, as estimated by the reduced frequency k above, it is hypothesized that relative LEV stability can be improved by moderating circulation growth with vorticity convection. As done by Wojcik and Buchholz (2014), the rate of circulation change due to vorticity convection can be determined from the integral of the unsteady and spanwise convection terms of the vorticity transport equation across the vortex core area:

$$\int \frac{\partial \omega_z}{\partial t}\, dA = \int -w\frac{\partial \omega_z}{\partial z}\, dA \ . \tag{2.7}$$

Using mean values across the vortex core area, Equation (2.7) reduces to:

$$\frac{\partial \Gamma}{\partial t} = \overline{-w\frac{\partial \omega_z}{\partial z}} A \ , \tag{2.8}$$

where A is the cross-sectional area of the vortex core. The presence of the spanwise flow w indicates that circulation transport, and in turn relative LEV stability, can be improved by the presence of a sweep angle Λ, as suggested by Wong et al. (2013a).

2.3.3 The Effect of Vortex Stretching on LEV Cross-Sectional Area

Vortex stretching acts to increase the centre-line vorticity of a vortex at a constant circulation, such that the vortex must contract in size to conserve momentum. In this way, vortex stretching can improve LEV stability by directly modifying the vortex size, avoiding the critical length scale c. Assuming mean values, vorticity and

circulation are related through the vortex core area:

$$\omega_z = \frac{\Gamma}{A} \ , \tag{2.9}$$

which can be differentiated with respect to time, while holding circulation constant:

$$\frac{\partial \omega_z}{\partial t} = \Gamma \frac{\partial}{\partial t} \frac{1}{A} = -\frac{\Gamma}{A^2} \frac{\partial A}{\partial t} \ . \tag{2.10}$$

This rate of change of vorticity can be substituted with the vortex stretching term of the vorticity-transport equation:

$$\omega_z \frac{\partial w}{\partial z} = -\frac{\Gamma}{A^2} \frac{\partial A}{\partial t} \ , \tag{2.11}$$

which can be rearranged for the rate of vortex growth as:

$$\frac{\partial A}{\partial t} = -\omega_z \frac{\partial w}{\partial z} \frac{A^2}{\Gamma} \ . \tag{2.12}$$

Thus, three factors are expected to improve relative LEV stability: vortex stretching; vorticity convection modified through profile sweep Λ; and increased reduced frequency k. The experimental procedure for investigated these effects are detailed in the following section.

2.4 Methods

All experiments were conducted in a horizontal free-surface water tunnel at the University of Calgary, while model kinematics were produced with a custom six degree-of-freedom hexapod manipulator. A detailed description of these facilities can be

found in Wong et al. (2013a). The water-tunnel test section has a diverging rectangular cross section with a mean width of 385mm. Water depth was maintained at 432mm. The hexapod manipulator was mounted above the water-tunnel test section. The current study investigates root-flapping kinematics on aluminium flat-plate profiles. These flat-plate profiles were oriented vertically with zero geometric angle of attack relative to the free-stream. In order to minimize free-end effects such as the inboard-directed spanwise flow or vortex compression observed by Hartloper et al. (2013), the model pierced the free surface in each test case and maintained a tip-gap with the water-tunnel floor of less than 3mm. The axis of the root-flapping motion was in the streamwise direction and fixed at the water-tunnel floor, maintained as a virtual hinge by the hexapod. The reference rotation profile for all test cases is shown in Figure 2.3, where the profile starts from rest and undergoes a sinusoidal ramp-up over a period of time t_r to the peak rotational speed $\Omega_{\max}$. The peak rotational speed $\Omega_{\max}$ is then maintained for a set period of time t_c, and then finally the profile is returned to rest with a sinusoidal ramp-down over t_r.

In order to compare the rotating cases investigated here to two-dimensional cases from the literature, it is possible to define a modified Strouhal number based on the displacement of the mid-span of the flapping profile:

$$St^* = \frac{(R\phi_{\max})f}{U_\infty} \ , \tag{2.13}$$

where $\phi_{\max}$ is the maximum angular displacement of the profile, R is the physical profile span, and f is the frequency of motion. $R\phi_{\max}$ is therefore the displacement of the half-span $R/2$ over a range of $\pm\phi_{\max}$. In order to determine the point at which St^* diverges from St, a large range of modified Strouhal numbers St^* and

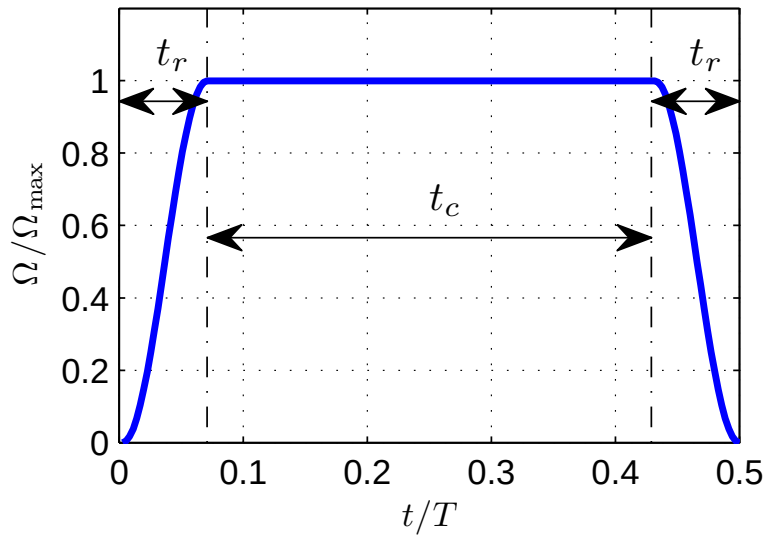

Figure 2.3: The prescribed velocity of the flat-plate profiles follow three sections: a sinusoidal ramp-up from zero velocity to maximum velocity over a period t_r; a constant velocity section over a period t_c; and a sinusoidal ramp-down over a period t_r. The duration of the constant-velocity section is varied in order to vary Strouhal number.

reduced frequencies k were investigated using phase-averaged planar Particle Image Velocimetry (PIV). Subsequently, vorticity transport on swept and unswept profiles at the specific modified Strouhal number St^* that diverged from two-dimensional cases ($St^* = 0.54$) were investigated using three-dimensional Particle Tracking Velocimetry (3D-PTV). The exact parameter space, as well as a detailed description of the PIV and 3D-PTV setups, are found below.

2.4.1 Parameter Space

The range of modified Strouhal numbers St^* and reduced frequencies k that were investigated in this study are shown in Figure 2.4. The parameter space of Baik

et al. (2012) is superimposed, as it is used as a reference in Section 2.5 in order to determine the effect of the modified Strouhal number St^* in comparison to the Strouhal number St. In order to vary the flapping frequency without changing the effective angle of attack α_{eff} the velocity profile was modified from the reference profile shown in Figure 2.3 by varying the duration of constant rotational speed t_c while maintaining the ramp-up and ramp-down duration t_r. By simultaneously varying the profile chord length and peak speed duration t_c, both reduced frequency and modified Strouhal number could be varied independently over the range $St = 0.33$, 0.45, and 0.54 and $k = 0.45$, 0.89, and 1.33. The varying chord length resulted in varying Reynolds numbers; however, the effect of Reynolds number on LEV convection speed is secondary within the range $200 \leq Re \leq 60000$, as shown by Garmann et al. (2013). Nevertheless, the variation in Reynolds number was kept as small as possible by varying the water-tunnel temperature between 20°C and 40°C, resulting in a range of $1875 \leq Re \leq 7500$ for all cases. Following the identification of the modified Strouhal numbers St^* and reduced frequencies k with large three-dimensional effects, a sweep angle Λ was included as an additional parameter to vary spanwise vorticity convection. Two sweep angles were considered: $\Lambda = 0°$ and 45°.

2.4.2 PIV Setup

A 1W continuous-wave laser ($\lambda = 532nm$) was used to illuminate a spanwise-oriented plane at the half-span of each test case. The flow was seeded with silver-coated hollow glass spheres of $100\mu m$ diameter, with a Stokes number of 2.4×10^{-3}. Images of the flow were captured with a Photron SA4 high-speed camera at a frame rate of $250Hz$ and a pixel resolution of 1024×1024. The images were subsequently processed with

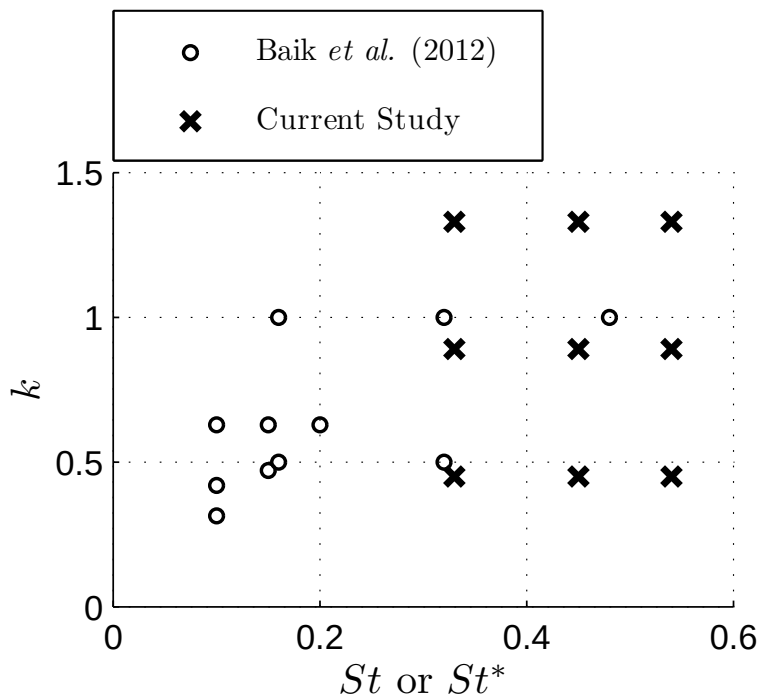

Figure 2.4: The $k - St^*$ parameter space for the current study. The $k - St$ parameter space of the two-dimensional study by Baik et al. (2012) is superimposed for comparison. The first stage of this study is to determine when three-dimensional effects begin to dominate vortex growth.

LaVision DaVis 8.1.3. Profile motions were repeated and captured ten times per test-case, and the results were then ensemble-averaged in order to produce the final vector fields. Vortex core identification followed the γ_1 criterion detailed by Graftieaux et al. (2001):

$$\gamma_1(P) = \frac{1}{N} \sum_S \sin \theta_M, \tag{2.14}$$

where θ_M is the angle formed between the velocity $\vec{u}(M)$ at point M and the vector $\overrightarrow{PM}$ to the point M from the point of interest P, while N is the number of points M inside the region S.

2.4.3 3D-PTV Setup

The features of the 3D-PTV setup are illustrated in Figure 2.5. A high-intensity discharge lamp was used as a light source to illuminate a streamwise-oriented cylindrical control volume centred at the mid-span of each test profile, after being collimated with a 300mm primary and 40mm secondary lens. The measurement volume had a diameter of 80mm and a length of approximately 200mm. The light column entered the water tunnel vertically and was reflected into the streamwise direction with a mirror approximately 15 chords downstream of the test profiles. The effect of the mirror on the flow within the control volume was tested by measuring the flow in an otherwise empty channel and checking that the pathline curvature was in fact negligible, and that the flow velocity was undisturbed. The same seeding particles were used as in the PIV experiments, but at a substantially lower seeding density. Images of the flow were captured with four pco.Edge sCMOS cameras at a frame rate of $165Hz$ and a pixel resolution of 2560×1280. The Lagrangian velocities and accelerations were determined by differentiation of the particle tracks. The mean inter-particle distance was approximately 3mm during the experiments. For each test case ten Lagrangian datasets were superimposed and interpolated onto an Eulerian grid with 4mm grid spacing. Vortex core identification followed a normalized helicity criterion detailed by Levy et al. (1990):

$$H_n = \frac{\vec{u} \cdot \vec{\omega}}{|\vec{u}||\vec{\omega}|} \ , \tag{2.15}$$

where in the limiting case of $H_n = \pm 1$, the local vorticity and velocity vectors are parallel.

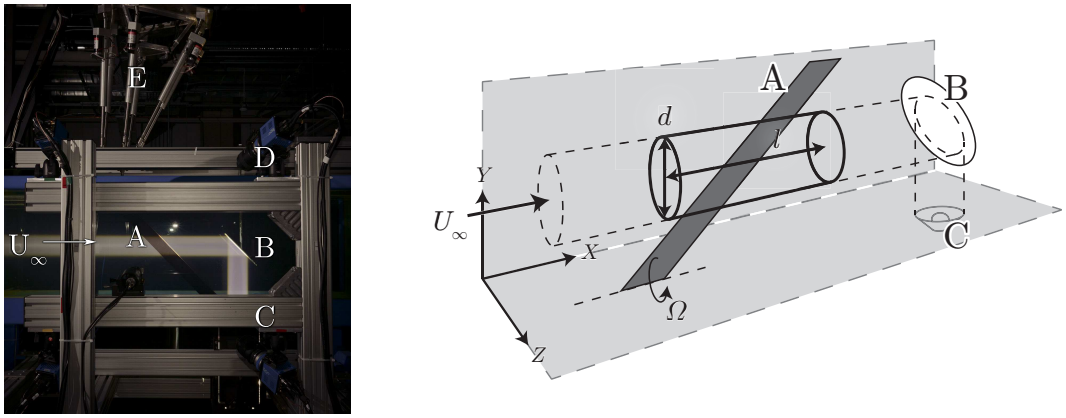

(a) experimental setup (b) schematic of control volume

Figure 2.5: Swept and unswept flat-plate profiles (A) manoeuvre through the cylindrical PTV control volume of length $l = 200mm$ and diameter $d = 80mm$. The volume is illuminated with the aid of a mirror (B) reflecting light upstream from a HID lightsource collimated with 40mm and 300mm lenses (C). Also shown are the four pco.Edge sCMOS cameras (D) and the hexapod manipulator (E). The mirror (B) was moved upstream relative to the real experimental setup for the purposes of this photo.

2.5 Results

In the following we will test the hypotheses proposed in Section 2.3 with direct measurements of vorticity transport. However, the modified Strouhal numbers and reduced frequencies that produce strong spanwise vorticity transport will first be determined via planar PIV at the midspan position.

2.5.1 The Effect of the Modified Strouhal Number and Reduced Frequency on Vortex Development

Vortices were tracked over the range of modified Strouhal numbers $St^* = 0.33$, 0.45 and 0.54, and reduced frequencies $k = 0.45$, 0.89 and 1.33 utilizing the γ_1 criterion, as shown in Figure 2.6 for $t/T = 0.5$. Vortex-core convection speed decreases with

increasing reduced frequency, similar to two-dimensional plunging cases. The dependence on reduced frequency is seen much more clearly in Figure 2.7, which shows the displacement of the γ_1 peak over the range of phases $0.1 \leq t/T \leq 0.5$. Here it is shown that vortex-core displacement varies only with respect to reduced frequency, while the modified Strouhal number plays no role. The dependence on reduced frequency suggests that the ratio between the maximum allowable growth rate of the LEV and the feeding of circulation into the LEV (from the leading-edge shear layer) determines LEV stability, as suggested by Equation (2.6).

Baik et al. (2012) observed that LEV circulation decreased with increasing reduced frequency for two-dimensional plunging cases, which is also observed for the flapping cases in the current study, again seen in Figure 2.7. However, while two-dimensional plunging cases showed that circulation had only a low dependence on Strouhal number, the $St^* = 0.54$ cases exhibit a drastically increased circulation to that of the other modified Strouhal numbers. The large variation in circulation with respect to St^* suggests that the investigated flapping cases cannot be approximated as bulk two-dimensional at these increasingly faster motions. Therefore, as the $St^* = 0.54$ cases bare the least resemblance to two-dimensional plunging, these cases will be investigated with 3D-PTV below in order to determine how spanwise vorticity transport affects LEV stability.

2.5.2 The Effect of Vorticity Transport on Vortex Development

Despite the divergence between St and St^* for $St^* \geq 0.54$, LEV stability is determined by the reduced frequency k alone, similar to two-dimensional plunging cases.

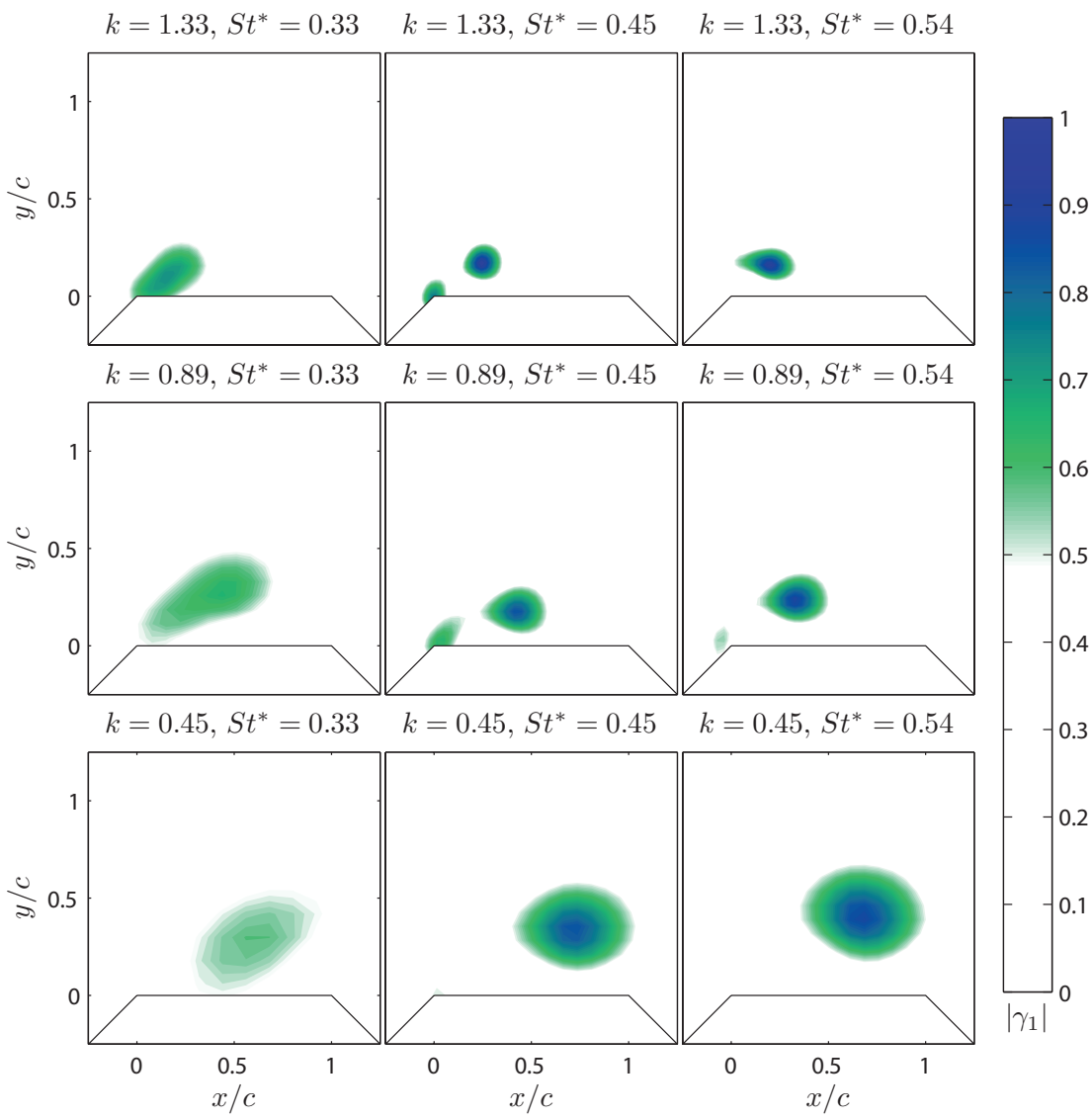

Figure 2.6: Vortex-core locations were determined with the $|\gamma_1|$ criterion and tracked through time, shown here for all modified Strouhal numbers St^* and reduced frequencies k tested, at the phase $t/T = 0.5$. The modified Strouhal number does not effect vortex convection speed.

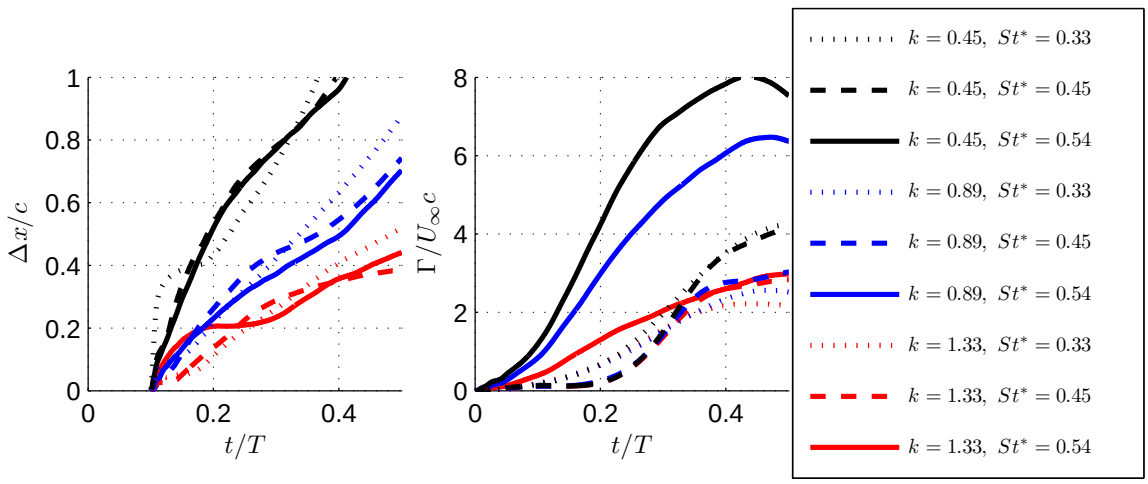

Figure 2.7: Vortex locations are tracked, relative to $t/T = 0.1$, showing a collapse of LEV displacement as a function of reduced frequency k (left). Vortex circulation is affected by both modified Strouhal number St^* and reduced frequency k: larger k results in a lower circulation Γ; sensitivity to St^* is low until $St^* = 0.54$, at which point dramatic increases in circulation are observed (right).

Therefore, at first glance the influence of vorticity transport on LEV stability appears to be secondary. In order to reconcile this observation with the hypotheses in Section 2.3, a profile sweep Λ can be introduced in order to vary vorticity convection by varying the spanwise flow, thus acting as a vorticity sink. Figure 2.8 shows isosurfaces of vorticity magnitude and vorticity convection for two sweep angles $\Lambda = 0°$ and 45° and two reduced frequencies $k = 0.89$ and 1.33, as measured with 3D-PTV. Vorticity convection magnitude is found to increase both with increasing reduced frequency and increasing profile sweep, which can also be seen in Figure 2.9. The spanwise flow, circulation, vorticity transport and vortex convection shown in Figure 2.9 were measured at the mid-span of each profile, and values for vorticity convection, vortex stretching and spanwise flow were determined from the average value within an isolevel of vorticity $\omega_z c/U_\infty = 5$. The vortices are tracked using the maximum

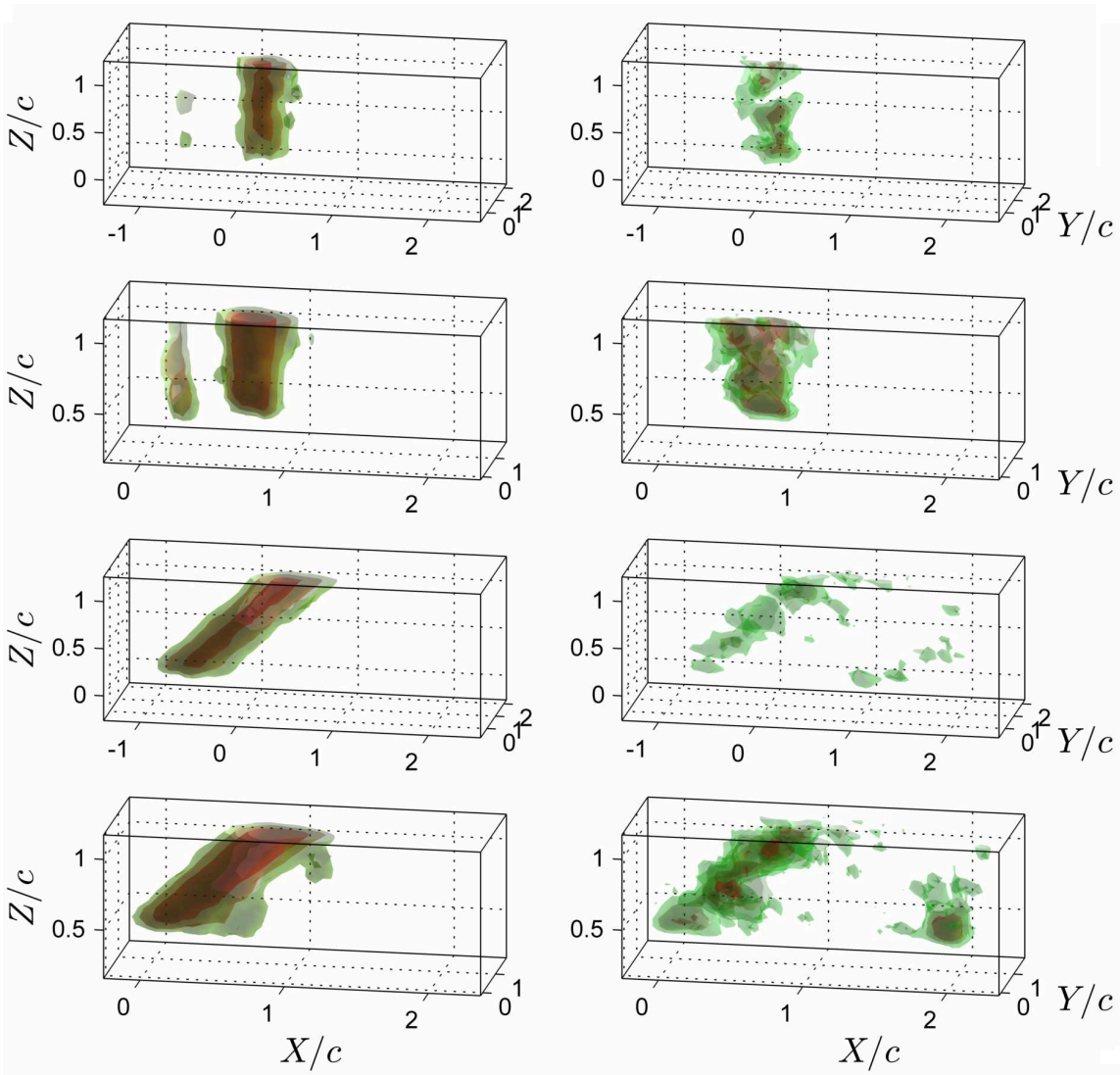

Figure 2.8: Isosurfaces of vorticity magnitude ($\omega c/U_\infty = 5$, 10, and 20) are shown for phase $t/T = 0.5$ in the left column, and isosurfaces of vorticity convection ($w\frac{\partial \omega_z}{\partial z}\frac{c^2}{U_\infty^2} = 20$, 50, and 100) are shown in the right column. From top to bottom the four cases shown are: $k = 0.89,\ \Lambda = 0°$; $k = 1.33,\ \Lambda = 0°$; $k = 0.89,\ \Lambda = 45°$; and $k = 1.33,\ \Lambda = 45°$.

normalized helicity criterion over the range $0.2 \leq t/T \leq 0.4$, as a strong peak of normalized helicity was observed across this interval.

The ability of profile sweep to modulate spanwise vorticity transport agrees with

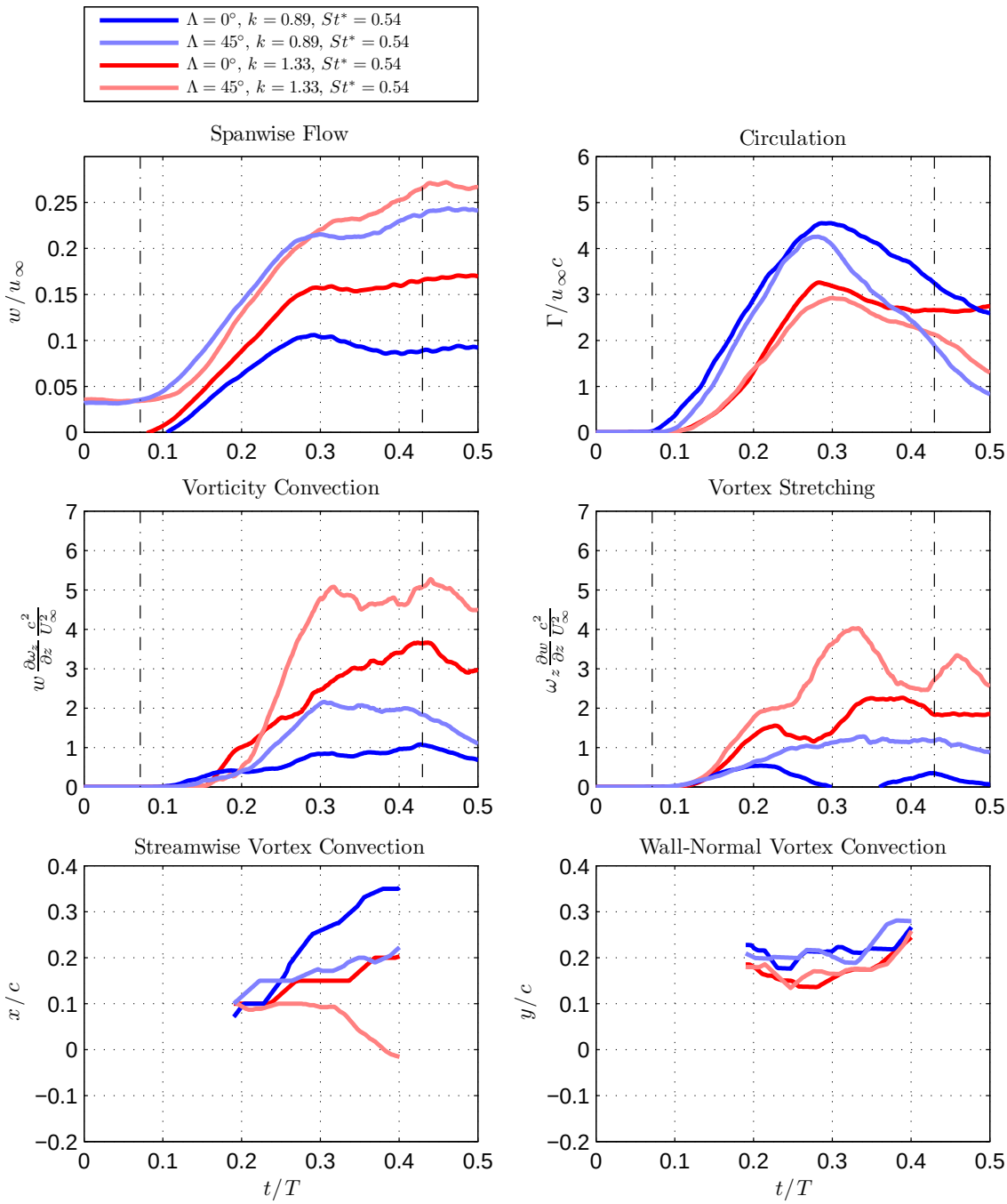

Figure 2.9: Spanwise flow, vortex circulation, vorticity transport and vortex location are plotted for four test cases. Streamwise vortex position shows a large dependence on both sweep angle and reduced frequency. This sensitivity to reduced frequency can be explained in terms of the limiting length scale of the profile chord for stable LEV growth.

the findings of Wong et al. (2013a). Increased spanwise vorticity transport corresponds to a reduced LEV convection speed, and both higher sweep angles and higher reduced frequencies result in a slower streamwise vortex convection. However, the effect of vortex stretching and vorticity convection on streamwise vortex convection is not linear. For instance, the $\Lambda = 45°,\ k = 0.89$ case and the $\Lambda = 0°,\ k = 1.33$ case have nearly identical vortex convection paths despite having very different levels of vorticity convection and vortex stretching. In other words, relative LEV stability is increased by two mechanisms: (1) the addition of vorticity sinks, such as from profile sweep; or (2) the reduction of vorticity feeding for a given limiting length scale c. This latter mechanism of increasing LEV stability is governed by the reduced frequency, as shown in Section 2.3.

2.6 Discussion

In Section 2.3 it was predicted that both larger reduced frequencies and larger sweep angles would result in more stable LEVs on flapping profiles. Even in the rotating cases investigated here, the reduced frequency was found to govern the ratio between the limiting growth rate of the LEV (c^2/T) and the feeding of circulation into the LEV from the leading-edge shear layer ($u_{\text{eff}}^2 T$). Meanwhile, larger sweep angles result in larger spanwise vorticity transport, acting as a vorticity sink.

For rotating cases, the vorticity feeding rate is a function of the profile span. Therefore, while aspect ratio sensitivity was not investigated explicitly in this study, the reduced frequency is analogous to the aspect ratio AR for rotating profiles:

$$k \approx \frac{\pi f c}{u_{\text{eff}}} \approx \frac{\pi f c}{\Omega R} \approx \frac{\pi f}{\Omega AR} \ , \tag{2.16}$$

where R is the profile span. Larger reduced frequencies k represent larger allowable LEV growth rates relative to shear-layer feeding, and thus more stable LEVs. In turn, the most stable LEVs also correspond to the smallest aspect ratios, similar to the findings of Lentink and Dickinson (2009b). This analogy between the aspect ratio AR and the reduced frequency k of course neglects effects such as vorticity convection and vortex stretching, which have been shown here to also improve relative LEV stability.

In addition to vorticity transport, Wojcik and Buchholz (2014) found that vorticity annihilation was a significant mechanism for regulating LEV growth and was generally much larger in magnitude than vorticity convection. However, as an extension to these findings, it has been shown here that relative LEV stability can be improved by moderating LEV growth through vorticity convection and vortex stretching.

Finally, with respect to the findings of Beem et al. (2012) that profile sweep does not affect LEV stability for plunging cases, it was found that profile sweep did, in fact, affect LEV stability for flapping cases in contrast with plunging cases. The addition of spanwise flow from profile sweep increased the vorticity transport that was already present for the rotating, unswept cases, in agreement with the findings of Wong et al. (2013a). Beem et al. (2012) had ignored rotating cases in their study on purely plunging profiles. The current result demonstrating the effect of profile sweep alludes to the evolutionary convergence of swept profiles found in nature ranging from large marine animals down to small flapping birds, and provides us with a step forward towards designing more efficient autonomous vehicles and energy extraction devices.

2.7 Conclusions

In this study relative LEV stability on impulsively-started flapping profiles was proposed and tested using phase-averaged planar PIV and volumetric 3D-PTV measurements. The circulation flux into an LEV from the leading-edge shear layer was moderated by the spanwise convection of vorticity. Moreover, vortex stretching was observed to limit LEV growth and further enhance relative LEV stability.

This study resulted in the following primary conclusions:

(1) The ratio between the limiting length scale of an LEV (the profile chord) and the shear-layer feeding rate can be approximated by the reduced frequency k, with larger reduced frequencies increasing LEV stability. In the specific case of rotating profiles, the shear-layer feeding rate is a function of the profile span. It is therefore speculated that the ratio between the limiting length scale of an LEV and the shear-layer feeding rate depends on the aspect ratio AR, with smaller aspect ratios increasing LEV stability in agreement with Lentink and Dickinson (2009b);

(2) In addition to the above ratio, LEV stability can be improved by draining vorticity through spanwise vorticity transport. Spanwise vorticity transport, and therefore LEV stability, can be increased by introducing profile sweep. This effect may explain the ubiquity of profile sweep in natural swimming and flying, throughout length scales ranging from the wings of small birds to the flukes of whales.

2.8 Acknowledgements

The authors gratefully acknowledge the support of the U.S. Air Force Office of Scientific Research under grant number FA9550-13-1-0117, monitored by Dr. Douglas Smith.

Chapter 3

Rapid manoeuvring with spanwise-flexible wings

3.1 Abstract

In this study, it is hypothesized that spanwise-profile bending contributes towards limiting leading-edge vortex (LEV) growth and increasing LEV stability in natural swimming and flight, due to the spanwise flow produced by profile bending. Specifically, as a propulsor undulates and subsequently bends, the profile tip can have a phase lag relative to the root, producing both a spanwise flow and an angle-of-attack gradient, transporting vorticity and thus circulation along its span. This relative phase of the profile tip versus the root is investigated experimentally using a combined pitching-and-flapping motion on a nominally two-dimensional NACA0012 profile, utilizing direct measurements of vorticity transport to estimate the circulation budget. In order to measure vorticity transport the entire velocity gradient tensor must be resolved, and therefore 4D-PTV, a high-density, time-resolved volumetric technique, was used to measure the flow around the profile. Tip-leading kinematics were found to increase LEV size and strength due to an unbalanced circulation budget: vorticity was not transported along the span, but instead accumulated to

increase circulation. Meanwhile for tip-lagging kinematics, that mimics the bending found in nature, both reduced LEV size and circulation were observed, as vorticity transport acted to balance the circulation budget instead.

3.2 Introduction

Previously, spanwise flexibility has been studied in terms of cruising efficiency. For instance, Heathcote et al. (2007) observed increased propulsive efficiencies for oscillating spanwise-flexible profiles, while Cleaver et al. (2016) observed increased lift coefficients and reduced power coefficients for flexible profiles across a broad range of kinematics. In such cruise conditions, Lucas et al. (2014) found broad evolutionary convergence among flexible appendages, with similar levels and locations of profile bending across a range of Reynolds numbers and species. Similar efficiencies have been observed for flexibility about other axes such as chordwise and twisting deformations, as demonstrated by Young et al. (2009) and Cleaver et al. (2014), respectfully. Taking inspiration from these advantages found for cruising conditions, the current study investigates the role of spanwise flexibility during rapid maneuvers.

Ellington et al. (1996) identified spanwise flow as critical in controlling the growth of the ubiquitous leading-edge vortex (LEV). This LEV is especially important for rapidly maneuvering flyers as the bound vortex is of negligible strength on thin, stalled airfoils, as discussed by Pitt Ford and Babinsky (2013). Thus, maintaining the proximity of this vortex to the profile of a swimmer or flyer is critical in maintaining high instantaneous loads, which is useful for rapid maneuvering and lift augmentation. The proximity of the vortex to the profile is determined by the relative streamwise velocity of the vortex. Wong and Rival (2015) showed that this streamwise convection

speed can be reduced by draining circulation from the LEV through spanwise vorticity convection, as the vortex-detachment process is determined by the vortex size. In particular, Rival et al. (2014) showed that for a critical vortex size on the order of one chord length, the detachment process is forced to begin by the streamline topology. For rotating kinematics, rotational accelerations can provide the spanwise flow required to maintain a constant vortex size in steady state, as discussed by Lentink and Dickinson (2009b). In particular, Lentink and Dickinson (2009b) described rotational accelerations with the Rossby number, with smaller values of the Rossby number corresponding to stronger rotational accelerations, and Rossby numbers on the order of $Ro \approx O(1)$ were associated with stable LEVs. Stable LEVs have been observed in this Rossby number range by Ozen and Rockwell (2012), Cheng et al. (2013), and others. At such low aspect ratios, Cheng et al. (2013) observed that convection of the LEV in the remaining two directions, streamwise and chord-normal, as well as vortex tilting, may also be critical in maintaining LEV stability. However, flapping flyers with lower rotational accelerations, or higher Rossby numbers, must pursue alternative strategies. For instance, a flapping profile initially perpendicular to the oncoming flow will passively bend along its profile span due to the lift it generates, resulting in a component of oncoming flow parallel with the span. As all natural propulsors are flexible, it follows that this spanwise flow may be exploited to manipulate LEV growth. However, merely producing any spanwise flow is not sufficient to limit the circulation of the LEV. Beem et al. (2012) showed that a nominally two-dimensional spanwise flow from uniform profile sweep does not limit LEV growth or improve LEV stability. Rather, to produce a stable vortex the circulation produced in the leading-edge shear-layer must be somehow balanced by a vorticity

sink. For spanwise flow to act as a vorticity sink, it must couple with a gradient of vorticity magnitude in order to convect vorticity along the profile span. Wong and Rival (2015) has shown that this vorticity convection is able to partially balance the circulation produced in the leading-edge shear-layer of a profile. At low Reynolds numbers, Wojcik and Buchholz (2014) further identified vorticity annihilation as a major vorticity sink, although spanwise convection becomes increasingly important at higher Reynolds numbers. Wong and Rival (2015) gives the spanwise circulation transport as:

$$\frac{\partial \Gamma}{\partial t} = \overline{-w\frac{\partial \omega_z}{\partial z}}A \ , \tag{3.1}$$

where the mean spanwise-vorticity convection is taken over the vortex area A. In the case of spanwise profile bending, the spanwise flow w can be estimated geometrically from the component of the local flapping velocity that is tangential to the span of the deformed profile. However, estimating the spanwise vorticity gradient $\frac{\partial \omega_z}{\partial z}$ requires the assumption that spanwise distribution of vorticity magnitude will scale with the distribution of circulation, given an approximately constant LEV area A.

Given this scaling relationship between vorticity magnitude and circulation, we speculate that spanwise profile bending controls LEV stability through the following mechanisms. First, a higher vorticity magnitude is anticipated in spanwise locations with a larger effective velocity or effective angle of attack. In order to accomplish this, a higher profile displacement and a higher effective velocity will be prescribed towards the tip of the profile in the experimental setup to follow. Second, a spanwise flow must be produced, through profile bending, rotation or sweep, to couple with this vorticity gradient and convect vorticity along the span of the profile. A flying animal can exploit this convection to control LEV circulation, either increasing it

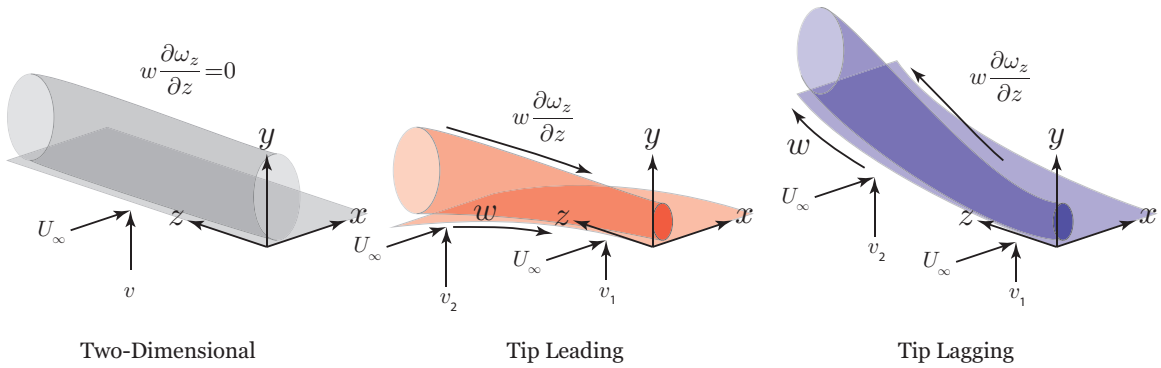

Figure 3.1: A two-dimensional plunging wing provides a reference with which to compare tip-leading and tip-lagging kinematics (grey). It is hypothesized that a tip-leading motion directs vorticity convection towards the wing root, reducing LEV stability (red). Meanwhile, a tip-lagging case is expected to direct vorticity convection away from the wing root, improving LEV stability by balancing the circulation generated at the leading-edge (blue). Here, U_∞ is the free-stream velocity, while v is a vertical velocity from plunging of flapping motions at points along the span 1 and 2.

to produce higher instantaneous force coefficients, or reducing it in order to prolong LEV attachment.

While a passively bending profile is expected to deform away from the direction of motion, it is interesting to consider the consequences of a flyer bending their wing actively into the direction of flapping. This active bending would reverse the direction of spanwise flow, for instance to alter the circulation budget of the LEV to increase vortex strength at the cost of LEV stability. Thus, we can consider three general bending cases: 'passive' bending away from the direction of motion, 'active' bending into the direction of motion, and rigid profiles that do not bend. Herein, these cases will be referred to by the phase of the profile tip relative to the root, where bending away from the direction of flapping produces a tip-lagging phase, bending into flapping produces a tip-leading phase, and a rigid case has no phase change, respectively.

The augmentation of circulation through profile bending is illustrated for each of

the two-dimensional, tip-leading, and tip-lagging cases in Figure 3.1. First, in the two-dimensional case no spanwise gradients or spanwise flow is present, and a two-dimensional vortex is expected to form. Second, in the tip-leading case it is expected that vorticity magnitude grows towards the profile tip while spanwise flow is directed towards the root, resulting in a negative vorticity transport, increasing circulation and reducing LEV stability. Lastly, in the tip-lagging case, vorticity magnitude is expected to grow towards the profile tip while spanwise flow remains directed outboard, reducing circulation and increasing LEV stability. Therefore, it is hypothesized that tip-lagging kinematics directs circulation along the profile span towards the profile tip, mediating LEV growth, and thus stabilizing the vortex structure and extending force augmentation. Meanwhile, tip-leading kinematics directs circulation inboard, increasing LEV growth, and therefore increasing force generation at the cost of reducing LEV stability. In order to produce tip-leading and tip-lagging profile kinematics to test the above hypothesis, a combined pitching-flapping system was developed in order to manipulate a nominally two-dimensional profile, outlined in the following section.

3.3 Methods

Isolating the effects of tip-leading versus tip-lagging kinematics poses a number of experimental challenges. For instance, if passively-flexible structures are used, the possibility of animals actively deforming their propulsors can be obscured. In particular, selecting particular materials and root kinematics that produce tip-leading and tip-lagging motions constitute additional constraints, which can obfuscate the relationship between profile bending and vortex growth. As such, in this study a

first-approximation to the kinematics of spanwise-flexible profiles was produced using a combined pitching and flapping motion of a rigid profile instead. Note that in this case, we are assuming negligible effects from the free ends. Previously, Bansmer and Radespiel (2012) have similarly sought to investigate combined pitching and flapping while avoiding free-end effects, using rubber segments to bridge their apparatus with wind tunnel walls. Such a method was not possible given the physical limitations of a towing tank, so here the tip gaps were merely kept as small as practicable, detailed below. This methodology is demonstrated in Figure 3.2, where the history of effective angle-of-attack of a hypothetical spanwise-flexible profile is extracted at the profile root and tip, and then is subsequently applied to a rigid profile undergoing a combined pitching and flapping motion:

$$\alpha_{\text{eff}} = \alpha_{\text{geo}} + \tan\left(\Omega R / U_\infty\right) \ , \tag{3.2}$$

where α_{geo} is the pitching angle, and ΩR is the flapping velocity at the mid-span.

Herein, the kinematics of the hypothetical profile will be referred to as the *modeled* motion, while the pitching-flapping analogue will be referred to as the *physical* motion. The specific modelled motion, along with the corresponding physical motion required to generate the same angle-of-attack history, is shown in Figure 3.3. This pitching-flapping analog captures the angle-of-attack history of a spanwise-flexible profile at the root and tip, and approximates the angle-of-attack gradient linearly between these two points. No twisting or deformation of the physical wing is required. Meanwhile, as spanwise flow can only be directed towards the profile tip in this arrangement, when the angle-of-attack gradient is reversed the physical profile tip will represent the modeled profile root and vice versa. The approximation of plunging with pitching

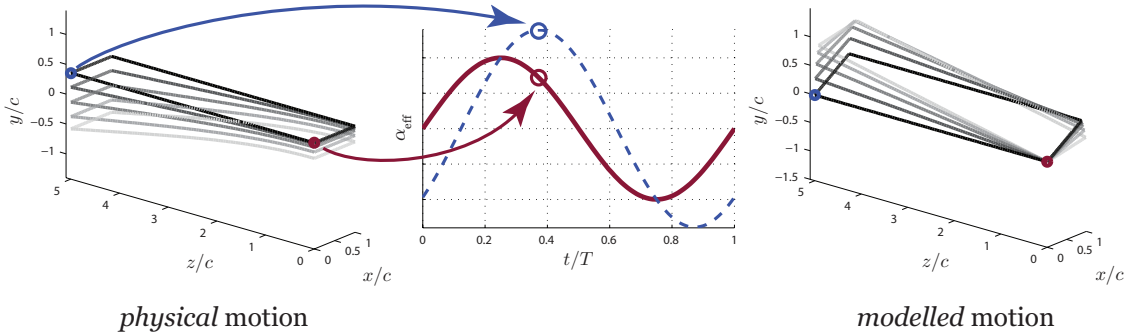

Figure 3.2: The angle of attack experienced at the tip of a flexible profile has a phase-lead or lag relative to the root, as well as a change in magnitude (left). The effective incidence at the root and the tip, shown in blue and red, respectively, can be recorded (centre). By carefully combining pitching and plunging motions, the same angle-of-attack history can be prescribed onto the root and tip of a rigid wing through combined pitching and flapping (right).

in this way is imperfect. However, as the purpose of this study is to investigate the applications of various combinations of spanwise angle-of-attack gradient and spanwise flow on LEV formation, as opposed to a true model of a flexible wing, these approximations are not expected to affect the conclusions of this study. Thus, the physical pitching and flapping motion is intended to mimic the vorticity transport properties of the modeled spanwise-flexible profile, and the system allows the modeled root kinematics and profile flexibility to be adjusted independently of one another.

Given this approach, a single set of profile kinematics within the bounds of natural flight can be defined for the modelled motion, while the tip can be modelled with a phase lead or lag relative to the root independently. Prescribing a harmonic plunging motion, the model root kinematics are defined entirely by two dimensionless parameters: the Strouhal number $St = \frac{f(2h_0)}{U_\infty}$, where f is the frequency of motion and h_0 is the plunging amplitude; the reduced frequency $k = \frac{\pi f c}{U_\infty}$, where c is the profile

chord; and the Reynolds number Re. In this study, the Strouhal number was selected to match the evolutionary convergence of propulsion found in nature by Taylor et al. (2003) of $St = 0.25$. This Strouhal number range is also low enough to avoid the lift-reducing formation of an LEV dipole, reported by Cleaver et al. (2016) for Strouhal numbers of $St > 1$. Meanwhile, the Reynolds number has been shown by Garmann et al. (2013) to have only a secondary effect on LEV size and convection within the range $10^2 \leq Re \leq 10^5$, and therefore a Reynolds number of $Re = 10^5$ was selected with enforced turbulent boundary layers. The range of reduced frequencies found in nature vary substantially even within a single species, for instance Tobalske and Dial (1996) observed that magpies fly with an approximately constant wing beat frequency across their entire flight envelope, resulting in a range of reduced frequencies $0.1 \leq k \leq 0.5$. Furthermore, Baik et al. (2012) found that only reduced frequencies lower than approximately $k \leq 0.5$ resulted in LEV detachment before the airfoil reached the bottom of the motion, due to the timescale of LEV development relative to profile motion. Therefore, as we are interested specifically in the timescales of LEV detachment, a reduced frequency of $k = 0.4$ was selected in order to produce a highly unsteady motion where LEV detachment was nevertheless expected.

As the modelled tip kinematics can be imposed arbitrarily, it was decided to match the flexion observed by Lucas et al. (2014), equivalent to a flexion angle of $\pm 25°$ at the 60% span location. Lastly, a 'rigid' two-dimensional case with no physical flapping motion was included as a reference. The modelled effective incidence for each of these three cases is shown in Figure 3.3, along with the corresponding physical pitching and flapping programs of each case. The average effective angle-of-attack is the same for the tip-leading and tip-lagging cases. Both here and in the results section, the time

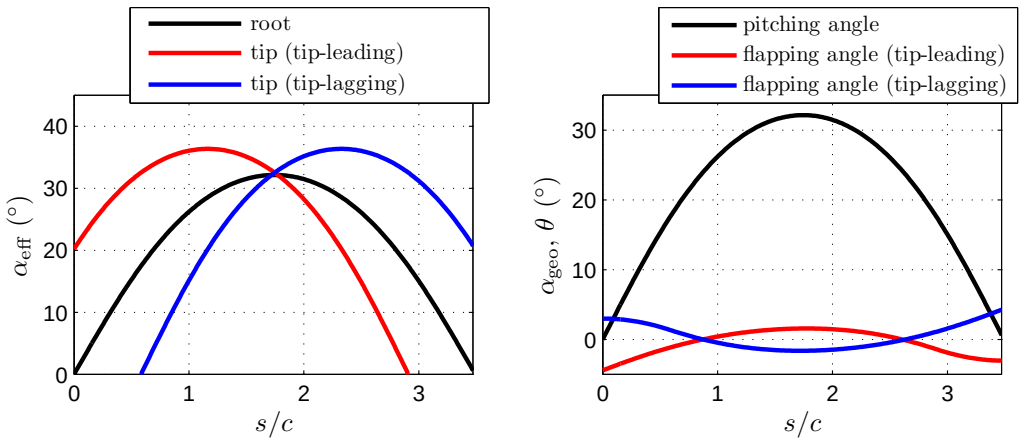

(a) (b)

Figure 3.3: (left) The modelled motion consisted of a common effective incidence α_{eff} at the root for all three cases (black). Meanwhile, the modelled deformation resulted in a different effective incidence history at the profile tip for the tip-leading case (red) and tip lagging case (blue). (right) This effective incidence history resulted in a common pitching angle α_{geo} (black) for all three cases, and flapping angles θ for the tip-leading (red) and tip lagging (blue) cases as shown.

coordinate is indicated in chords travelled s/c from the onset of pitching motion.

All experiments were performed in the optical towing-tank facility at Queen's University, which has a $15m$-long test section, and a $1m \times 1m$ cross-section with three-sided optical access, as shown in Figure 3.4. The towing tank is enclosed by a roof along its length to minimize free-surface effects, with a $50mm$ opening through which test articles can be mounted and towed. The test article chosen was a NACA0012 airfoil with $0.3m$ chord and $1m$ span, which spanned from the roof to the floor in order to minimize tip effects. The effectiveness of turbulators has been shown by Lissaman (1983) to diminish towards Reynolds numbers of 10^5, suggesting that the occurrence of laminar separation is rare after this point. However, as the efficiency of the airfoil is not critical in this study a z-type turbulator was nevertheless included

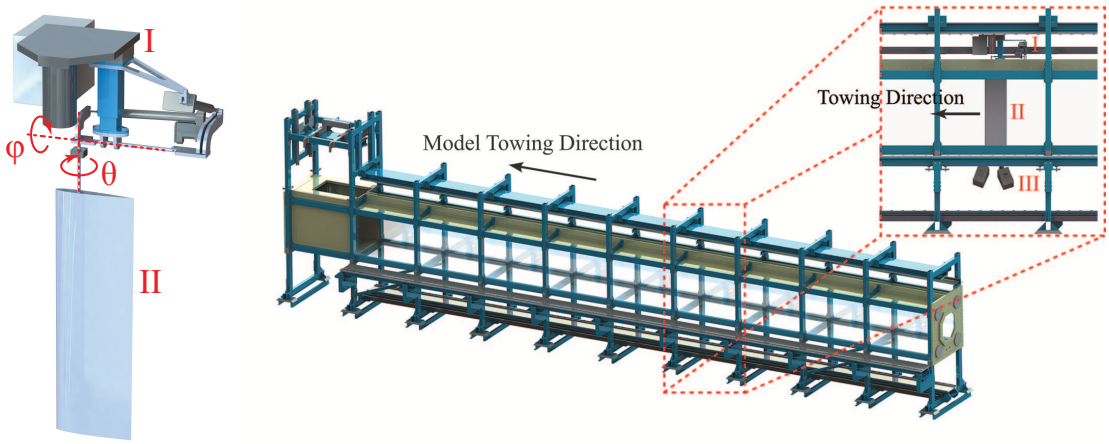

(a) (b)

Figure 3.4: (a) A pitching-flapping mechanism (I) was use to actuate the NACA0012 profile (II) as it was towed along the 15m-long optical towing tank (b). Pitching and flapping axes are labeled ϕ and θ, respectively. The flow-field around the profile was illuminated from the side-wall with a high-speed laser, and was subsequently captured with a four-camera 4D-PTV setup (III), which was located below the glass floor.

at the 20% chord position in order to fully ensure attached boundary layers prior to the pitching-flapping manoeuvre. Wall gaps at both the root and tip were kept as small as possible in order to minimize free-end effects while accommodating the profile motion. In the two-dimensional case, the tip gap was approximately 2% of chord, increasing with flapping angle to a maximum of 6% at a flap angle of 15°. The NACA0012 profile was mounted to a robotic pitching-flapping system (labelled I in Figure 3.4) through the roof opening in order to prescribe the motions described above. This pitching-flapping system was integrated into a rack-and-pinion traverse that provided a convective velocity of $U_\infty = 0.3m/s$.

A $527nm$ Photonics Industries $40mJ$-per pulse Nd:YLF laser was used to illuminate the flow-field at the mid-span of the NACA0012 profile during a pitching-flapping

cycle, after approximately 20-chords of steady-state travel. The flow was seeded with $100\mu m$ hollow glass micro-spheres, which were tracked using four-dimensional Particle Tracking Velocimetry (4D-PTV), a state-of-the-art Lagrangian measurement technique described by Schanz et al. (2016). The use of 4D-PTV allows the reconstruction of the entire velocity gradient tensor and therefore every component of the vorticity transport equation, thus enabling the direct testing of the hypothesis laid out in Section 3.2. The 4D-PTV system was comprised of four Photron SA-4 cameras operating at $1000Hz$ with a resolution of $1024 \times 1024\text{px}^2$, capturing particle tracks over a $130 \times 130 \times 10mm^3$ measurement volume, with the short-axis of the domain parallel to the profile span to capture the LEV cross-section. Utilizing two adjacent fields of view, just under one convective time of data was obtained, and measurements were repeated for ten individual runs per test case. At the mid-point of the measurement, each of the three cases had an identical angle-of-attack ($\alpha = 32°$). Raw pre-processed images were also used to verify the repeatability of the motion, which had a maximum variation of 5 pixels (0.2 % of chord) at the half-span location where measurements were conducted. These pre-processed images were also used to determine the geometric angle of attack and flapping velocity in order to estimate the error in the motion reproduction. The RMS error observed in geometric angle of attack across all cases and all runs was $\Delta\alpha = 0.2°$. Meanwhile, the deviation in the flapping velocity resulted in an RMS error in effective incidence of $\Delta\alpha_{\text{eff}} = 0.4°$. Processing of the 4D-PTV data was accomplished with LaVision Davis 8.3.0 software.

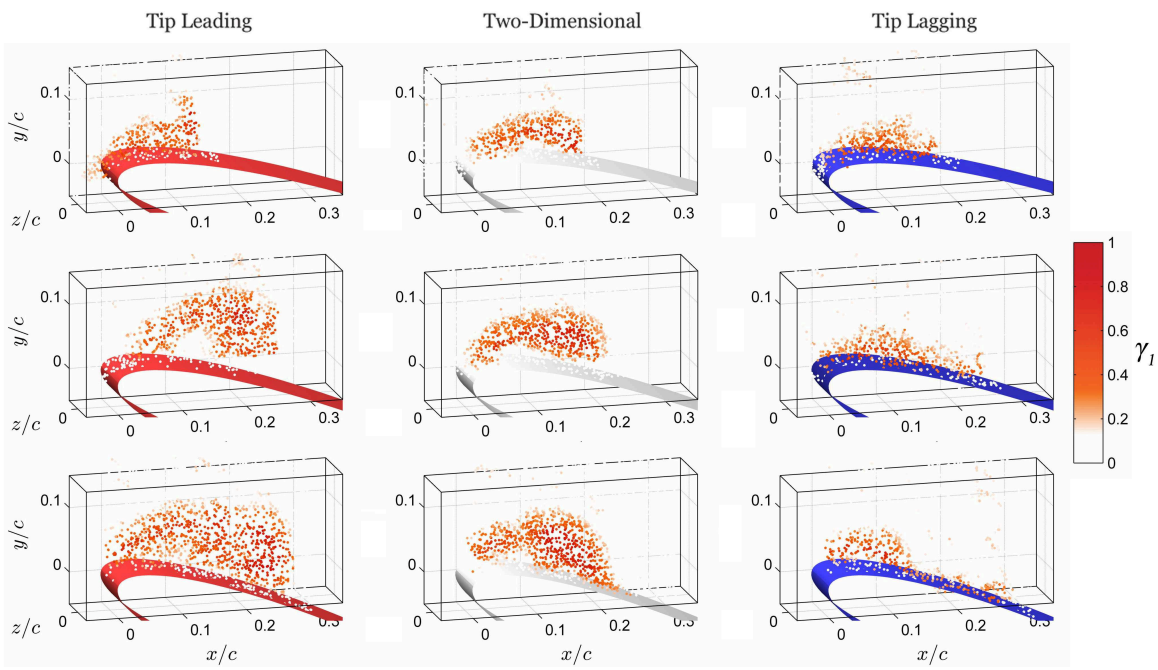

Figure 3.5: Three snapshots centred about $s/c = 1.5$ of highly-rotational tracked particles are highlighted here with the gamma criterion for the tip-leading case (red, left), two-dimensional reference case (grey, centre), and tip-lagging case (blue, right), respectively. All low-vorticity particles are removed for clarity. The tip-lagging case, similar to kinematics found in nature, exhibits a compact LEV closer to the profile surface than either of the other cases. As a faster-growing LEV is likely to reach the limiting $1c$ length-scale earlier, this indicates that it will not remain attached for as long into the motion.

3.4 Results

Figure 3.5 shows the evolution of the flow-field captured for an individual run of each of the three test-cases considered, with the final snapshot corresponding to the maximum geometric angle of attack. Tracked particles of high rotation have been coloured by gamma criterion to highlight the LEVs formed, as defined by Graftieaux et al. (2001), and low-rotation particles have been removed for clarity. At this point in the motion, streamwise position of the vortex does not vary significantly between

the three cases as the vortex detachment process has not yet started. However, at this point it can already be observed that the tip-lagging case (blue), which replicates the passive bending kinematics found in nature, has a much more compact and less coherent vortex structure, closer to the surface of the profile than the tip-leading case (red) or the two-dimensional case (grey). In turn, the LEV in the tip-leading case has a larger cross-sectional area than the two-dimensional case. These observations are already intuitively in agreement with the hypothesis laid out in Section 3.2 that the tip-leading case would exhibit a stronger, larger vortex while the tip-lagging case would have a weaker, more compact vortex. These hypothesis are further supported in the time-resolved, quantitative measurements. Circulation histories are shown in Figure 3.6, where the circulation value presented is the ensemble average of ten runs per case. Along with its smaller vortex size shown previously, the tip-lagging case (blue) has a smaller circulation, and a lower rate of circulation growth relative to the tip-leading (red) and two-dimensional (grey) cases. The tip-leading case has a larger circulation and a higher circulation growth rate than the two-dimensional case, but does not deviate as far from the two-dimensional case as that of the tip-lagging case.

Spanwise vorticity convection is shown in Figure 3.7(a), next to spanwise vortex stretching in Figure 3.7(b). Vorticity transport in the two-dimensional case will not be discussed here, as it is nearly zero for the entire measurement duration. However, values are nevertheless presented in Figure 3.7 as an indicator of the run-to-run variation present in the current experiments. For each of these two parameters, the spatial average was taken across the vortex area as defined by a gamma criterion of $\gamma_2 \geq 0.64$, and once again the ensemble average from ten runs is presented here. Based on Equation (3.1), the large negative vorticity convection seen in the tip-leading

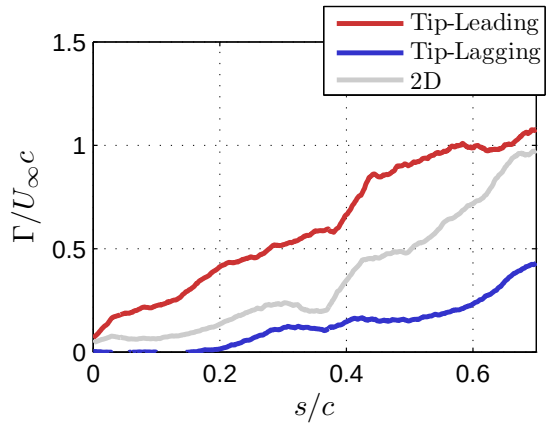

Figure 3.6: Vortex circulation is highest for the tip-leading case, and lowest for the tip-lagging case, similar to the results seen for the cross-sectional vortex area.

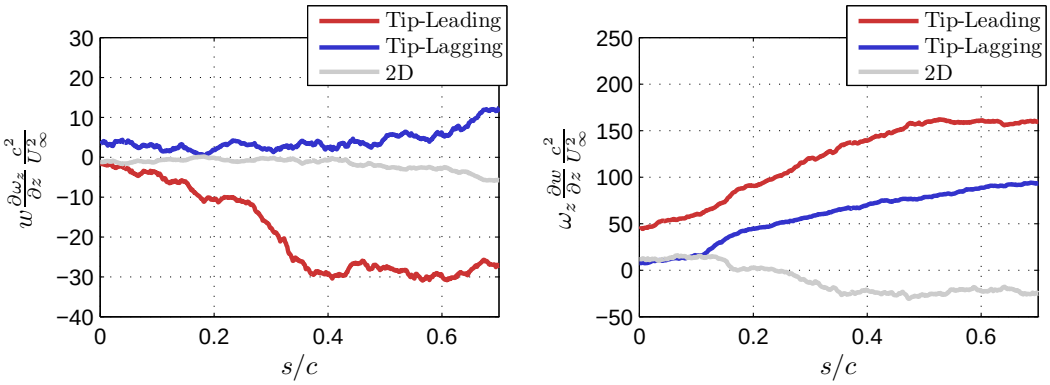

(a) Vorticity convection

(b) Vortex stretching

Figure 3.7: Vorticity convection is large and negative for tip-leading kinematics. Meanwhile, vortex stretching has the same sign for both tip-leading and tip-lagging kinematics. Therefore, as the flexible cases differ from the two-dimensional case in opposite ways, the two cases cannot be differentiated through vortex stretching.

case should serve to increase the circulation at this spanwise location, explaining its higher circulation relative to the two-dimensional case. Meanwhile, the tip-lagging case exhibits a positive vorticity convection, matching its correspondingly reduced circulation relative to the two-dimensional case. Vortex stretching meanwhile is non-negligible and positive in both cases. The spanwise flow set up due to rotation is similar in magnitude for both 'flexible' cases, however the tip-lagging case has a lower centre line vorticity. Nevertheless, it does not appear that vortex stretching can be used to differentiate the tip-leading and tip-lagging cases, as it is the same sign for both flexible cases.

3.5 Discussion

In Section 3.2 it was hypothesized that spanwise profile flexibility could be used to control LEV circulation, and thereby also LEV stability. For both flexible cases studied here, the spanwise flow produced by spanwise profile bending was able to convect circulation along the span and thus manipulate LEV circulation. This circulation control would allow the tip-leading case to increase instantaneous lift production, as needed for manoeuvres. However, this increase in circulation is likely to reduce LEV stability such that a manoeuvring animal would only be able to exploit this lift over a shorter period of time. This reduced vortex stability is directly related to the relative growth rate of the vortex; based on the topological detachment criteria laid out by Rival et al. (2014), a faster-growing LEV would detach earlier in its growth as it would quickly reach a limiting length-scale on the order of one chord-length. Moreover, Wong and Rival (2015) found that this specific mechanism of LEV detachment resulted in a correlation between spanwise vorticity convection and relative LEV

stability. This argumentation is of course in line with the observation of increased vortex size in the tip-leading case, and decreased vortex size in the tip-lagging case, respectively.

Due to the use of spanwise profile bending as a method of flow control, it is unlikely that an evolutionary convergence similar to that observed by Lucas et al. (2014) in cruising flight would also be observed in manoeuvring flight, as rapid force generation may be valued higher than efficiency. By analogy, in jet-like propulsion, Dabiri (2009) noted that squid maximized impulse instead of efficiency during escape manoeuvres since survival was prioritized above all else, and therefore the squid deviated from the more universal behaviour seen in cruise. Additionally, Cleaver et al. (2016) only observed large differences in force histories between rigid and flexible profiles for much larger Strouhal numbers than those investigated here. Indeed, Cleaver et al. (2016) observed much less profile deflection at the Strouhal numbers we investigate, implying the above results may only be achieved by an animal actively bending its wing. However, the current study nevertheless echoes the general conclusion of Lucas et al. (2014) that spanwise bending is not determined by wing material or physical structure, but rather by constraints on aerodynamic performance.

3.6 Conclusions

The first conclusion of this study is that spanwise profile bending can indeed be used to control LEV growth and stability. This conclusion comes from the observation that tip-lagging kinematics, like the passive bending found in the natural world, produced a more compact LEV with reduced circulation relative to the two-dimensional reference case. Meanwhile, tip-leading kinematics produced a much stronger LEV relative to

the two-dimensional case.

The second conclusion is that the differences in vortex strength could not be attributed to vortex stretching, as both the tip-leading and tip-lagging cases had positive vortex stretching, while the resulting circulation and vortex sizes differed from two-dimensional case each in an opposite sense. Rather, we conclude instead that flexibility modulates the circulation transport along the span of a profile following Equation (3.1). These conclusions together explain one role that spanwise profile bending plays in natural swimming and flying.

3.7 Acknowledgements

The authors gratefully acknowledge the support of the U.S. Air Force Office of Scientific Research under grant number FA9550-13-1-0117, monitored by Dr. Douglas Smith.

Chapter 4

Flow separation on flapping and rotating profiles with spanwise gradients

4.1 Abstract

The growth of leading-edge vortices (LEV) on analogous flapping and rotating profiles has been investigated experimentally. Three time-varying cases were considered: a two-dimensional reference case with a spanwise-uniform angle-of-attack variation α; a case with increasing α towards the profile tip (similar to flapping flyers); and a case with increasing α towards the profile root (similar to rotor blades experiencing an axial gust). It has been shown that the time-varying spanwise angle-of-attack gradient produces a vorticity gradient, which, in combination with spanwise flow, results in a redistribution of circulation along the profile. Specifically, when replicating the angle-of-attack gradient characteristic of a rotor experiencing an axial gust, the spanwise-vorticity gradient is aligned such that circulation increases within the measurement domain. This in turn increases the local LEV growth rate, which is suggestive of force augmentation on the blade. Reversing the relative alignment of the spanwise-vorticity gradient and spanwise flow, thereby replicating that arrangement found in a flapping

flyer, was found to reduce local circulation. From this, we can conclude that spanwise flow can be arranged to vary LEV growth to prolong lift augmentation and reduce the unsteadiness of cyclic loads.

4.2 Introduction

As a first-order approximation, a flapping wing will experience rapid time-dependent variations in angle-of-attack α as a function of position along the span. Often, the angle-of-attack and pitch rate are sufficient for flow to separate, resulting in the formation of a leading-edge vortex (LEV) (Lentink and Dickinson 2009b). Significant attention has been given to understanding the role of the LEV in lift generation and maneuvering of small animals (Ellington et al. 1996; Usherwood and Ellington 2002). In particular, understanding the roles of spanwise flow and spanwise angle-of-attack gradient on the maintenance of LEV position along the profile is thought to be critical in understanding low-Reynolds number flight (Beem et al. 2012; Wojcik and Buchholz 2014; Wong and Rival 2015). Large rotational accelerations, corresponding to low Rossby numbers Ro, have been found to be responsible for stabilizing the LEV by draining vorticity into a trailing vortex system (Lentink and Dickinson 2009a).

In contrast, most rotors are designed for steady operation, and would not experience flow separation unless impacted by a gust, which for this study will be assumed in the axial direction. Gusts are of course common in the atmosphere and therefore understanding their interaction with rotor systems is critical in many engineering applications such as in wind turbines (Wächter et al. 2011). Similar to flapping flyers, rotors will experience strong spanwise flow from rotational accelerations, particularly at inboard portions of the blade. This can be problematic, since the performance of

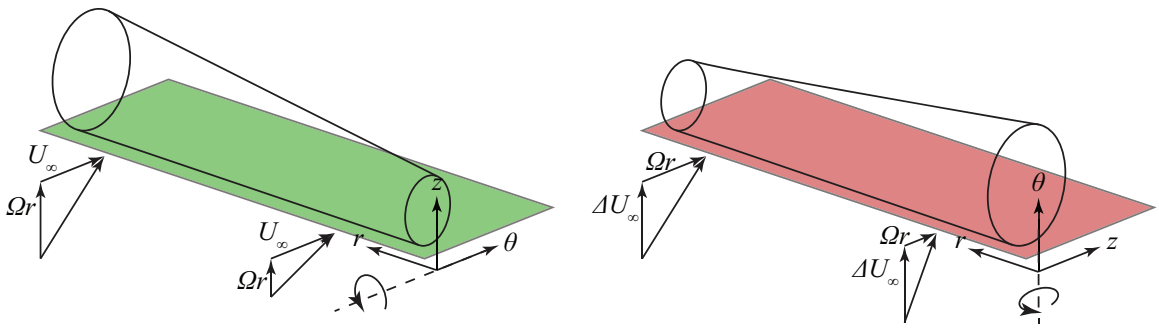

Figure 4.1: The angle of attack change is shown here for a flapping wing case (left) and a rotor case experiencing a gust (right). The angle of attack change on a flapping wing grows towards the tip of the profile, whereas the angle of attack change for a rotor with gust is greatest towards the root.

rotating wings and blades is typically calculated using blade-element models or strip theory (Glauert 1935; Videler 2005). These models often assume little to no interaction between the blade elements, such that each element is treated as an independent two-dimensional airfoil section (Burton et al. 2001). Indeed, in order to obtain accurate results in low-order models, the effect of spanwise flow on rotors is adjusted with an empirically-determined correction factor (Ronsten 1992; Du and Selig 1998). In reality, assuming a set of two-dimensional solutions along the spanwise direction is often insufficient to describe the flow (Bansmer and Radespiel 2012).

While the importance of this spanwise flow has been noted for the cases of both natural flight and rotor operation, the unsteadiness experienced by these two analogous cases is very different; the angle-of-attack gradient is inverted between the two, as shown in Figure 4.1. For instance, consider the angle-of-attack distribution on a flapping bird during the downstroke. The variation in angle of attack at an instant in time due to flapping, $\Delta\alpha$, is described by the following equation:

$$\Delta\alpha(r) = \arctan\left(\frac{\Omega r}{U_\infty}\right) - \alpha_0 \ , \tag{4.1}$$

where α_0 is the initial angle-of-attack, Ω is the rate of rotation, U_∞ is the forward speed of flight, and r is the spanwise coordinate. In this case, the change in angle-of-attack is negligible at the wing root and grows towards the wing tip. Contrast this with the instantaneous angle-of-attack distribution of a rotor blade experiencing an axial gust:

$$\Delta\alpha(r) = \arctan\left(\frac{U_\infty + \Delta U}{\Omega r}\right) - \alpha_0 \ , \tag{4.2}$$

where ΔU is the gust magnitude. The respective velocity triangles of each of these cases is shown in the left side of Figure 4.2. As the rotational component of velocity Ωr moves from numerator to denominator, the peak angle-of-attack change moves closer to the profile root, as illustrated on the right of Figure 4.2. If the kinematics of flapping wings are responsible for their resilience against gusts, then the question arises if rotor-like kinematics can produce the same benefits.

While these two examples may operate around different optimums, both must be resilient against unsteadiness in their respective environments. Thus, there is an opportunity to transfer insight between these communities. Many previous studies have already focused on determining how two-dimensional parameters can affect LEV development and stability (Baik et al. 2012; Wong and Rival 2015; Widmann and Tropea 2015). Therefore, in the current study we will consider the relationship between opposing gradients in angle-of-attack in the presence of spanwise flow, as was exemplified by the above examples, on LEV development and relative stability. The following section will formulate the mechanics of LEV growth rigorously in order to develop an expectation for the role of this spanwise angle-of-attack gradient.

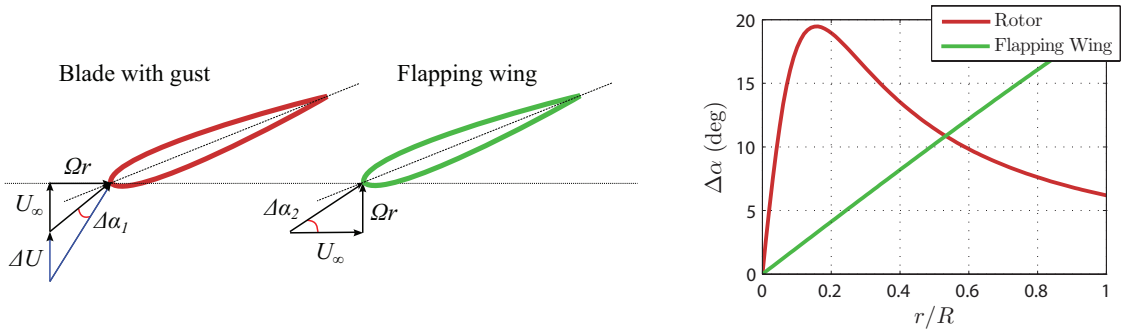

Figure 4.2: The angle-of-attack (α) change is shown for both the rotor case and the flapping case (left). A change in the axial velocity (gust) ΔU has an opposite effect on the angle-of-attack distribution for a rotor compared to the distribution formed from a flapping motion. An example of the spanwise distribution of angle-of-attack is shown for the rotor and flapping cases in red and green, respectively (right).

4.3 Background

In this study, we are primarily interested in the formation of the LEV in unsteady environments for flapping and rotating profiles. Due to the spanwise angle-of-attack gradients outlined above, LEV evolution is a function of the spanwise position (and gradient) along the profile. Spanwise locations whose effective angle-of-attack changes greatly experience LEV formation earlier (Shipley et al. 1995). During LEV formation, higher effective angles of attack correspond to higher rates of circulation generation, which in turn correspond to higher rates of circulation growth within the vortex, as evidenced by the higher circulation and lift generation of airfoils in deep-dynamic stall as opposed to shallow-dynamic stall (Ol et al. 2009; Baik and Bernal 2012). As a result, the LEV would be expected to reach a topological limit in strength (and size) earliest at positions with the highest angle-of-attack change, for two-dimensional cases where the vortex strength is not limited by spanwise flow.

This topological limit in LEV size has been identified to have a length scale on

the order of the chord, indicating the onset of vortex detachment (Rival et al. 2014). However, a persistent dynamic stall vortex is often generated on rotating and flapping profiles that lasts for much larger time-scales when compared to their respective two-dimensional case (Lentink and Dickinson 2009b; Ellington et al. 1996; Birch and Dickinson 2001; Bomphrey et al. 2005; Harbig et al. 2013). It has been proposed that rotational accelerations act to stabilize the vortex, with three critical rotational accelerations affecting vortex attachment (Lentink and Dickinson 2009a): the angular acceleration (a_{ang}), centripetal acceleration (a_{cen}), and Coriolis acceleration (a_{Cor}):

$$a_{\text{ang}} = \hat{\dot{\Omega}} \times \hat{r}, \tag{4.3}$$

$$a_{\text{cen}} = \hat{\Omega} \times (\hat{\Omega} \times \hat{r}), \tag{4.4}$$

$$a_{\text{Cor}} = 2\hat{\Omega} \times \hat{u_{\text{eff}}}, \tag{4.5}$$

where u_{eff} is the local velocity in the rotating frame. Note that in steady rotation cases the angular acceleration, $\dot{\Omega}$, goes to zero. The centripetal acceleration a_{cen} induces a pressure gradient that drives spanwise flow. The local velocity u_{eff} is the sum of both the free-stream velocity and that velocity induced by the flapping motion of the wing. In steady rotor operation or for flapping wings, the free-stream velocity is parallel to the axis of rotation, and therefore does not contribute to the Coriolis acceleration, which becomes exclusively a function of the flow induced by the blade rotation:

$$a_{\text{Cor}} = 2\Omega \times u_{\text{eff}} = 2\Omega \times (\Omega \times r). \tag{4.6}$$

In a linear momentum balance described by the Navier-Stokes equation, the Coriolis effect acts to stabilize the dynamic stall vortex (Lentink et al. 2009). Moreover, even if the vortex is stabilized by other means, it has been found that the Coriolis effect acts to increase force generation(Jardin and David 2014). Rotational effects are still significant in the current study, but utilizes an angular momentum balance, described by the vorticity transport equation, to examine vortex stabilization without directly invoking the concept of Coriolis forcing. Within this framework, the Coriolis effect is manifested as an induced spanwise flow (Maxworthy 2007). Spanwise flow on the order of the flapping velocity can be expected, as this has been observed for dynamic-stall vortices such as in a flapping motion (Ellington et al. 1996). This spanwise flow contributes to the redistribution of vorticity along the span of the profile following the vorticity transport equation:

$$\frac{d\omega}{dt} + (\vec{u} \cdot \nabla)\omega = (\omega \cdot \nabla)\vec{u} + \nu\nabla^2\vec{\omega}, \tag{4.7}$$

where the terms on the left-hand side describe the change in vorticity of the fluid due to unsteadiness and convection. The terms on the right-hand side represent vortex stretching and tilting, and the viscous diffusion of vorticity, respectively. For a gust event acting on a rotating blade, viscous diffusion can be neglected under the assumption that the timescales of diffusion are much larger than the timescales of vortex growth itself. Therefore, the spanwise component of the vorticity transport equation in the rotating frame takes the form:

$$\frac{\partial\omega_r}{\partial t} + u_r\frac{\partial\omega_r}{\partial r} + \frac{u_\theta}{r}\frac{\partial\omega_r}{\partial\theta} + u_z\frac{\partial\omega_r}{\partial z} = \omega_r\frac{\partial u_r}{\partial r} + \frac{\omega_\theta}{r}\frac{\partial u_r}{\partial\theta} + \omega_z\frac{\partial u_r}{\partial z} + 2\Omega\frac{\partial u_r}{\partial z}, \tag{4.8}$$

where the terms from left to right are the constituent terms of Equation 4.7 above representing the rate of change of vorticity due to unsteadiness, the convection of vorticity in the $r-$, $\theta-$, and $z-$ directions, vortex stretching and vortex tilting, and Coriolis effects, respectively. A schematic of the hypothesized vorticity balance is shown in Figure 4.3 for the rotor case, where circulation generated in the shear layer is balanced by spanwise-vorticity convection. It can be assumed that the vortex is aligned approximately parallel with the span of the blade, and that therefore ω_r is the dominant component of vorticity present in the flow (Wong and Rival 2015). The rate of spanwise circulation redistribution can be computed by integrating the vorticity-transport equation across the vortex-core area (Wojcik and Buchholz 2014; Wong and Rival 2015):

$$\frac{\partial \Gamma}{\partial t} = -\int u_r \frac{\partial \omega_r}{\partial r} dA, \tag{4.9}$$

where the vortex tilting term vanishes as the vortex is aligned along the span of the profile as shown in Figure 4.3, which is a reasonable approximation far from the profile tip, before the LEV begins to tilt into the tip vortex. The stretching term vanishes, as stretching acts to increase centre line vorticity but does not transport vorticity along the blade span. Additionally, for a vortex tube attached near the leading edge of the blade profile, gradients in the spanwise direction will be much larger than the gradients in the streamwise direction, resulting in the Coriolis term having a negligible impact on spanwise-vorticity transport. Note that the vorticity convection shown in Equation 4.9 only describes the redistribution of circulation generated at the leading edge, as opposed to the production of that circulation itself.

As shown in Equations 4.1 and 4.2, in transient flow conditions rotating profiles

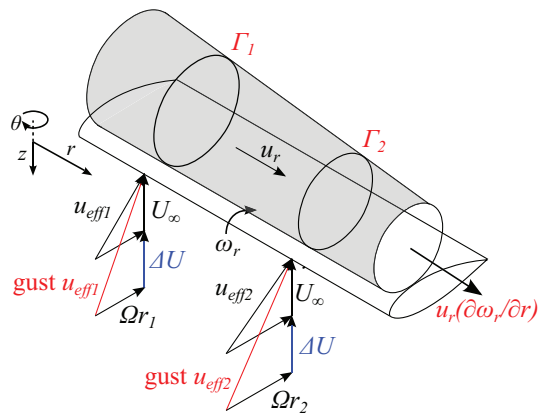

Figure 4.3: A section of a rotating profile experiencing a spanwise variation in angle-of-attack in the presence of radial flow, resulting in vorticity convection ($u_r \partial\omega_r/\partial r$) towards the profile tip.

develop a gradient in angle-of-attack along the blade span, from which a spanwise-vorticity gradient is formed. It is postulated that, in combination with the spanwise flow induced by rotational accelerations, this spanwise-vorticity gradient acts to re-distribute circulation along the span of the profile. However, as the gradient in angle-of-attack is opposite in sign for the flapping wings versus rotors in gusts, it is expected that the flapping case exhibits a reduction in circulation while the rotor case will exhibit an increase in circulation. The following section outlines the methods used to test the hypothesis experimentally.

4.4 Methods

In order to test the hypothesis at conditions relevant to large wind turbines, the angle-of-attack magnitude and spanwise gradient in angle-of-attack was determined for a reference 5MW NREL turbine operating at a free-stream velocity of $U_\infty = 11$m/s experiencing a gust of $\Delta U = U_\infty$ at a reduced frequency of $k = \pi f c/U_\infty = 0.35$.

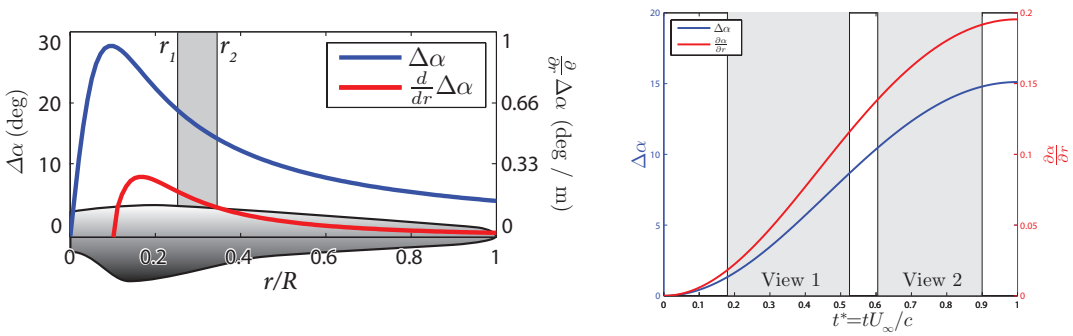

Figure 4.4: In order to test the hypothesis for conditions relevant to large wind turbines, change of angle of attack $\Delta\alpha$ and angle of attack gradient $\frac{\partial}{\partial r}\Delta\alpha$ were chosen based on an axial gust impinging on the NREL 5MW turbine. Specifically, the parametric values selected were equivalent to those at the $r/R = 0.3$ spanwise position, where large gradients are observed. The spanwise variation in $\Delta\alpha$ and angle of attack gradient $\frac{\partial}{\partial r}\Delta\alpha$ are shown on the left for a gust of $\Delta U = U_\infty$, and is shown on the right resolved in time.

This gust magnitude and frequency was chosen to be an extreme gust event, which is beyond what could be accommodated by pitch control. Moreover, this free-stream velocity and reduced frequency also fall well within the range of flying birds. For instance, the wingbeat frequency of pigeons has been observed to vary between approximately $0.1 \leq k \leq 0.35$ across a range of flight speeds $6m/s \leq U_\infty \leq 20m/s$ (Tobalske and Dial 1996). The change in angle-of-attack was determined for a sinusoidal variation in free-stream velocity at the 30% span position, as illustrated on the left-hand side of Figure 4.4. As a result, three test cases were developed. The first test case, hereafter referred to as the turbine case, was designed to exactly mimic the temporal angle-of-attack change, change in the spanwise gradient of angle-of-attack, and spanwise-flow direction experienced at the 30% span of the reference 5MW turbine. This case was developed in order to quantify the effect of spanwise redistribution of circulation on a representative rotating blade experiencing a gust.

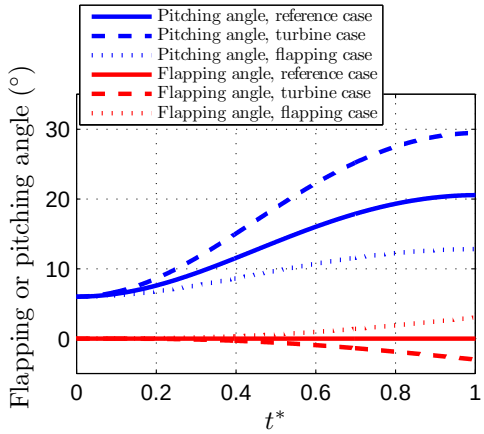

Figure 4.5: The pitching program for the two-dimensional reference case follows the angle-of-attack program exactly, and has a flapping angle of exactly zero. Meanwhile, the turbine and flapping cases each have an equal and opposite flapping angle in order to produce the appropriate spanwise gradients. In turn, their pitching programs are adjusted in order to maintain angle-of-attack programs identical to the reference case.

The second test case, hereafter referred to as the flapping case, was designed such that the temporal angle-of-attack change, and thus the change in the spanwise gradient of angle-of-attack, was equal in magnitude but opposite in orientation relative to the turbine case. The spanwise-flow direction is identical in each case. Thus, in the flapping case the angle of attack grows towards the tip, and spanwise flow is directed towards the tip, as is the case in flapping flight. The flapping case was developed in order to contrast the turbine case, and is used to discuss the global behaviour of the spanwise circulation profile. The third test case, hereafter referred to as the reference case, was set up to be a quasi two-dimensional pure-pitching case with no spanwise gradient in angle-of-attack, while having a magnitude change in angle-of-attack equal to the other test cases. The angle-of-attack program for the turbine case is shown in Figure 4.6, and the physical pitching and flapping programs for all three cases are shown in Figure 4.5.

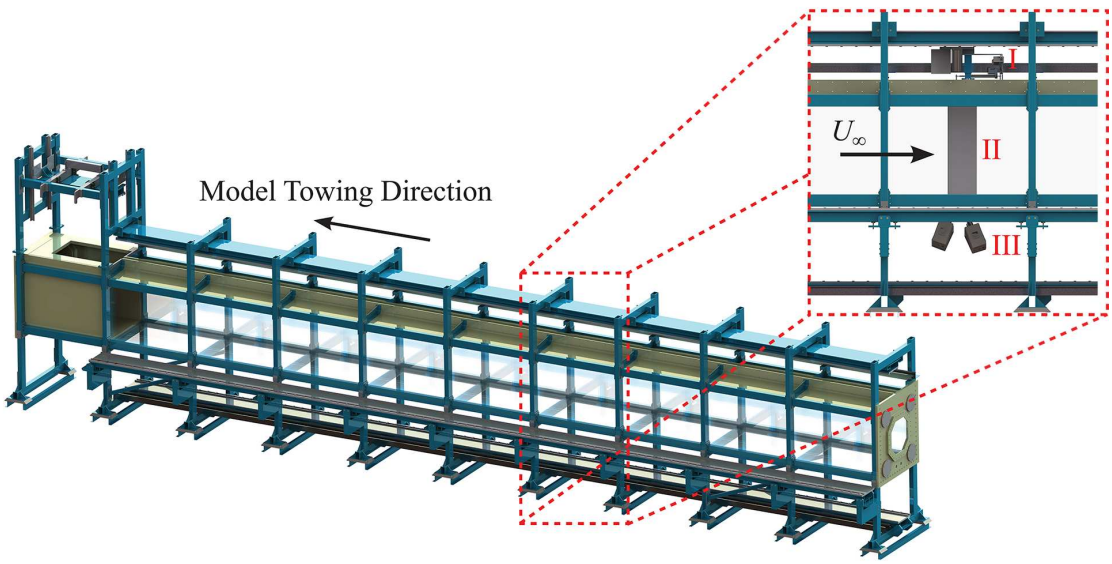

Figure 4.6: All test cases were conducted in a 15m-long towing tank with a 1m × 1m cross section with a semi-enclosed ceiling to minimize free-surface effects. The model (II) was actuated using a robotic pitching-flapping mechanism (I), which was towed from right to left along the upper traverse. A four-camera setup (III) was used to capture the motion of the seeding particles.

All tests were conducted in a 15m-long optical towing tank with a 1m × 1m cross section, shown in Figure 4.6. The tunnel ceiling was semi-enclosed, with only a 5cm opening to pass through the test article, in order to minimize free-surface effects. The tank is 15m long and uses water as the working fluid. The side and bottom walls of the tank are glass to allow for optical access. A traverse system, running the length of the towing tank, on which a 30cm chord, 1m span NACA-0012 test article was mounted, is fixed above the tank and was operated at a free-stream velocity of $U_\infty = 0.33m/s$, resulting in a Reynolds number of $Re_c = 10^5$. A z-type turbulator was placed at the 20% chord in order to ensure that all three cases experienced an identical turbulent boundary layer at the onset of motion. This onset of the pitching and flapping

actuation occurred after approximately 20 chords of steady-state motion at the free-stream velocity a constant angle-of-attack of 6° with zero flapping motion. Enforcing an identical initial condition, neglecting the initial rotation of the turbine case, was chosen in order to maximize possible comparison between the two cases. A pitch and flap actuator mechanism was mounted to this traverse system in order to control the blade motion, as shown in Figure 4.7. The mechanism consisted of two linear actuators, which controlled the pitching and flapping axes independently, attached to moment arms rotating around z and θ axes. In this way, the superposition of pitching and flapping motions could be used to dictate an angle-of-attack and a gradient in angle-of-attack independently. The actuator system was designed to accept a timeseries of blade pitch and flap angles, within the maximum actuator velocity and displacement range. As the blade underwent its programmed motion, the flow field around the profile was captured at the half-span location using a four-dimensional

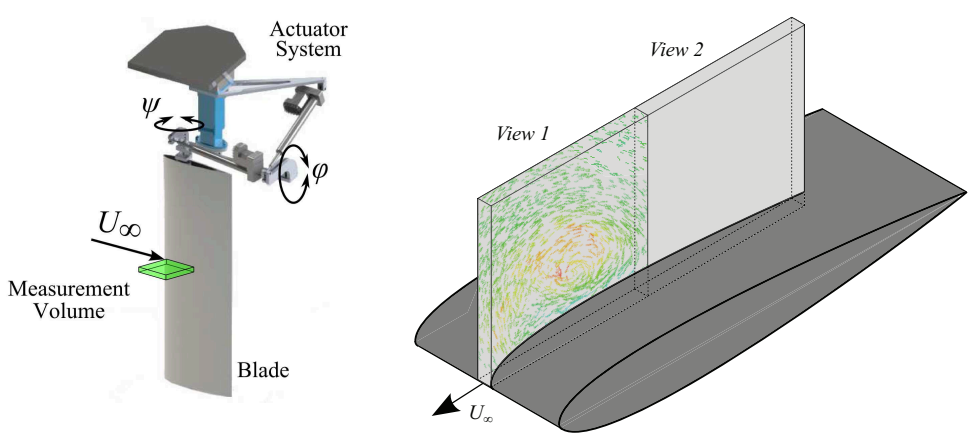

Figure 4.7: The profile is mounted to a mechanism capable of actuating the profile in both flapping and pitching (left). The blade motion intersects two adjacent measurement fields of view taken over separate runs, located at the half-span position. An exemplary volumetric vector field is shown, with the profile indicated for scale (right).

Particle Tracking Velocimetry (4D-PTV) system in order to capture all components of the velocity-gradient tensor, which are necessary to compute the individual terms of the vorticity transport equation (Schanz et al. 2016). Spatial velocity gradients were computed from the scattered velocity data by tri-linear interpolation.

The system consisted of four Photron SA-4 cameras ($1024\times1024\text{px}^2$ resolution) operating at $1000Hz$ to capture particle images illuminated with a Photonics Industries DM-40 laser. This illuminated volume was held in-place as the profile conducted its motion, and therefore the two adjacent measurement volumes illustrated in Figure 4.7 were used to maximize the measurement duration, as opposed to maximizing the field of view. For the turbine and flapping cases, an initial static flapping angle was applied to the profile such that the measurement volume was approximately orthogonal to the wing surface for each measurement. The quality of the volumetric reconstruction produced by 4D-PTV has been evaluated previously using synthetic images with artificial noise. 4D-PTV has been shown to triangulate detected particles with approximately half the error of tomographic PIV, with mean errors of 0.1 pixels being typical for such synthetic data sets(Schanz et al. 2016). Raw pre-processed images were also used to verify the repeatability and accuracy of the motion, which had a maximum variation of 5 pixels (0.2% of chord) from the motion program, at the half-span location where measurements were conducted.

4.5 Results

The resulting flow fields in the turbine and flapping cases are shown for a snapshot of time ($t^* = 0.8$) from a single run in Figure 4.8. Highly rotational regions have been isolated using the γ_2 criterion, which defines a vortex core as a location where

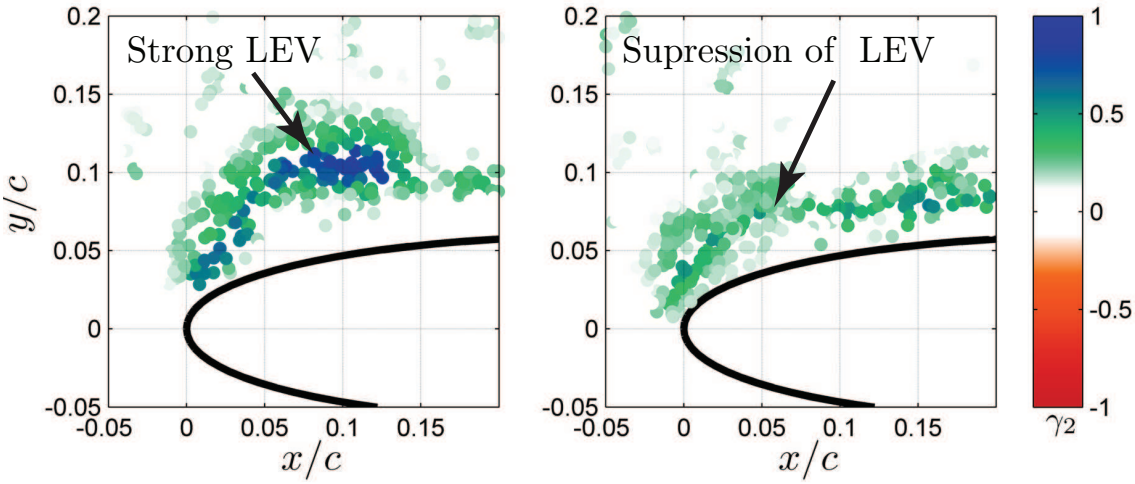

Figure 4.8: Regions of high rotation are visualized here for the turbine case (left) and the flapping case (right), with the γ_2-criterion for $t^* = 0.8$. This time step is near the end of the measurement period representing the highest observed angle of attack $\alpha \approx 18°$, and thus the largest extent of vortex growth in either test case. The vortex core, defined as $|\gamma_2| > 2/\pi$, is clear for the turbine case, whereas the flapping case exhibits an extended shear layer with no clear roll-up.

$|\gamma_2| > 2/\pi$ (Graftieaux et al. 2001). Here, we see a large LEV forming in the turbine case (left) with a clear vortex core. Meanwhile, the flapping case (right) exhibits an elongated shear layer without any γ_2 values reaching the threshold for core detection. In the remainder of this section, this qualitative difference will be explained in terms of spanwise flow and vorticity transport.

The spanwise flow u_r observed in the turbine case increases for the entire measurement period, as shown in Figure 4.9. This single value is determined by taking the spatial-average across a $0.2c \times 0.2c$ region above and directly behind the leading-edge of the profile, corresponding approximately to the maximum extent of the LEV in the turbine case. The use of a single spatial domain for averaging each case means that the relative magnitude of spanwise flow between cases is not affected by small

changes in the domain size, and in fact is proportional to the relative volumetric flow rate between each case along the span. The effective velocity $U_{\text{eff}} = \sqrt{U_\infty^2 + \Omega^2 r^2}$ was chosen as the normalization velocity in order to account for the additional flapping velocity. Spanwise flow was normalized by the instantaneous effective velocity in order to account for the rotational contribution to the effective velocity experienced in the turbine case. The spanwise velocity increased throughout the measurement period as a result of the rotational velocity increasing during the motion. This spanwise flow was on the order of the local rotational velocity Ωr at the measured spanwise position, which is consistent with results found in the literature (Wächter et al. 2011; Maxworthy 2007). The spanwise flow is in the direction of decreasing angle-of-attack for the turbine case, which mirrors that of a wind turbine experiencing a gust event. In comparison, the reference case exhibited negligible spanwise flow, indicating a nearly two-dimensional flow.

Similar to the turbine case, the flapping case exhibited increasing spanwise flow u_r within the dynamic stall vortex over the the entire measurement period. The spanwise flow was in the same direction as the turbine case, moving towards the tip, due to the pressure gradient induced by rotational accelerations. The spanwise velocity for both the flapping and turbine cases were within one standard deviation of one another. Rather, spanwise flow appears to be coupled to the rotational velocity Ω of the profile instead.

The spanwise-vorticity gradient within the dynamic stall vortex is shown in Figure 4.9. For the turbine case, the gradient is negative (decreasing towards the tip), and becomes increasingly negative as a function of the convective time. This negative vorticity gradient is likely due to the negative angle-of-attack gradient along the span

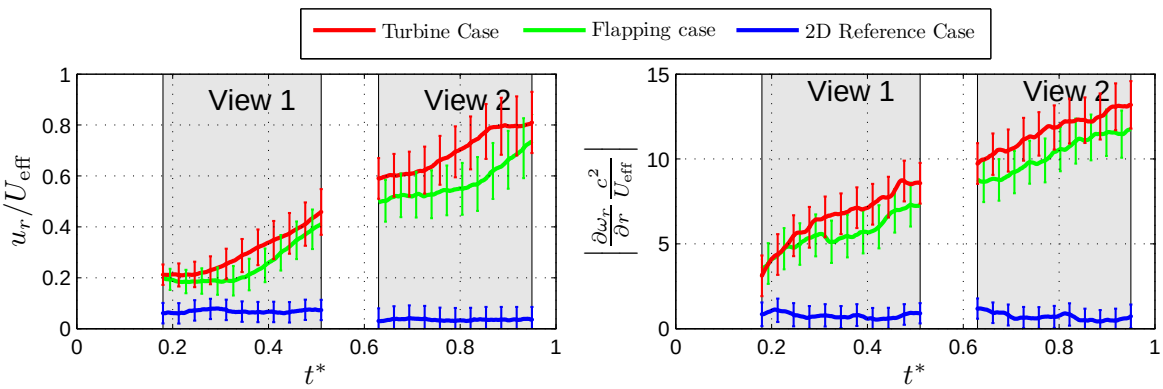

Figure 4.9: Both the spatially-averaged spanwise flow and vorticity gradient within the dynamic stall vortex was found to be similar between the turbine and flapping cases. Please note that the magnitude of the vorticity gradient is plotted here for comparison purposes, and that the vorticity gradient is negative in the turbine case. In both rotational cases the spanwise flow and vorticity gradient both increase as a function of convective time. For spanwise flow this was on the order of the rotational velocity (Ωr), in close agreement with literature (Maxworthy 2007). The reference case exhibited negligible spanwise flow and vorticity gradient. The run-to-run variation was estimated by the standard deviation of the 10 runs, and is plotted every 20 frames.

of the blade. Similar to the spanwise flow, the spanwise-vorticity gradient in the two-dimensional case has a small positive bias over the measurement period.

Due to the opposite sign of angle-of-attack gradient between the turbine and flapping cases, the spanwise-vorticity gradient was also opposite in sign, being positive for the flapping case (increasing towards the tip). The magnitude of the spanwise-vorticity gradient fell within one standard deviation between the two rotational cases. For both cases the spanwise gradient in vorticity and angle-of-attack were the same sign.

Finally, the circulation integrated across the entire measurement domain in the turbine case was greater than that observed for the reference case over the entire

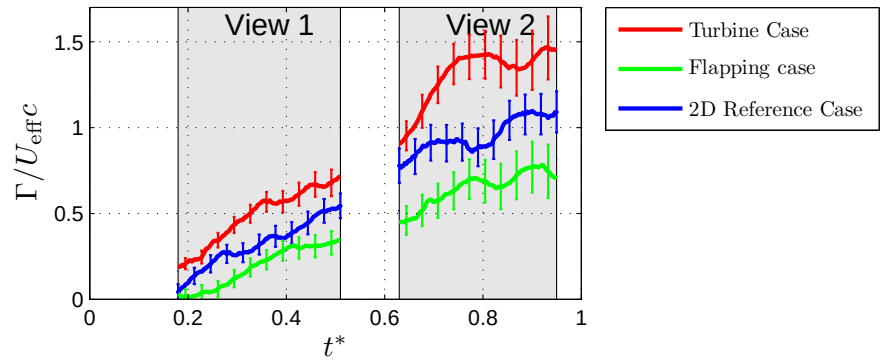

Figure 4.10: The growth rate of circulation in the turbine case was found to be greater than that of the reference case. In contrast, the growth rate of circulation in the flapping case was lower than that of the reference case. The difference in circulation growth is a result of the relative alignment of spanwise flow and the spanwise-vorticity gradient between the cases. The error bars denote the standard deviation of the 10 runs plotted every 20 frames.

measurement period, as shown in Figure 4.10. This indicates that vorticity transport due to the combination of spanwise flow and a spanwise-vorticity gradient acts to increase circulation for a rotating blade motion with a gust. The relative orientation of the spanwise flow and spanwise-vorticity gradient dictates the direction of this transport. The higher levels of circulation growth indicate that locally, the dynamic-stall vortex is less stable in the turbine case, and will reach the critical size sooner than the reference case (Rival et al. 2014).

In contrast to the turbine case, the observed circulation of the flapping case was lower than the two-dimensional reference case over the entire measurement period. The decrease in circulation is a function of the relative alignment between the spanwise flow and spanwise-vorticity gradient generated on the profile. The vorticity gradient in the flapping case was parallel with the spanwise flow, which, based on Equation

(4.9), resulted in circulation being transported from areas of low generation to areas of high generation.

Based on these above results from the turbine and flapping cases, it can be observed that rotors exposed to axial gusts, with increasing angle of attack towards the root, experience increased circulation. This is in contrast to cases with increasing angle of attack towards the tip, as in the flapping case, which experiences a decrease in circulation.

4.6 Conclusions

In this study, the effect of a spanwise angle-of-attack gradient on the growth and stability of the dynamic stall vortex for rotating systems has been investigated. Three cases were considered:

1. The turbine case was actuated such that the angle-of-attack magnitude and spanwise angle-of-attack gradient generated on the test model was equivalent to that found at the 30% span of a wind-turbine blade experiencing an axial gust event;

2. The flapping case was actuated such that the spanwise angle-of-attack gradient was equal in magnitude, and opposite in direction, relative to the spanwise flow of the turbine case;

3. The two-dimensional reference case was actuated in pure pitch such that it had an identical angle-of-attack history to the rotational cases over the observed convective time but with no spanwise gradients or spanwise flow.

Two major conclusions have been drawn. First, that inducing an angle-of-attack gradient along the span of a profile results in a corresponding spanwise-vorticity gradient. Second, that spanwise flow induced from rotational accelerations coupled with the spanwise-vorticity gradient results in a redistribution of circulation along the span of the profile, which in turn has an impact on the growth of the LEV.

In the turbine case, the spanwise-vorticity gradient is anti-parallel to the spanwise flow, resulting in transport of vorticity into the measurement domain, thereby increasing the circulation observed. Based on the vortex stability criteria found in the literature, the increase in vortex-growth rate corresponds to a less stable vortex (Rival et al. 2014). Conversely, the flapping case showed transport of vorticity from out of the measurement domain, reducing circulation. This effect decreased circulation, indicating increased stability. The decreased vortex stability and increased vortex circulation in the turbine case describes a situation where transient loads increase in frequency and magnitude. Therefore, highly transient loads can be mitigated through modifications in either spanwise flow or spanwise-vorticity gradient, such as through wing fences or blade twist, respectively, in order to maintain consistent power generation or thrust production, or even reduce cyclic loading.

Under rotation, spanwise flow is induced within the dynamic stall vortex due the spanwise pressure gradient generated from rotational accelerations. The redistribution of circulation through vorticity transport was driven by a combination of this spanwise flow and the spanwise-vorticity gradient described above. The behaviour of this circulation transport is described by the spanwise convection term $u_r \frac{\partial \omega_r}{\partial r}$ of the vorticity transport equation.

Finally, the Coriolis term of the vorticity transport equation does not affect the transport of angular momentum directly. Rather, the Coriolis effect is manifested by inducing a spanwise flow (Lentink et al. 2009). Therefore, we present an equivalent description of this phenomenon as found in the literature, where the circulation-transporting effect of spanwise flow is described through the convection of angular momentum.

4.7 Acknowledgements

The authors would like to thank the Ontario Student Assistance Program and the Natural Sciences and Engineering Research Council of Canada for partial funding in support of this work.

Chapter 5

Coupling Temporal and Spatial Gradient Information in High-Density Unstructured Lagrangian Measurements

5.1 Abstract

Particle tracking velocimetry (PTV) produces high-quality temporal information that is often neglected when computing spatial gradients. A method is presented here to utilize this temporal information in order to improve the estimation of spatial gradients for spatially unstructured Lagrangian data sets. Starting with an initial guess, this method penalizes any gradient estimate where the substantial derivative of vorticity along a pathline is not equal to the local vortex stretching/tilting. Furthermore, given an initial guess, this method can proceed on an individual pathline without any further reference to neighbouring pathlines. The equivalence of the substantial derivative and vortex stretching/tilting is based on the vorticity transport equation, where viscous diffusion is neglected. By minimizing the residual of the vorticity-transport

equation, the proposed method is first tested to reduce error and noise on a synthetic Taylor-Green vortex field dissipating in time. Furthermore, when the proposed method is applied to high-density experimental data collected with *'Shake-the-Box'* PTV, the spatial coherence of the resulting vorticity field is improved. In the particular test case investigated here of an accelerating circular plate captured during a single run, the method acts to delineate the shear layer and vortex core, as well as resolve the Kelvin-Helmholtz instabilities, which were previously unidentifiable. The proposed method shows promise for improving PTV measurements that require robust spatial gradients while retaining the unstructured Lagrangian perspective.

5.2 Introduction

The development of aerodynamic or hydrodynamic systems requires a detailed understanding of the relationship between structural features on immersed bodies, such as profile shape or flexibility, and the resulting vortical flow field. Often these design features are used to manipulate highly-separated three-dimensional vortical flows, such as the unsteady vortex rings investigated by Shadden et al. (2006), similar to those found in jellyfish propulsion. In particular, it was found that Lagrangian analysis was much more effective at capturing the flow topology, especially at greater degrees of unsteadiness. Fully characterizing such flows not only requires determining velocity gradients familiar to Eulerian analysis, but also the transport of vorticity-containing mass over time, as shown in Figure 5.1. Particle-tracking velocimetry (PTV) techniques, especially modern high-density methods such as *Shake-the-Box* (STB, a.k.a. 4D-PTV) described by Schanz et al. (2016), are ideally suited to capturing both the

required velocity field, as well as the desired Lagrangian flow history. Several techniques exist to determine the velocity gradient, vorticity or pressure at a very high resolution from dense velocimetry data. These methods include *FlowFit* (see Gesemann et al. (2016)) or *VIC+* (see Schneiders and Scarano (2016)). In both *VIC+* and *FlowFit*, physical constraints on the system are used to improve the accuracy of velocity interpolation, such as through penalizing non-zero divergence in *FlowFit*. *VIC+* in particular makes use of the vorticity transport equation as a physical constraint, and utilizes the high-quality substantial derivative available from PTV. This follows previous developments for particle image velocimetry (PIV) where physical constraints were able to leverage high spatial resolution to improve temporal resolution. This work is exemplified by Scarano and Moore (2012), where the spatial resolution of tomographic-PIV was used to estimate advection between velocity snapshots to super-sample data beyond the traditional Nyquist criterion. Alternatively, Jeon et al. (2014) demonstrated the use of high temporal resolution in time-resolved PIV to improve spatial resolution.

The aerodynamic and hydrodynamic forces of highly-separated vortical flows are often analyzed with respect to the topology of the flow, for instance with Lagrangian coherent structures as demonstrated in Rockwood et al. (2016). PTV inherently provides this Lagrangian perspective on the development of the flow, as was illustrated above in Figure 5.1. For instance, fluid that passes over a vorticity source like the leading-edge shear layer in Figure 5.1 can be tracked forward along a pathline to study the evolution of that mass, in this case into a vortex. Meanwhile, the mass in this vortex can be tracked backwards in time to identify the source of this vorticity. Additionally, the high-quality substantial derivative determined from PTV

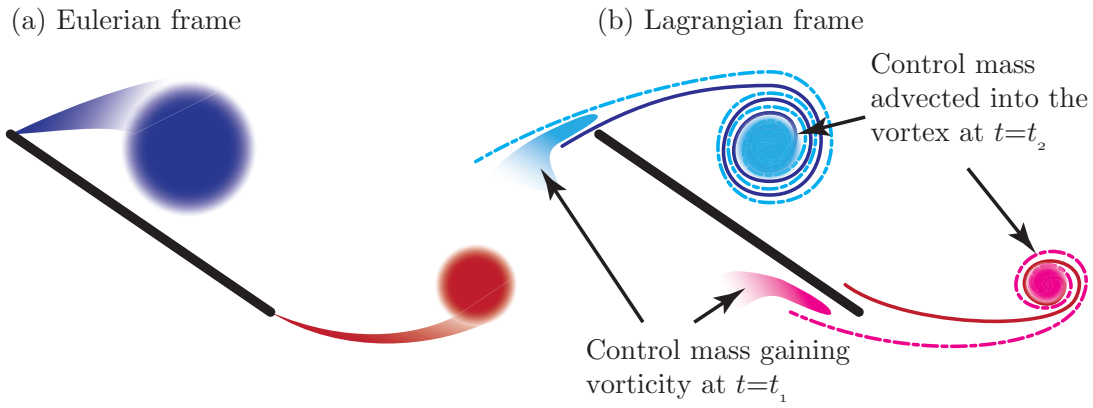

Figure 5.1: (a) A vortex-pair forming on a flat plate is illustrated in the familiar Eulerian frame. (b) The same vortex-pair can be studied in a Lagrangian frame: at $t = t_1$ two control masses gain vorticity through the leading and trailing-edge shear layers, respectively, and are tracked forward in time into the vortex core at $t = t_2$. In this way the Lagrangian data can be used to determine the origin of vorticity-containing mass (by tracking structures backwards in time), or to study the evolution of mass gaining vorticity through time (by tracking mass through a shear layer).

dramatically improves the quality of pressure fields derived from the velocity field, as described by Neeteson and Rival (2015) and Neeteson et al. (2016). Wolf et al. (2013) also noted that conducting a Lagrangian-frame analysis alongside familiar Eulerian techniques yielded unique insight into vortex entrainment. However, most available high-resolution techniques for determining spatial gradients do so on the familiar Eulerian grid, while averaging techniques for Lagrangian data smooth away small-scale flow structures. Therefore, with the motivation of maintaining the intrinsic transport information of a pathline, the current study proposes a high-resolution method for determining derived properties natively on unstructured Lagrangian data, without resorting to averaging multiple runs.

In order to evaluate the robustness of the proposed methodology, it is applied

to two test cases: First, a synthetic data set, for which true values of the velocity gradient tensor are known *a priori*, is used to verify that the method reduces gradient estimation error in the process of reducing noise. Second, an experimental *4D-PTV* data set is used to evaluate the increase in fidelity and reduction in noise when the method is applied to real experimental data. The details of the vorticity-correction technique are presented next.

5.3 Gradient Optimization Methodology

By directly tracking individual particles, PTV does not experience the loss of fidelity that occurs when taking the average displacement across an interrogation window, as described by Kähler et al. (2012). Furthermore, by collecting data along a pathline, high-quality temporal information is obtained, especially in the form of substantial derivatives. However, if one wishes to maintain the unstructured Lagrangian description of the flow, there are limited methods for computing spatial gradients. Among them there are regression-based methods that, for example, minimize the residual of an overdetermined set of directional derivatives, as discussed by Meyer et al. (2001). Alternatively, there are weighted-averaging techniques that calculate the gradient as a weighted-sum of local derivatives, as discussed by Correa et al. (2011).

In either of the above methods, individual outliers or poor spatial resolution can have a substantial effect on the value of gradients computed at any given point. The effect of individual outliers is mitigated from the Lagrangian nature of PTV measurements. Mitigating these effects of poor gradient estimations more generally can be accomplished by limiting how quickly such gradients can change (Lipschitz continuity), or by forcing the gradient to exist only within a certain bound (see

Bunin et al. (2013)). However, applying these constraints aggressively can reduce the fidelity of the computed gradient, especially if there is little *a priori* information about appropriate gradient magnitudes. Therefore, inspired by the use of physical constraints in the higher-order interpolation of Eulerian velocimetry data, we propose a method for filtering an initial gradient estimate on unstructured data by enforcing physical equations of motion. We propose the use of the vorticity-transport equation as a physical constraint, as it utilizes the high-quality temporal information along a pathline (the substantial derivative of vorticity). The transport equation is also a function of every component of the velocity gradient tensor, allowing the optimization of every component of the tensor simultaneously. The vorticity-transport equation takes the following form:

$$\frac{\mathrm{D}\vec{\omega}}{\mathrm{D}t} = (\vec{\omega} \cdot \nabla)\vec{U} + \nu\nabla^2\vec{\omega} \ , \tag{5.1}$$

where the terms from left to right are the substantial derivative of vorticity ω, vortex stretching/tilting, and the viscous diffusion of vorticity, respectively. In this study we will be neglecting viscous diffusion, under the assumption that the timescales of viscous diffusion are much greater than that of the measurement given a moderate Reynolds number. In order to cast Equation (5.1) onto a set of unstructured Lagrangian data, we will introduce nomenclature described in Figure 5.2. Here, N pathlines are enumerated by the counter p, while each pathline is tabulated in the vector $\vec{L}$, such that the number of frames in which a particle is observed is denoted $\vec{L}(p)$. At each timestep along a pathline, the position $\vec{X}$, velocity $\vec{U}$ and acceleration $\vec{a}$ of each particle are known for i timesteps. We will denote the components of these vectors with j.

The vorticity-transport equation must have no residual at any point or time, and

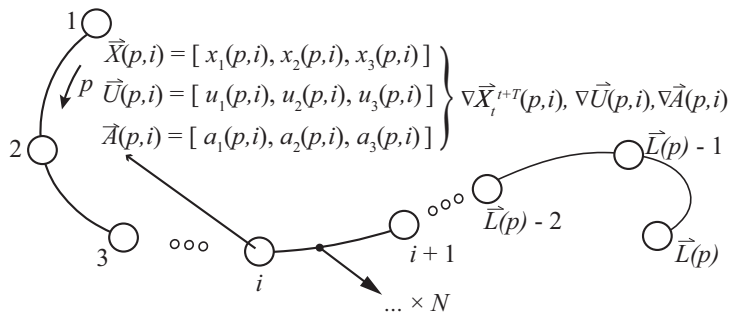

Figure 5.2: A schematic of one of N pathlines acquired within a PTV data set. The number of timesteps within each pathline are contained within the $1 \times N$ vector array $\vec{L}$, while the pathlines themselves are enumerated by counter p. As such, the number of timesteps in which the current pathline is observed is given by $\vec{L}(p)$. The timesteps along pathline p are enumerated by the counter i, and at each timestep the three-dimensional position $\vec{X}(p,i)$, velocity $\vec{U}(p,i)$ and acceleration $\vec{a}(p,i)$ have been measured. With this data set, the velocity-gradient tensor $\nabla\vec{U}(p,i)$ is to be calculated.

therefore we can estimate the quality of our gradient estimations by looking at the residual of the equation at any point:

$$R(p,i) = \sum_{j=1}^{3} \left(\frac{\mathrm{D}\omega_j(p,i)}{\mathrm{D}t} - (\vec{\omega}(p,i) \cdot \nabla) u_j(p,i) \right)^2 . \tag{5.2}$$

Rather than attempting to minimize this residual at each point individually, the maximum amount of temporal information can be transferred to the spatial gradient by minimizing this residual across an entire pathline simultaneously:

$$O(p) = \sum_{i=1}^{\vec{L}(p)} R(p,i) = \sum_{i=1}^{\vec{L}(p)} \left[\sum_{j=1}^{3} \left(\frac{\mathrm{D}\omega_j(p,i)}{\mathrm{D}t} - (\vec{\omega}(p,i) \cdot \nabla) u_j(p,i) \right)^2 \right] . \tag{5.3}$$

As an added practical benefit, this formulation operates pathline by pathline, resulting in a straightforward implementation. Recently, Schneiders et al. (2016) demonstrated a novel velocity interpolation technique that utilized full-particle trajectories in order

to improve the fidelity of velocity field reconstructions at a single snapshot. In particular, increased information gleaned from long paths showed a clear improvement in velocity reconstruction fidelity. The current study also benefits from the use of long track information, as the optimization at any given point relies in part on the optimization both upstream and downstream of that point along a given pathline. In this way, a point with a poor initial velocity gradient estimate can benefit from better initial estimates at neighbouring points along the pathline. At this point we wish to find the velocity gradient $\nabla\vec{U}(p,i)$ along the entire pathline the minimizes O, given our initial guess. There are many ways to perform this optimization, but as a proof of concept we will use a simple gradient descent method. ∇O is determined with respect to all elements of $\nabla\vec{U}(p)$. O is then minimized by iteratively adjusting each individual element of $\nabla\vec{U}(p)$ along the direction ∇O by a step α:

$$\nabla\vec{U}(p)_{k+1} = \nabla\vec{U}(p)_k - \alpha\nabla O \ . \tag{5.4}$$

The individual components of velocity determined from particle tracking are unchanged. The above optimization scheme requires an initial estimate of the velocity gradient tensor to operate on. There are many methods to produce such an initial estimate. Here, we follow the method of Meyer et al. (2001), by minimizing the residual of an overdetermined set of directional derivatives.

The procedural order to implement this gradient optimization method varies slightly from the conceptual order described above. Given particle tracking data, implementing the above-described method would take the following order:

1. An initial estimate of the velocity gradient tensor is produced, across the entire set of particles at each timestep, using an established method, such as

from an overdetermined set of directional derivatives (see: Meyer et al. (2001)), weighted-averaging technique (see: Correa et al. (2011)), or interpolation.

2. The data set is separated into pathlines, such that each pathline has $9 \times \vec{L}(p)$ velocity gradient components to be adjusted.

3. These $9 \times \vec{L}(p)$ velocity gradient components are evaluated based on the objective function in Equation (5.3).

4. The gradient of this objective function is determined by making small adjustments to the $9 \times \vec{L}(p)$ velocity gradient components.

5. New values of the velocity gradient components are determined using a steepest descent optimization following Equation (5.4) until a local optimum of the objective function is found.

It is worth noting that, given an initial estimate is available, this optimization can be performed on any track individually without any reference to other particle tracks.

In the following section, the above methodology will be evaluated on a synthetic set of pathlines in order to have access to "true" reference values, and evaluate error reduction. Following this evaluation, the methodology will be implemented on experimental data to both evaluate noise reduction on real data, and to demonstrate Lagrangian analysis.

5.4 Numerical Test Case: Dissipating Taylor-Green Vortex

Since a physical measurement would not provide any insight into error reduction for the proposed methodology, the initial evaluation presented here utilizes a synthetic

data set. A dissipating Taylor-Green vortex field in three dimensions is used for our test case (see Taylor and Green (1937)). The data set for the Eulerian field was generated using a pseudo-spectral code whose formulation and validation is briefly described below. Simulated particles that perfectly follow the flow were advected through this domain, and synthetic noise was added to the particle positions to simulate measurement error. Using the mean frame-to-frame displacement as a reference value, uniform random displacements of between 0% and 3% were applied to each particle. This is comparable to the reconstruction quality of experimental techniques such as SMART ($0.2px$ error over $6px$ frame-to-frame displacement; see Schanz et al. (2016)). The error was subsequently evaluated both before and after applying the proposed methodology. The results for this synthetic test case described below, following a brief description of the computational method.

5.4.1 Computational Methodology

For the dissipating Taylor-Green vortex, the following incompressible form of continuity and momentum equations are solved:

$$\frac{\partial u_i}{\partial x_i} = 0 \tag{5.5}$$

$$\frac{\partial u_i}{\partial t} + \frac{\partial (u_i u_j)}{\partial x_j} = -\frac{\partial p}{\partial x_i} + \frac{1}{Re_c}\frac{\partial^2 u_i}{\partial x_j \partial x_j} \tag{5.6}$$

where u_1, u_2, u_3 are the velocity components in the x_1, x_2, x_3 directions, respectively. Note that the equations have become non-dimensionalized by a characteristic length-scale L_c and velocity-scale U_c. Thus, the Reynolds number that appears in the viscous term is defined as $Re_c = U_c L_c/\nu$, where ν is the kinematic viscosity of the fluid.

Equations (5.5) and (5.6) are solved in spectral (Fourier) space using a pseudo-spectral method (see Orszag (1969) and Orszag (1972)). To remove the aliasing error, the 3/2 rule proposed by Orszag (1971) was adopted. Periodic boundary conditions are applied in all three directions with a domain size of $2\pi \times 2\pi \times 2\pi$. The governing equations are integrated in time using fractional step method (see Kim and Moin (1985)) with a second-order, three-step Runge-Kutta time-advancement scheme.

The three-dimensional dissipating Taylor-Green vortex is initialized following Canuto et al. (2007). The simulation was carried out at $Re_c = 100$ for which reference data was available from Brachet et al. (1983) and Canuto et al. (2007). The equations were integrated from $t = 0$ to $t = 16$ with grid resolution of $32 \times 32 \times 32$. This resolution was found to be appropriate for such a low Reynolds number flow based on a grid-convergence study and the above works in literature. Our data set is compared qualitatively and quantitatively against literature in Figures 5.3 and 5.4. Iso-surfaces of $u-$component of velocity are shown in Figure 5.3 for the current simulation and those of Brachet et al. (1983). Figure 5.3 (left) is the initial condition. Figure 5.3 (middle) is the current simulation at $t = 5.0$, which is the same as the results of Brachet et al. (1983), presented in Figure 5.3 (right). In addition to this qualitative comparison, the dissipation rate, $\varepsilon = \nu \left\langle \frac{\partial u_i}{\partial x_j} \frac{\partial u_i}{\partial x_j} \right\rangle$ (where $\langle ... \rangle$ indicates volume averaging), is also compared with literature and is shown in Figure 5.4. The result of the current simulation is in very good agreement with that of Brachet et al. (1983).

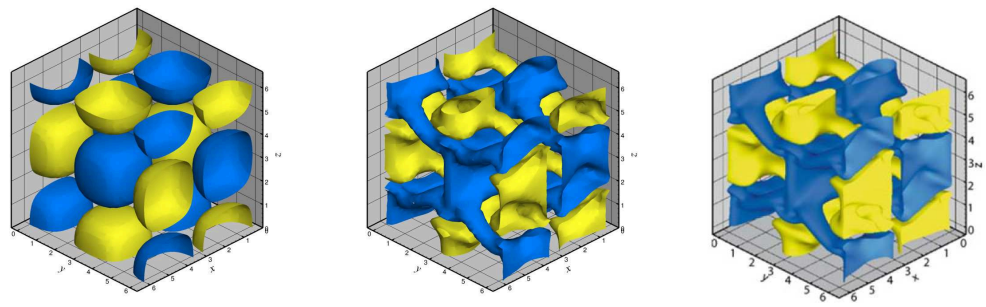

Figure 5.3: Iso-surfaces of $u-$component of velocity with levels 0.25 (yellow) and -0.25 (blue) at $Re_c = 100$. Left: initial flow field at $t = 0$. Middle: current simulation at $t = 5.0$. Right: Brachet et al. (1983) at $t = 5.0$.

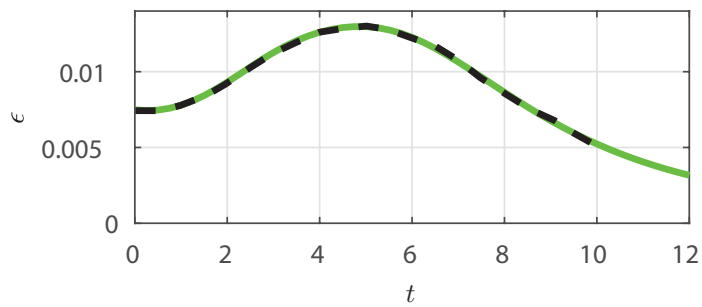

Figure 5.4: Dissipation rate for Taylor-Green vortex at $Re_c = 100$. Current study (solid); Brachet et al. (1983) (dashed).

5.4.2 Results: Proposed Method Operating on the Dissipating Taylor-Green Vortex

Figure 5.5 shows snapshots of particles coloured by the root-mean-square (RMS) error of velocity-gradient components both before and after the vorticity-correction method was applied for high and low seeding densities. Here, the RMS error is computed across the individual elements of the velocity gradient tensor, instead of an ensemble of measurements:

$$\text{Error} = \sqrt{\frac{1}{9}\sum_{i=1}^{3}\sum_{j=1}^{3}\partial_i u_j^2}\ . \tag{5.7}$$

The *before* image is of the initial velocity gradient estimate produced utilizing the method of Meyer et al. (2001). The snapshots are taken at $t = 5$, or approximately 1.5 convective times through the simulation. The RMS error of the velocity gradients range up to approximately 3% before correction, as expected given the magnitude of noise applied to the advected particles. Error is dramatically reduced by the vorticity-correction method throughout the domain for both seeding densities shown. These observations can be seen more clearly in the supplementary videos "*Supplementary_Video_5-1.mp4*" and "*Supplementary_Video_5-2.mp4*" This reduction in error was achieved at relatively low computational cost, with MATLAB-based implementation on a desktop-class computer optimizing approximately 25-100 pathlines per second, depending on seeding density.

In addition to the error shown in Figure 5.5, the vorticity field can also illustrate how the vorticity correction method is applied. Figure 5.6 shows the vorticity-magnitude sampled on a plane one half-wavelength from the centre of the computational domain ($z = \pi/2$). The time-step of this sample was chosen to be early in the simulation such that there were still large structures to identify, and the highest seeding density was used here. This vorticity field is shown interpolated onto an Eulerian grid as a contour plot. While the vorticity correction method does not recover the true gradients exactly, the alternating pattern of vorticity magnitude into nearly-circular structures is much more evident after correction than before.

Four seeding densities were evaluated following the same methodology. The average error was determined at each seeding density through the arithmetic average of RMS errors across the entire spatial and temporal domain, shown in Figure 5.7. The initial cases, indicated with crosses, are the initial gradient estimates used as an

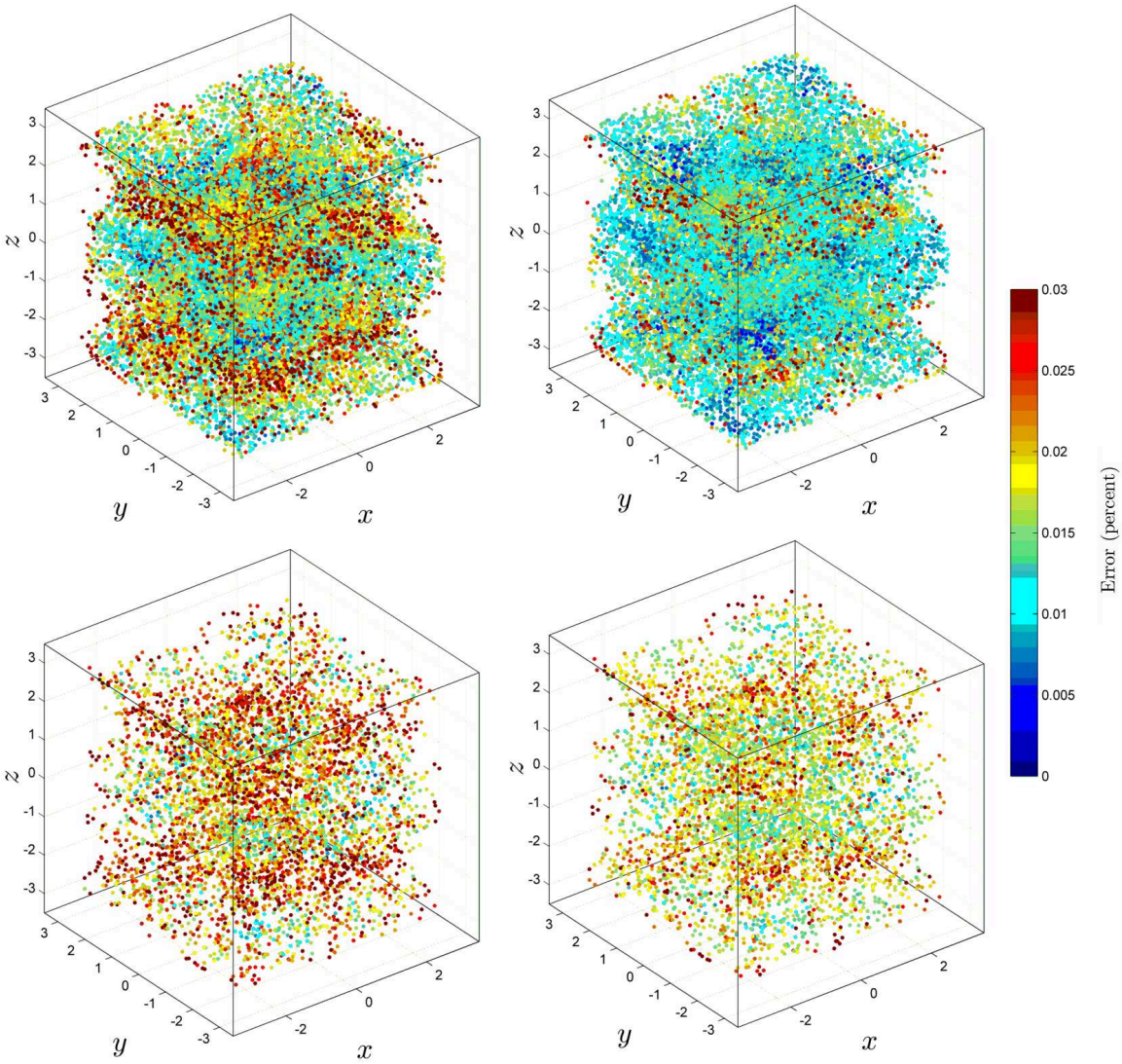

Figure 5.5: Particles were advected through the dissipating Taylor-Green vortex field with some artificial noise, and the resulting tracks were processed as if they were PTV data. The resulting RMS error in velocity-gradient components is shown for $t = 5$. The upper row shows a high particle-density case before (left) and after (right) the vorticity correction scheme was applied. The scatter plots on the second row shows a intermediate particle-density case. In both cases, the vorticity correction scheme shows a dramatic reduction in RMS error. For each seeding density, the side-by-side comparison before and after correction can be viewed as a time sequence in the supplementary videos "*Supplementary_Video_5-1.mp4*" and "*Supplementary_Video_5-2.mp4*"

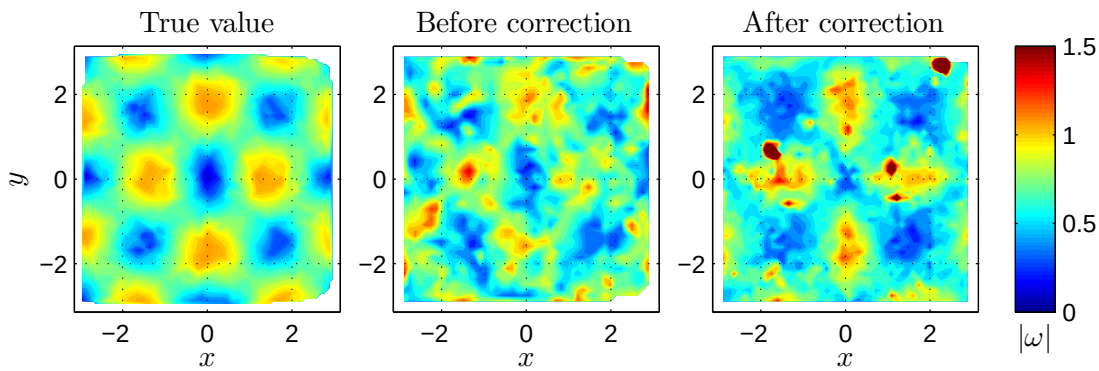

Figure 5.6: Vorticity magnitude is shown here for the plane $z = \pi/2$ for the high particle-density case. While the recovery if the vorticity pattern is not perfect, the alternating circular pattern is much more evident after the correction scheme is applied.

input for the gradient optimization. While higher seeding densities presented lower error both before and after correction, the vorticity-correction methodology reduced mean error across all cases, with a maximum reduction in error of approximately 40%. It is speculated that the variation in converged error values with respect to seeding density is due to the simple gradient descent method uses here, which is only capable of determining local optima. As such, in its current implementation this gradient optimization technique is dependent on initial conditions. However, the larger error reduction (as a fraction of the initial error) observed at a particle count of 6000 is not expected to be an artefact of the random initialization as the particle positions were all confirmed to be uniform at their initialization. Moreover, this case still represents approximately 10^7 individual gradient estimations, reducing the likelihood of random error. Figure 5.7 also shows the reduction in the objective function O as expressed in Equation (5.3), as a function of iteration. The function quickly converges upon its final value within five to ten iterations, with an overall reduction of approximately

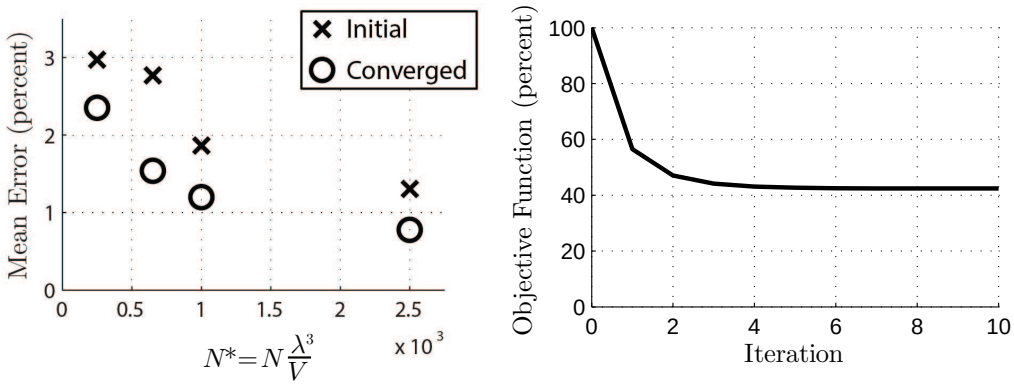

Figure 5.7: The per-particle RMS error averaged across the whole computational domain for four different seeding densities. The vorticity-correction method reduced error across all seeding densities (left). The highest and second-lowest seeding densities in this Figure are those shown in Figure 5.5 as high-density and intermediate-density, respectively. The reduction in the objective function is also shown here, as a function of iteration (right).

60% versus the initial value of the function.

5.5 Experimental Test Case: Starting Vortex on an Accelerating Circular Plate

Given the reduction of error produced by the vorticity-correction method on synthetic data, as demonstrated in Figure 5.5, we will now apply the method to experimental data derived from a single image sequence. The test case consists of the vortex wake behind a circular flat plate towed at a constant acceleration. The experimental setup is explained below.

5.5.1 Experimental Apparatus and Image-Processing Methodology

To test the gradient-evaluation method presented in Section 5.3, 4D-PTV (also known as *Shake-the-Box*) data was collected along the leeward side of a linearly accelerating

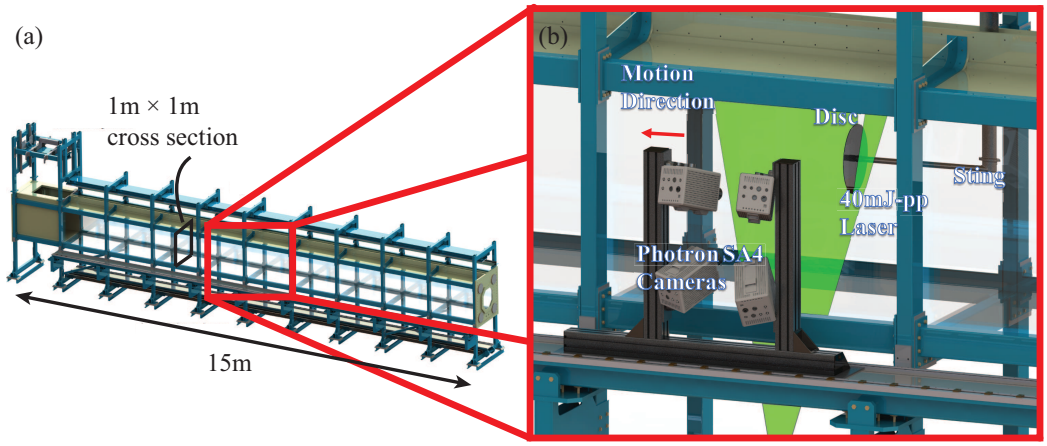

Figure 5.8: Schematic of the experimental apparatus: (a) A $D = 30$cm circular plate was accelerated at at a non-dimensional rate of $a^* = aD^3/\nu^2 = 1.1 \times 10^{10}$ through a 15m-long, 1m × 1m square cross-section optical towing tank; (b) Particles were illuminated with a 40mJ per-pulse laser and captured using four Photron SA-4 cameras.

circular plate. A schematic of the experimental apparatus is shown in Figure 5.8. The experiments was performed in the 15m-long, 1m × 1m cross-section optical towing tank at Queen's University. Three-sided optical access is provided from the two side-walls and the bottom of the towing tank. An impulsively started circular plate of diameter $D = 30$cm was accelerated normal to its path at a dimensionless acceleration of $a^* = aD^3/\nu^2 = 1.07 \times 10^{10}$, where a and ν represent dimensional acceleration and kinematic viscosity, respectively. The motion was achieved by a rack-and-pinion traverse above the towing tank. The sting holding the circular plate was $2D$ long, with a circular profile and a diameter of $0.1D$, attaching to the plate on its suction side. The blockage ratio of the experiment is 7%. The sting assembly and optical setup are shown in Figure 5.8(b). Further documentation on this experiment can be found in Fernando and Rival (2016).

$55\mu m$ polymer spheres were seeded in the flow to serve as tracer particles. The

Stokes number of the particles was approximately 3×10^{-3}, which ensured tracer-accuracy errors of $< 1\%$ (see Raffel et al. (2007)). The tracers were illuminated by a 527nm, 40mJ-per-pulse laser expanded into a $10 \times 10 \times 0.3\text{cm}^3$ volume. Four Photron SA4 high-speed cameras captured images of the tracers within this volume at a frame rate of 900Hz. To minimize image distortions, water-filled prisms were fixed onto the glass pane of the tank such that all cameras were orthogonal to a prism face. The acquired images were then processed in DaVis 8.3.0 and using a 4D-PTV tracking algorithm; see Schanz et al. (2016) for details. Measurements were performed over a diameters-traveled domain of $0.1 \leq s/D \leq 0.28$, which corresponds to circulation-based Reynolds numbers between $9 \times 10^3 \leq \text{Re}_\Gamma \leq 43 \times 10^3$. Finally, the 4D-PTV pathlines were then extended forwards and backwards beyond their original lifespan via a pathline-extension method inspired by flow-map compilation techniques described in Brunton and Rowley (2010) and Raben et al. (2014).

5.5.2 High-Fidelity Measurements of the Starting Vortex Growth

As direct estimates for gradient errors are no longer accessible, an instantaneous snapshot of the vorticity field is instead presented in Figure 5.9 to demonstrate the increase in fidelity offered by the proposed vorticity-correction method. As in the numerical test case, the *before* image is of the initial velocity gradient estimate produced utilizing the method of Meyer et al. (2001). The noise of the starting vortex is dramatically reduced, allowing for the identification of structures not previously obvious, such as individual Kelvin-Helmholtz instabilities in the shear layer. These structures would also be obscured by ensemble-averaging, such that the ability to correct individual runs is critical. This noise reduction is more clearly shown in the supplementary video

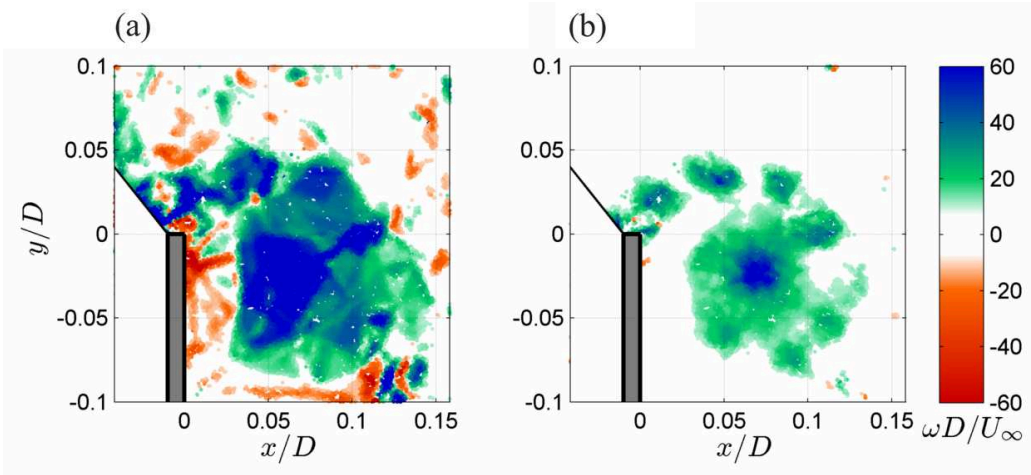

Figure 5.9: An instantaneous snapshot of the vorticity field captured from a single image sequence is shown here (a) before and (b) after vorticity-correction on flow-compiled PTV data. The correction scheme allows for the identification of individual instabilities in the shear layer, and the clear identification of the vortex core. This side-by-side comparison is available as a time sequence in the supplementary video "*Supplementary_Video_5-3.mp4*"

"*Supplementary_Video_5-3.mp4*". The concentric circular vorticity levels also clearly identify the vortex core in the corrected vorticity field. Although the vorticity scale is saturated in Figure 8(a), it is worth noting that the small-scale structures remain obscured at all scaling levels. Furthermore, it should be noted that the vorticity correction method will often increase velocity gradient magnitudes, and does not simply smooth the gradient values. The computational cost of the proposed methodology did not significantly increase for the experimental data relative to the synthetic data, correcting pathlines on the order of 10 per second on a desktop-class computer.

In order to give a rough estimate of both the computational cost and the reduction in the objective function, the objective function O as expressed in Equation (5.3) is shown in Figure 5.10. Despite the simple optimization method used in this study, the residual of most pathlines converged on its final value after five to ten iterations.

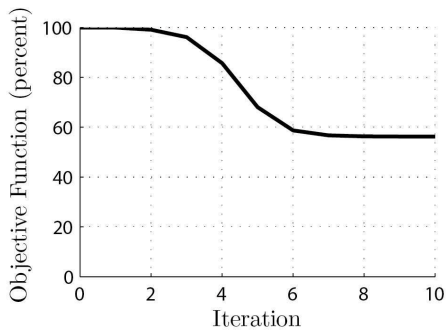

Figure 5.10: The magnitude of the objective function along an individual pathline is shown here as a function of iteration to visualize both the noise reduction observed and the computational speed. The 40% reduction in the objective is similar to the 40% reduction in error observed in synthetic data.

However, it is worth noting that in the absence of an objective true value with which to compare to, no quantitative treatment of error reduction can be given here. The convergence on a local minimum, as opposed to zero, was seen as acceptable in order to avoid gradient estimations tending towards zero.

We can demonstrate the utility of this high-fidelity result in Figure 5.11. Here, we are now able to accurately identify key features in the flow due to the smooth, well-resolved vorticity field. Having identified a flow feature, the mass in that structure can then be tracked backwards in time along pathlines back to its source, as shown on the right in Figure 5.11. Pathlines are coloured by time overlayed on a snapshot of vorticity from the later-most timestep of the dataset. In this way, we are able to identify where vorticity-containing mass originated. Alternatively, the left of Figure 5.11 shows pathlines tracked forwards in time from a vorticity source. This forward and backward tracking together define the relationship between the resulting flow topology and vorticity source.

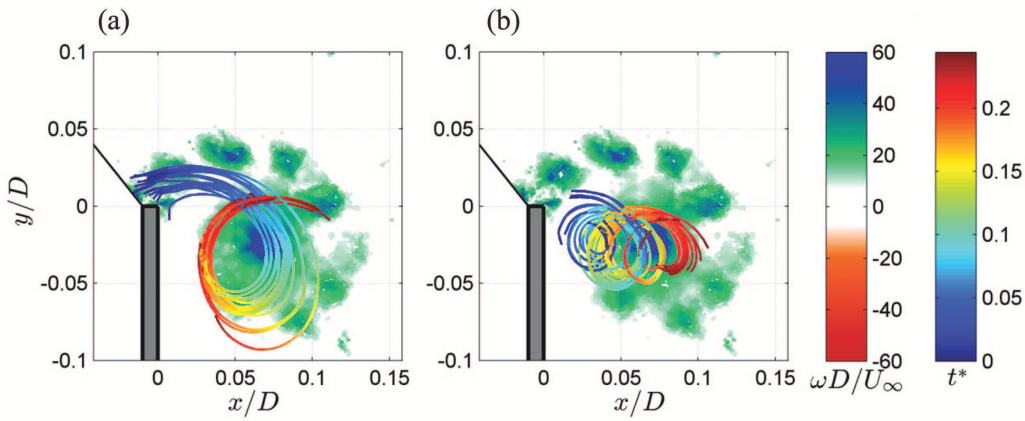

Figure 5.11: Utilizing the pathline information can elucidate material transport within a flow. For instance, on the left (a) particles are tracked forward in time from the shear layer to a later time-step, shown here overlayed on the vorticity field at that later time-step. This shows the advection of material from a vorticity source. Alternatively, particles can be tracked from the vortex core backwards in time, shown in the right (b), to identify the origin of that vorticity-containing mass.

5.6 Conclusions

The purpose of this study was to improve the estimation of spatial gradients on unstructured Lagrangian data without discarding any pathline information. Such robust gradient estimation can improve the understanding of vorticity transport through a flow for the purposes of aerodynamic or hydrodynamic optimization or flow control. Therefore, we proposed a gradient correction scheme based on the knowledge that the substantial derivative of vorticity through a flow must equal the vortex stretching/tilting through that flow. This constraint was realized by minimizing the residual of the vorticity-transport equation across all points of an individual pathline simultaneously.

The proposed method has been implemented on both synthetic and experimental data consisting of a decaying Taylor-Green vortex field and an accelerating circular

plate, respectively. In the synthetic case, mean errors were shown to be consistently reduced by the proposed vorticity-correction method across all seeding densities, by up to 40%. However, as the method shown here is locally optimizing, the error reduction achieved is dependent on the spatial resolution of the initial gradient estimate. Meanwhile, the application of the proposed method to experimental data reduced the vorticity-transport residual by approximately 40%. The proposed method also provided access to small-scale flow structures such as the Kelvin-Helmholtz instabilities that were otherwise obscured. This retention of Lagrangian data was demonstrated with the direct investigation of material transport within a starting vortex. Small-scale flow structures could be identified in the post-processed data that were otherwise unavailable to the raw gradient outputs. By identifying those flow structures one could then track the vorticity-containing mass back to its origin. This experimental case demonstrates the value of retaining Lagrangian data for aerodynamic or hydrodynamic optimization, which could eventually lead to new insights when studying complex, vortical flows.

Chapter 6

Modelling Circulation Redistribution in Leading-Edge Vortices with Spanwise Flow

6.1 Abstract

A model for the spanwise transport of circulation within a leading-edge vortex (LEV) is proposed and validated, based on one-dimensional species advection. The model is composed of two parts: first, a shear layer model predicts the circulation feeding rate into the LEV; and second, a spanwise transport model initializes vorticity-containing mass with a finite circulation, allowing mass to advect along the span with the spanwise flow. No empirical data is necessary to inform the results of the model. Both components of the proposed model are validated separately, using a flat-plate delta wing as a test case. Utilizing high-speed particle image velocimetry (PIV) to measure the shear-layer velocity, the proposed shear layer model is found to predict circulation flux into the LEV. Four-dimensional particle tracking velocimetry (4D-PTV) is used to validate the spanwise transport of circulation. By allowing vorticity-containing mass to advect along the span with the spanwise flow, it is found that the model automatically satisfies the vorticity transport equation, when vortex tilting and the

viscous diffusion of vorticity are neglected. The magnitude of the neglected vorticity transport terms is approximately 10% that of spanwise circulation advection, such that these terms do not significantly affect the outcome of the model. Thus, the proposed model represents a computationally inexpensive tool for predicting circulation redistribution in an unsteady, three-dimensional LEV.

6.2 Introduction

The rapid flapping motion of an insect wing produces a strong and compact leading-edge vortex (LEV), as identified by Ellington et al. (1996). Such structures are also found in fish and bird locomotion (see Videler et al. (2004), Borazjani and Daghooghi (2013)), and either their engineering analogues of autonomous underwater vehicles (AUVs) and micro-aerial vehicles (MAVs), respectively. While the investigation of the LEV in relation to biological locomotion has received significant attention only since the mid-1990s following Ellington et al. (1996), similar LEVs have been of engineering interest on delta wings for decades, as exemplified by Polhamus (1966). In each of these aforementioned cases, the LEV develops in the pattern illustrated by Figure 6.1: vorticity formed in a leading-edge shear layer is fed into the vortex, and if spanwise flow exists, that vorticity may be advected along the leading-edge in the outboard direction.

An LEV that forms on a nominally two-dimensional profile with no spanwise flow will always eventually detach and convect downstream (see Rival et al. (2014)). For such a case, the development of an LEV on a pitching or heaving profile is influenced by a small number of parameters, as identified by Rival et al. (2009), Baik et al. (2012), Widmann and Tropea (2015), and Wong and Rival (2015). In particular, the Strouhal

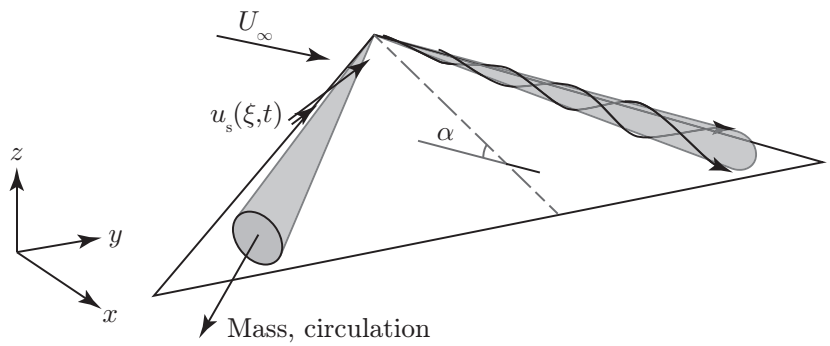

Figure 6.1: The LEV formed on the suction side of a delta wing is fed by a leading-edge shear layer. In order fo this LEV to remain stationary, the vorticity-containing mass fed into the LEV must be balanced by spanwise transport of vorticity-containing mass or vorticity annihilation. ξ is the coordinate along the shear layer.

number St determines force generation, while the reduced frequency k dominates the flow topology and the eventual detachment of the LEV. In turn, when the circulation of an LEV is normalized by its feeding shear-layer velocity, Onoue and Breuer (2016) found that circulation was not affected by reduced frequency. A very large reduced frequency k represents a very fast motion compared to the development time of the LEV, and subsequently the LEV never grows large enough to detach over the course of the cycle. Several very powerful methods exist for predicting the development of the LEV in two-dimensional cases for arbitrary motions, especially using discrete vortex methods such as those exemplified by Ramesh et al. (2014) and Hemati et al. (2014). However, these two-dimensional cases represent only a small subset of the LEVs that are observed in engineering practice.

A canonical three-dimensional LEV is that of a delta wing, as shown in Figure 6.1. This LEV would rapidly saturate and detach if vorticity-containing mass was not advected away along the span of the profile. This same physics governs LEV formation in biological and bio-inspired swimmers and flyers, where leading-edge curvature is

used to manipulate circulation and mass transport, as shown by Hartloper and Rival (2013). For instance, Hartloper and Rival (2013) noted similar lunate tail fins in several species of swimmers, while Videler et al. (2004) observed that the pronounced leading-edge curvature of common swifts was utilized to form a stable LEV. Both the spanwise advection of vorticity and the annihilation of vorticity are critical circulation regulating mechanisms, as shown by Wong and Rival (2015) and Eslam Panah et al. (2015), respectively. The spanwise advection of vorticity is especially difficult to account for, as most models for LEV growth are explicitly two-dimensional, such as the strip-theory approach used in Jain et al. (2015). Therefore, the current study provides a design tool appropriate for both engineering practice and in the study of biologically-inspired flows, by explicitly accounting for this spanwise circulation transport.

The proposed design tool is a computationally-inexpensive model for LEV growth in the presence of spanwise flow. This model is derived in the following section, based on a Monte Carlo simulation of the advection of vorticity-containing mass along the span of a profile. In order to validate this model, a canonical LEV is produced experimentally utilizing a non-slender flat-plate delta wing, as described in Section 6.4. However it should be noted that this model is also applicable to biological and bio-inspired flows. The resulting LEV is investigated in Section 6.5 utilizing high-speed particle image velocimetry (PIV) to validate estimates for circulation entering the LEV, while four-dimensional particle tracking velocimetry (4D-PTV) is used to resolve the distribution of circulation along the span, and thus validate the spanwise advection model.

6.3 A One-Dimensional Monte-Carlo Simulation of Circulation Transport

Previous modelling efforts have either suffered from limited three-dimensional information, or a dependence on empirical data, such as shear-layer thickness or velocity, as in the case of Wong et al. (2013a). The proposed model attempts to solve these limitations by treating circulation transport in the same way as other species transport phenomena, where circulation follows the flow of mass through the domain. Such a model requires the assumptions of limited vortex tilting and rapid advection relative to the diffusion of vorticity. While vortex stretching can be included in this model, it does not affect the outcome as vortex stretching is a circulation-conserving process. This model can be divided into two parts: the feeding of circulation through a shear layer; and the subsequent transport of that circulation along the span of a profile. These two parts are each discussed in the following sections.

6.3.1 Shear-Layer Feeding

Wong and Rival (2015) give the feeding of a vortex as:

$$\frac{\partial \Gamma}{\partial t} \propto u_{\text{eff}}^2 \ , \tag{6.1}$$

where u_{eff} is the effective velocity of the profile. The constant of proportionality depends on the shape of the velocity profile in the shear layer. More precisely, this expression for shear-layer feeding can be expanded as:

$$\frac{\partial \Gamma}{\partial t} = \frac{\partial \Gamma}{\partial m'} \frac{\partial m'}{\partial t} \ , \tag{6.2}$$

where m' is the mass per unit span at a location of interest. Following the diagram of the shear layer in Figure 6.2, the circulation about the shear layer is $\Gamma = u_o l$, where u_o is the outer shear-layer velocity. Meanwhile, the mass inside the shear layer (per unit span) is $\rho d l$. Thus, we can insert specific values into Equation (6.2) so as to obtain:

$$\frac{\partial \Gamma}{\partial m'} \frac{\partial m'}{\partial t} = \left(\frac{u_o l}{\rho d l} \right) \left(\tfrac{1}{2}(u_o + u_i)\rho d \right) = \tfrac{1}{2}(u_o^2 + u_o u_i) \ , \tag{6.3}$$

where u_i is the inner shear-layer velocity and can be assumed to be zero. Setting $u_i = 0$ gives a circulation feeding rate of:

$$\frac{\partial \Gamma}{\partial t} = \tfrac{1}{2} u_o^2 \ , \tag{6.4}$$

which is similar to the feeding rate for vortex rings determined in the literature, such as in Didden (1979). Therefore, we need only to compute the outer shear-layer velocity in order to estimate the flux of vorticity into the LEV.

Roshko (1954) gives the velocity of a shear layer as a function of the base pressure coefficient C_{ps}, which is the pressure coefficient in the separated region of a obstacle in the flow:

$$u_o = U_\infty \sqrt{1 - C_{ps}} \ , \tag{6.5}$$

and thus the challenge is to determine a reasonable estimate for the base pressure coefficient. A general solution for the pressure difference across a stalled flat plate would constitute a solution to the unsteady lift problem, and thus such a value is unavailable. However, we can consider the solution for a normal flat plate as a worst-case scenario in order to determine the importance of the parameter. In order to determine the sensitivity of the shear-layer velocity on the base pressure coefficient,

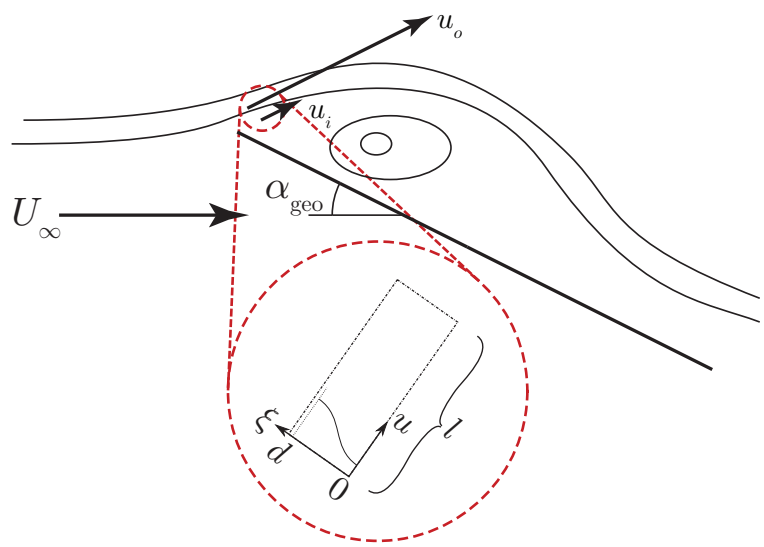

Figure 6.2: The vorticity entering the leading-edge vortex can be determined by integrating around a shear layer of length l and thickness d. Although these values are important for intermediate steps, all geometric constraints ultimately cancel out in the derivation. ξ is the coordinate along the shear layer.

we can determine a first-approximation of the base-pressure coefficient from a well-known drag coefficient. Using the established drag coefficient of $C_D = 1.3$ for low-aspect ratio normal flat plates (see White (1999)), a base pressure can be estimated by assuming a uniform pressure difference between the upstream and downstream surfaces of the plate. This results in a shear-layer velocity approximately 10% greater than the free-stream. Therefore, we will neglect this acceleration in the remainder of the study. It should be noted that for any dynamic motion, for instance in biological or bio-inspired profile motions, Kriegseis et al. (2013) showed that the appropriate scaling velocity for the shear layer is the effective velocity u_{eff}, and not the free-stream velocity U_∞. This allows for the extension of the above model to include unsteady biological and bio-inspired locomotion modes, in addition to delta wings and rotating machinery.

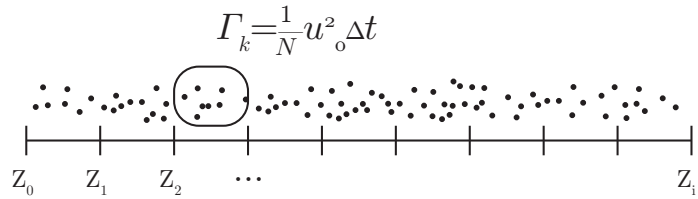

Figure 6.3: In the proposed model, particles representing vorticity-containing mass are initialized randomly along the span of the profile at every timestep. As the local circulation generated at any timestep is $\Delta t u_{\text{eff}}^2$, this circulation is divided equally among all the particles within a spanwise bin.

6.3.2 Spanwise Circulation Transport

The assumption that circulation follows the mass in the flow is valid for flows with small vortex tilting and higher Reynolds numbers where viscous diffusion is small relative to convection. While this dramatically simplifies the analysis of circulation transport, it still requires the computation of mass transport within the flow. Estimating mass transport explicitly would require empirical values such as the shear-layer thickness, which should ideally be avoided. A solution to this problem is proposed here, where mass is treated implicitly in a Monte Carlo simulation.

At each timestep, particles are initialized randomly in a continuous uniform distribution along the spanwise domain of the profile, as shown in Figure 6.3. This spanwise domain is discretized into i bins, each representing one spanwise slice that is treated locally as two-dimensional. The circulation generated at that spanwise slice $\Delta\Gamma = u_o^2 \Delta t$ is divided equally among all the particles in that domain, where this shear-layer velocity may vary along the span for rotating or flapping profiles. Thus, every particle is initialized with the circulation:

$$\Gamma_k = \frac{1}{N} u_o^2 \Delta t \ . \tag{6.6}$$

In the current study, the shear-layer velocity u_o is uniform, but for flapping or rotating profiles it may vary as a function of span. These particles are assumed to always retain their initial circulation, for the duration of the simulation. This assumption is equivalent to assuming that circulation transport is dominated by advection, such that circulation follows regular species transport.

Spanwise flow is accounted for by advecting these particles through the domain at the spanwise velocity, as shown in Figure 6.4. As these particles represent vorticity-containing mass, their velocity is exactly the spanwise flow by definition. Thus, at each timestep j, the circulation for a spanwise location z_i is the sum of the elemental circulation of all the particles generated at that location and time-step, plus the circulation of particles initialized at prior timesteps that advected to that spanwise location:

$$\Gamma(z_i) = \sum_{k=1}^{N} \Gamma_k \ . \tag{6.7}$$

As an example, consider the delta wing of sweep angle $\Lambda = 45°$ travelling at a constant velocity U_∞. If we assume that the spanwise flow is equal to half of the component of the free-stream velocity aligned with the span, the spanwise flow will be $w = U_\infty/(2\sqrt{2})$. The factor of 1/2 is a first-approximation of the no-slip condition at the surface of the profile. The resulting spatially- and temporally-resolved circulation distribution is shown in Figure 6.5, normalized for a chord of c. As one would expect, the circulation distribution rapidly approaches a steady value, with a linearly increasing circulation towards the profile tip.

By integrating the vorticity transport equation, Wong and Rival (2015) gives the

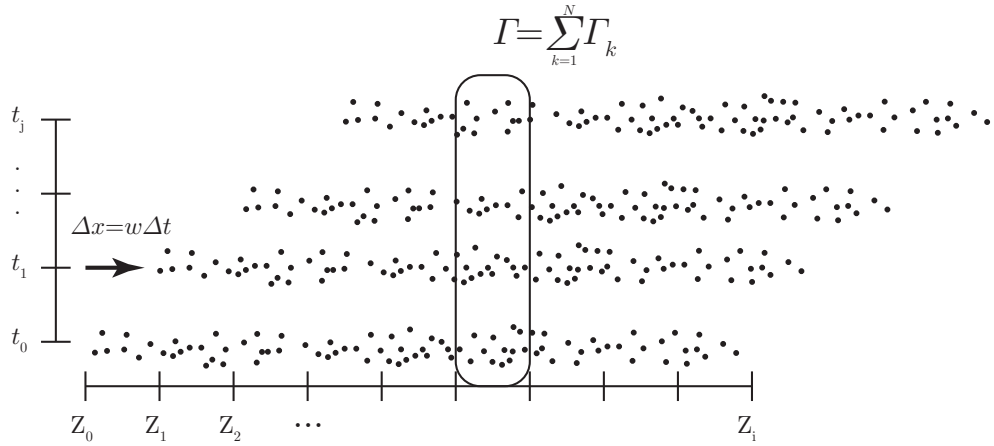

Figure 6.4: At each timestep, particles from previous timesteps are advected along the span of the profile by the spanwise flow w. Each spanwise location has a total circulation Γ determined by all the particles in that bin, both from the current timestep and all prior timesteps.

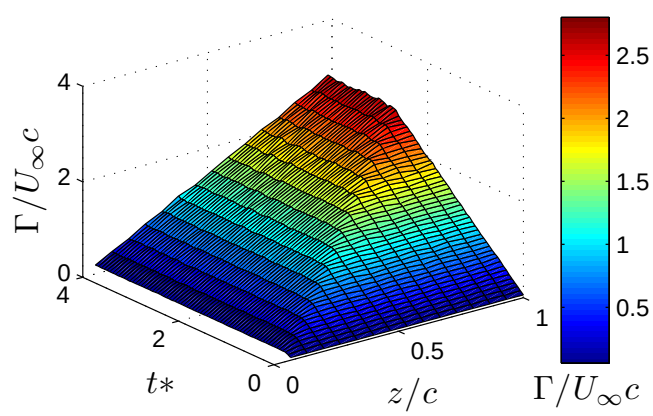

Figure 6.5: The time- and spanwise-resolved solution to the vortex growth on a delta wing converges upon a conical circulation distribution. This conical circulation distribution satisfies the vorticity transport equation when diffusion and vortex tilting are neglected.

circulation advection out of the vortex as:

$$\frac{\partial \Gamma}{\partial t} = w \frac{\partial \Gamma}{\partial z} \ . \tag{6.8}$$

When computing the circulation gradient $\partial\Gamma/\partial z$, we find that it satisfies the relationship:

$$\frac{\partial \Gamma}{\partial z} = \frac{\frac{1}{2}u_o^2}{w} \ , \tag{6.9}$$

meaning that all of the circulation that enters the vortex is being advected along the span. In this way, the Monte Carlo simulation is satisfying the vorticity transport equation simply by advecting circulation along the span with spanwise flow. The model presented above is validated with the experiments described in the following section.

6.4 Experimental Methods

A non-slender, flat-plate delta wing with sweep angle $\Lambda = 45°$ is used here as a canonical test case, as it exhibits a strong, stationary LEV that can be easily characterized by optical measurements. Although the LEV in this case is a stationary vortex with a uniform shear-layer feeding, the proposed Monte Carlo method is capable of resolving time-varying cases with non-uniform feeding, such as rotating and flapping wings. This delta wing is investigated in the 15 m-long optical towing tank at Queen's University, as shown in Figure 6.6. The towing tank has a 1×1 m^2 cross-section, with optical access through both side walls and the floor, while the partially-enclosed roof section mitigates surface waves. A high-speed rack-and-pinion traverse was used to tow the delta wing, which was mounted to a sting via the pressure-side of the

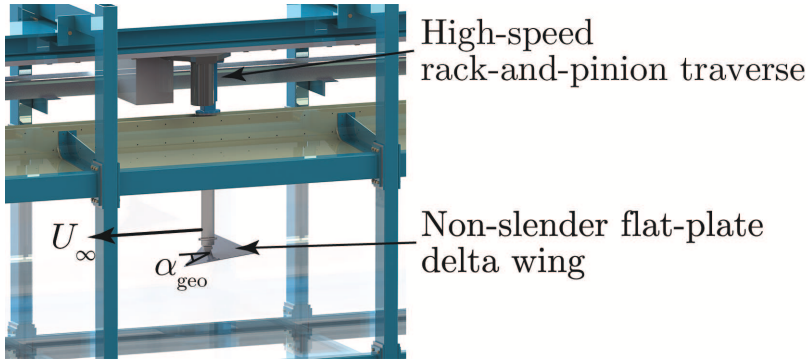

Figure 6.6: A rack-and-pinion traverse is used to tow a flat-plate delta wing at a Reynolds number of Re =250,000. The wing was mounted to a sting by its pressure-side, which extended up 0.5 m to the high-speed traverse.

profile. A geometric angle-of-attack of $\alpha_{\text{geo}} = 20°$ is utilized for all measurements, and the delta wing is towed at a velocity of $U_\infty = 0.833 m/s$, corresponding to a Reynolds number of Re =250,000. The resulting flow-fields are captured with two different measurement techniques in order to characterize the small-scale shear layer and large-scale circulation transport, described in the two following sections, respectively.

6.4.1 High-Speed Shear-Layer Measurements

In order to test the shear-layer feeding model, high-speed planar particle image velocimetry (2D-PIV) measurements are conducted over a small field-of-view, as shown in Figure 6.7. This field-of-view is approximately 30×30 mm^2, illuminated with a 527 nm Photonics Industries 40 mJ-per pulse Nd:YLF laser. This field of view is placed at the half-span location, half way between the apex of the delta wing and the wing tip. The laser is used to illuminate 100 μm hollow glass micro-spheres seeded into the flow, which are tracked with a Photron SA-Z high-speed camera operating at 10,000 Hz at a resolution of 1024×1024 px^2. Relatively large 64 px interrogation

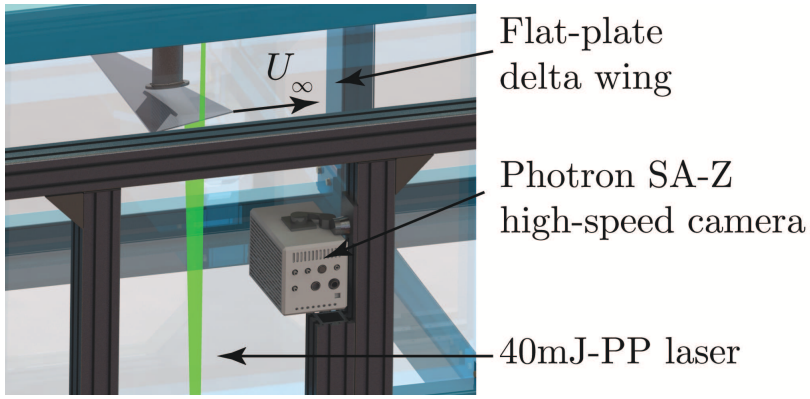

Figure 6.7: The shear layer on a flat-plate delta wing is captured using time-resolved PIV. $100\mu m$ hollow glass microspheres were illuminated with a $40mJ$ per-pulse high-speed laser and captured using a Photron SA-Z camera at 10,000 Hz. The field of view on the suction side (bottom) is approximately 30×30 mm^2.

windows are used for PIV processing in order to compensate for the small field of view, and an adaptive weighting scheme is applied to compensate for the high shear expected in the leading-edge shear layer. A single run of data was used to produce the shear-layer measurements. However, data from 200 adjacent frames were cast into the plate-fixed coordinate frame and averaged in order to produce the final vector field. The PIV algorithm is implemented in LaVision Davis 8.2.0.

6.4.2 Spanwise-Resolved Circulation advection Measurements

Four-dimensional particle tracking velocimetry (4D-PTV), as described by Schanz et al. (2016), is used to capture the integral properties of the vortex above the flat-plate delta wing. The volumetric, time-resolved data is necessary in order to measure gradients of circulation along the span. The measurement system is illustrated in Figure 6.8. 100 μm hollow glass micro-spheres are seeded into the flow and illuminated with the same 40 mJ-per pulse laser as in the 2D-PIV measurements. The laser

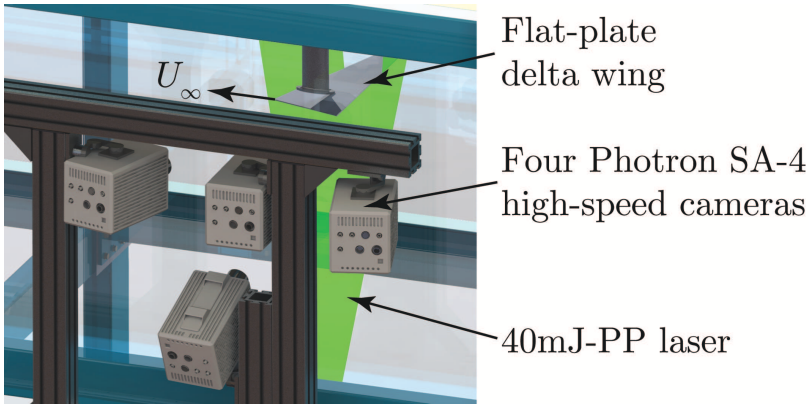

Figure 6.8: Volumetric, time-resolved 4D-PTV measurements were used to characterize the velocity gradient tensor, in order to validate the Monte Carlo simulation described in Section 6.3. $100\mu m$ hollow glass microspheres were illuminated with a $40mJ$ per-pulse high-speed laser and captured using four Photron SA-4 cameras at 1,500 Hz. The field of view as approximately $120\times120\times10$ mm^3, located on the suction side (bottom) of the model.

is expanded to a much larger control volume than for the 2D-PIV measurements, measuring $120 \times 120 \times 10$ mm^3, once again at the half-span. Particle images are then captured with four Photron SA-4 high-speed cameras, operated at 1500 Hz at a resolution of 1024×1024 px^2. Once again, a single run was used to characterize the vorticity transport within the domain, where data from 50 adjacent frames were cast into the plate-fixed coordinate frame and averaged in order to produce the final vector field. The 4D-PTV algorithm used in this study is implemented in LaVision Davis 8.3.0 software. 4D-PTV has been shown to have a triangulation error of approximately half that of tomographic-PIV, with triangulation errors of 0.1 px being typical in the current study.

6.5 Results and Discussion

The measurements of the flat-plate delta wing are used here to validate the Monte Carlo simulation. First, the small-scale shear-layer measurements will be used as reference, followed by the large-scale circulation transport and spanwise flow.

6.5.1 Shear-layer flux

The small-scale PIV measurements are shown in Figure 6.9 for both the velocity and vorticity fields. After re-casting the velocity field into the plate-fixed frame of reference, the vectors were then averaged in time in order to improve the signal-to-noise ratio. The shear layer is sampled in order to measure the circulation feeding into the LEV. The black lines shown in Figure 6.9 (a) are used to sample the effective velocity u_{eff}/U_∞ following the method of Wong and Rival (2015), which is used in the Monte Carlo simulations. Meanwhile, the black lines in Figure 6.9 (b) are used to sample $u_x\omega_z$ following the method of Wojcik and Buchholz (2014) in order to produce the reference circulation feeding values. Multiple samples were utilized in order to investigate the sensitivity of the shear-layer measurements to the chosen sampling position.

The sampled shear-layer velocities u_{eff}/U_∞ are shown in Figure 6.10 (a), while the vorticity fluxes $u_x\omega_z$ are shown in Figure 6.10 (b). While velocity profiles are insensitive to sampling position within the shear layer, it can be seen that the vorticity-flux profile varies with the sampling location, based on the inclination of the shear layer. However, the integral of the vorticity flux is insensitive to the sampling location, as the vorticity layer is merely translated up as you progress in the streamwise direction. Integral vorticity flux values were $\partial\Gamma/\partial t = 0.43$, 0.42, and 0.38 at the three sampled

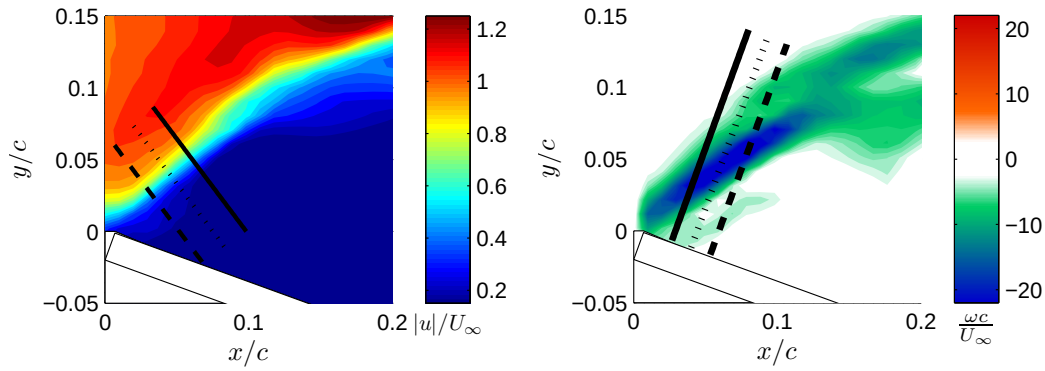

(a) (b)

Figure 6.9: The shear-layer feeding rate can be characterized in one of two ways: (a) the rate of circulation feeding is proportional to the square of the effective velocity u_{eff}^2 following Equation (6.4), or; (b) the rate of circulation feeding is the integral of the product of chordwise-velocity and vorticity following Equation (6.11). While the first method avoids any empirical dependence on the shear-layer thickness, its accuracy must be validated.

locations from upstream to downstream locations, respectively. The modelled outer shear-layer velocity, assuming $C_{\text{ps}} = 0$, is slightly lower than the measured value of $u_{\text{eff}}/U_\infty = 1.27$. As the worst-case scenario, shear-layer acceleration discussed in Section 6.3.1 for a normal flat plate exhibited similar velocities to that observed here. Therefore, the observed shear-layer velocities suggest limited sensitivity to the geometric angle-of-attack α_{geo}. However, the measured inner shear-layer velocity of $u_i \approx 0$ confirms the assumption used in Section 6.3 of a negligible inner velocity. This modelled velocity gave a shear-layer feeding of:

$$\frac{\partial \Gamma}{\partial t} = \frac{1}{2} u_{\text{eff}}^2 = 0.383 \ \tfrac{m^2}{s^2} \ . \tag{6.10}$$

Meanwhile, the measured vorticity flux following the method of Wojcik and Buchholz

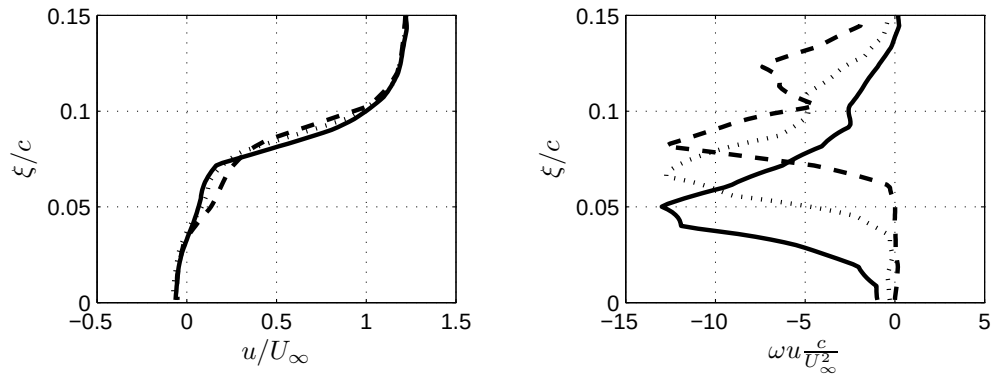

(a) (b)

Figure 6.10: The velocity profiles sampled in Figure 6.9 are shown here as a function of the shear-layer coordinate ξ. The velocity profile u_{eff} and the vorticity flux $u_x\omega_z$ produce nearly identical circulation feeding rates.

(2014) gave a very similar value:

$$\frac{\partial \Gamma}{\partial t} = \int_0^d u_x \omega_z \, d\xi = 0.431 \, \tfrac{m^2}{s^2} \, , \tag{6.11}$$

where ξ is the shear-layer coordinate. These results validate that the shear-layer feeding model predicts circulation feeding to within approximately 10 %. This model avoids the explicit use of the shear-layer thickness, eliminating the empiricism required for a shear-layer feeding estimates. With this model validated, the spanwise flow and integral circulation will be analysed in the following section.

6.5.2 Spanwise Flow and Circulation Redistribution

In order to compute integral circulation transport properties, 4D-PTV data is re-cast into a plate-fixed frame of reference. That 4D-PTV data is visualized in the z-vorticity field in Figure 6.11. It should be noted that although Figure 6.11 appears to be two-dimensional, this is only a projection of three-dimensional data, such that the entire

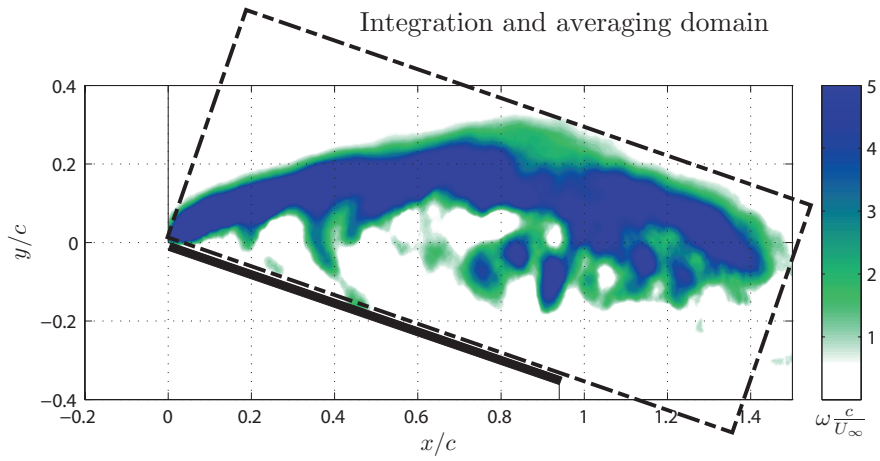

Figure 6.11: The three-dimensional vorticity field is shown here projected onto a single plane. Vorticity values below and upstream of the wing have been masked. The domain used to integrate circulation values and compute spanwise flow and circulation gradient values tabulated in Table 6.1 is shown as the dashed box.

velocity-gradient tensor and the gradient of circulation can be resolved directly. A single investigation window, indicated by the dashed box in Figure 6.11, was used as both an integration domain and as an averaging window in order to compute circulation transport properties. This large field of view was used to compute circulation, spanwise flow, and the circulation gradient, as tabulated in Table 6.1. Furthermore, the shear-layer feeding discussed in Section 6.5.1 is included for comparison.

Circulation is the first parameter tabulated in Table 6.1. Despite the shear-layer feeding being similar between the Monte Carlo simulation and the measured quantities, the model underestimates circulation. However, it can be observed that the proportion by which circulation is underestimated is almost identical to the quantity by which the circulation feeding is underestimated. The measured case exhibits approximately 16% higher circulation and 13% higher circulation feeding than the Monte Carlo simulation. Thus, in future work it may be possible to improve the presented

Table 6.1: Circulation, circulation transport, and shear layer properties for a flat plate delta wing are estimated with a low-cost Monte Carlo simulation. The results of that simulation are compared here to 4D-PTV measurements for the case of a non-slender flat-plate delta wing.

	Γ (m^2/s^2)	w (m/s)	Shear-layer feeding (m^2/s^2)	$\frac{\partial \Gamma}{\partial z}$ (m/s)	Residual (%)
Measured	0.220	0.33	0.431	1.19	9
Modelled	0.190	0.30	0.383	1.22	1.1

Monte Carlo method by including an estimate for the base pressure coefficient.

By running the simulation again using the empirical feeding rate of $\partial\Gamma/\partial t = 0.43\ m^2/s^2$ as an input parameter, we can estimate the sensitivity of the proposed model to the feeding rate, and therefore determine the value of improving circulation feeding models. Using this circulation feeding value, the modelled circulation is approximately 9% greater than the measured values, which is also equal to the residual in the measured case. The *residual* of the circulation balance, tabulated in the final column of Table 6.1, is defined as the difference between the circulation fed into the LEV through the leading-edge shear layer and the circulation leaving the domain due to vorticity advection. This difference is expressed as a percentage of the circulation fed into the LEV. For instance, the residual of the vorticity balance in the measured test case is 9%, meaning that 91% of the circulation that enters the domain in steady-state is advected out of the domain in the spanwise direction, validating the assumption of a advection-dominated circulation balance in Section 6.3. In the modelled case, the residual of 1% represents a small numerical error due to the discretization of mass into particles, as part of the Monte Carlo method. However, the larger 9% value measured on the delta wing is more significant, as it suggests that a proportion of circulation that enters the LEV through the leading-edge shear layer is not being advected downstream, due either to vorticity being tilted out of

the measurement plane, reducing the in-plane circulation measurement, or by vorticity annihilation from the surface of the profile. If this residual is due to vorticity annihilation, the magnitude of annihilation that we observe here is significantly less than that reported by Wojcik and Buchholz (2014). However, Wojcik and Buchholz (2014) also observed that vorticity annihilation decreased with increasing Reynolds number, and in turn their Reynolds numbers were approximately an order of magnitude smaller than in the current study. As the model proposed here is intended for extremely low-cost early estimates, such as for rapid parameter studies or flow control, this 9% error is within commonly accepted tolerance. Therefore, the proposed Monte Carlo simulation represents an extremely low-cost and versatile model, easily applied to unsteady problems and rotating wings.

6.6 Conclusions

In this study a model is proposed to predict the time-resolved circulation of an LEV in the presence of spanwise flow. This model is a Monte Carlo simulation of vorticity-containing mass advected along the span of the profile. *A priori* knowledge required to successfully implement this model is limited to the profile shape, profile kinematics, and free-stream velocity. This kinematic model frees the modeller from using empirical data on the shear-layer velocity or thickness, or circulation gradients in order to compute the circulation distribution.

This model is applied to the stationary LEV above a flat-plate delta wing, as a canonical case with which to validate the Monte Carlo simulations. The model for circulation feeding into the LEV is within 15% of values measured with high-speed PIV. Simply using the component of the free-stream velocity along the leading edge,

in this case $U_\infty/(2\sqrt{2})$, produced a spanwise flow very similar to that measured on the delta wing. This spanwise flow, in turn, advected a similar quantity of circulation along the span as a real delta wing, resulting in an estimate of circulation within 15% of measured values. The ratio between modelled and measured circulation was very similar to the ratio of modelled and measured circulation feeding. When the real feeding rate is applied to the modelled case, the predicted circulation is 9% abive the measured value, which is precisely the quantity of circulation annihilated or tilted out of the measurement plane in the physical case Furthermore, this improved circulation estimate validates each of the other assumptions made about circulation transport in Section 6.3. In particular, it is shown that circulation is indeed advected with vorticity-containing mass along the span of the profile, and in addition both vortex tilting and vorticity diffusion are minimal at higher Reynolds numbers, as tested here.

Approximately 9% of the circulation entering the flat-plate delta wing is not transported out of the LEV through circulation advection. As the Monte Carlo simulation neglected viscous diffusion, vorticity annihilation, and vortex tilting, this residual value may be difficult to account for without dramatically changing the modelling formulation. However, this 9% is also within common engineering tolerance for early-stage design tools, before applying high-fidelity methods at a higher cost later. As such, the proposed model provides an attractive and extremely low-cost platform for estimating the time- and spanwise-resolved circulation distribution within an LEV on planforms of complex shape and/or undergoing unsteady motion as found in biological and biomimetic swimming and flying.

6.7 Acknowledgements

The authors would like to thank the Natural Sciences and Engineering Research Council of Canada for partial funding in support of this work.

Chapter 7

Synthesis

Nature's flyers and swimmers exhibit graceful, forceful aerobatics and aquatic manoeuvres. Animals achieve such large lift coefficients, tight turning radii, and impressive acceleration through the skilful manipulation of vortices in the flow. Yet, while these observations are found in a substantial fraction of the studies cited by this thesis, the ultimate goal of robust, nimble and efficient biomimetic flying and swimming machines remains elusive. In that great tradition, the current thesis does not offer a breakthrough. However, in addition to their self-contained conclusions, the preceding chapters provide collective insight clustered around three themes: the use of profile kinematics and flexibility as a method of flow control; techniques for investigating such highly-separated three-dimensional flows; and the applications of biomimetic flow physics to areas outside of flying and swimming machines. These themes are discussed in more detail below, followed by an outlook and concluding remarks.

7.1 Wing Shape and Kinematics as Flow Control

As discussed in Chapter 1, some animals exploit flow control techniques familiar to aeronautical engineers and naval architects. For instance, the *dog-toothed* leading-edge of high-performance aircraft bears a strong resemblance to the manipulation of the alula in birds of prey. Meanwhile, the manipulation of profile kinematics and shape is well outside the scope of modern aviation. However, Chapters 2 and 3 showed that manipulating the profile motion itself can nevertheless be quite an effective flow control. In both studies this control amounted to a balance of circulation entering a vortex versus the amount leaving it. The rate of circulation entering a vortex was given as:

$$\frac{\partial \Gamma}{\partial t} \propto u_{\text{eff}}^2 \ , \tag{7.1}$$

similar to the rate of vortex growth in piston-cylinders found by Didden (1979). For a profile undergoing sinusoidal plunging $h = h_0 \sin(2\pi f t)$, this can be non-dimensionalized as:

$$\frac{\partial \Gamma}{\partial t} \frac{1}{U_\infty^2} \propto \frac{u_{\text{eff}}^2}{U_\infty^2} = \frac{(2\pi f h_0)^2 + U_\infty^2}{U_\infty^2} = \pi^2 St^2 + 1 \ , \tag{7.2}$$

meaning that an animal can change its stroke amplitude or frequency to increase or decrease its circulation generation. This of course fits in neatly with the findings of Baik et al. (2012) that Strouhal number dictates force generation, and the close relationship between formation number and stroke amplitude, as discussed in Chapter 1. Similarly, maximum growth of an LEV in a period of motion c^2/T is curiously

related to the integral of circulation generation over the period of motion:

$$\frac{c^2/T}{u_{\text{eff}}^2 T} \propto \frac{1}{\pi^2} k^2 \ , \tag{7.3}$$

which is once again in line with the observations in literature that the reduced frequency k dictates LEV growth and detachment in two-dimensional flows. Thus, even without considering any three-dimensionality, an animal already has a tremendous amount of control authority over vortex growth.

Once three-dimensional effects are considered, circulation can further be controlled through vorticity transport:

$$\frac{\partial \Gamma}{\partial t} = \overline{-w \frac{\partial \omega_z}{\partial z}} A \ . \tag{7.4}$$

Here, circulation can now be controlled by modulating spanwise flow w through profile sweep, as in Chapter 2 and Wong et al. (2013a), or through profile deformation, as in Chapter 3. Alternatively, it was found in Chapter 4 that the vorticity gradient can be controlled by varying the angle-of-attack gradient, which can be controlled through profile twist.

These studies examine a fraction of the available parameter space in biomimetic locomotion, and there is thus immense opportunity to continue investigations into the use of profile kinematics for circulation control. For instance, chordwise flexibility and profile twist can both alter circulation generation, while twist in particular can also modify the angle of attack to drive vorticity convection. Other methods of altering the balance of circulation have been identified as well, such as vorticity annihilation (see Wojcik and Buchholz (2014)) or downwash induced by the tip vortices (see Birch and Dickinson (2001)). These too may have biomimetic means of control yet to be

understood. The prospect of determining such methods requires a corresponding leap in measurement accuracy and resolution, which brings us to the following section.

7.2 Analysing Unsteady Separated Flows

Once there are scaling rules such as those laid out in Section 7.1, there is a desire to move on to developing low-cost predictive tools. Each of the Chapters 2, 3 and 4 determined scaling relationships for the convection of vorticity between rotation rate, profile flexibility and angle-of-attack gradient. While each of these studies gives insight into the flying and swimming strategies of animals, the models they present are scaling relationships, and therefore are not sufficient to be predictive engineering tools. One promising path forwards is to investigate vorticity transport as a function of mass transport, as opposed a function of kinematic parameters.

Chapters 2, 3 and 4 each investigated vorticity transport utilizing velocimetry data produced via particle-tracking methods, both traditional 3D-PTV and *Shake-the-Box*. For Chapter 2 in particular, 3D-PTV was found to be extremely robust due its tolerance for low illumination when studying large volumes. Later on, *Shake-the-Box* also allowed for the resolution of the entire velocity gradient tensor in a single measurement realization, limiting the influence of run-to-run variability in the analysis (for instance due to ensemble averaging). However, in each of these cases, circulation transport was then studied in the familiar Eulerian frame of reference, discarding the inherent mass transport information provided by PTV. The desire to retain mass-transport inspired the vorticity-correction method presented in Chapter 5. Studying the relationship between vorticity transport and mass transport is very promising, as a simple relationship between the two would allow for the determination of the

dynamic redistribution of circulation in a flow from bulk velocities. These velocities in turn can be determined from profile kinematics and shape much more easily than attempting to estimate the vorticity field directly.

These ideas were applied directly in Chapter 6, where a low-cost model for the circulation balance on a delta wing was proposed and validated. Such a model would not be possible without both high-quality Lagrangian and Eulerian information in order to validate the vorticity transport model. The use of these analysis techniques on a delta wing demonstrates one example of the extensibility of these vorticity transport models to non-biomimetic applications, which is described in more detail in the following section.

7.3 Applications Outside of Biomimetic Locomotion

Vortex-dominated flows are ubiquitous throughout aerodynamics and hydrodynamics, and are in no way limited to bio-inspired flows. The turbine case studied in Chapter 4 is an excellent example: a wind turbine subject to a gust experiences dynamic stall just as a flapping wing does, and is subject to similarly strong rotational accelerations. Utilizing blade-element methods where individual nodes do not communicate mass, momentum, or circulation transport will thus generate erroneous results. Chapter 4 demonstrates not only that typical gust profiles exposed to a turbine would result in similar LEV formation to that on a natural flyer, but that the spanwise flow configuration typical to wind turbines produces the largest, most unsteady loads. The same technique could be applied to rotor craft, which experience similar rotational accelerations and similar dynamic stall behaviour.

The above analysis also applies to delta wings, as demonstrated in Chapter 6.

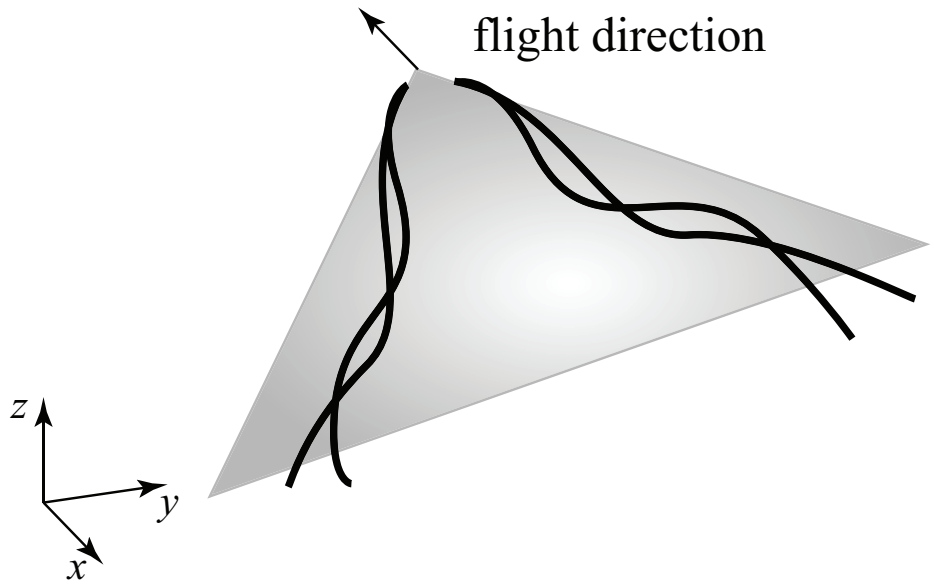

Figure 7.1: A delta wing exhibits a stationary LEV, similar to the flapping propulsors of natural swimmers and flyers. This LEV must also satisfy the conservation of mass and circulation, and therefore can be modelled using similar techniques to those developed for biomimetic propulsion.

Despite the absence of rotation, delta wings exhibit the same stably attached LEV as in biological flight, as shown in Figure 7.1. A significant fraction of the analysis on LEV stabilisation on biological flyers has focused on rotation, as described in Section 1.1.2. Yet, the LEV must satisfy the exact same conditions on a delta wing as on an insect wing: mass and circulation must be conserved.

7.4 Outlook

We are naturally left with new questions as we make progress with the old ones. In particular, the focus of this thesis has been on a limited subset of three-dimensional flows where the only significant additions to the two-dimensional case are spanwise flow and angle-of-attack gradients. Extending the relationships for vortex growth

and circulation convection derived in earlier chapters to true low-cost models, those appropriate for design work, is an obvious goal for future researchers. This work will involve investigations on finite wings to determine how the above relationships change in the presence of strong tip vortices. In the context of flexibility, this work also limited itself to investigating spanwise bending. Of course, actual propulsors also exhibit both twist and chordwise flexibility. Chordwise flexibility in particular is very pronounced in aquatic mammals and other swimmers.

Swimming and flying animals have developed their manoeuvring ability due to the evolutionary pressure from their environment, and gust loading and riverine unsteadiness are both in need of greater investigation. A gust encounter, such as passing near a roller embedded in the flow, can be abstracted as a phase-lag in angle-of-attack between the leading and trailing-edges of the profile, as demonstrated by Wong et al. (2013b). As such, it may be possible to model gusts through dynamic cambering. A comparison of dynamic cambering effects from a gust encounter to that of chordwise flexibility may be very fruitful, considering the need for further investigation in both cases.

7.5 Closing remarks

More than a century ago the form and function of bird wings were informing the first powered flight. Today, biological swimmers and flyers are far from relinquishing all of their secrets. While this thesis was narrow in scope, it was conducted with the knowledge that a problem like biomimetic locomotion will only yield through many small incremental steps.

This work has produced scaling relationships for LEV growth and detachment,

proposed a method by which animals use their profile kinematics as a form of flow control, and developed measurement techniques that may be useful to future investigation. A model based on these scaling relationships has also been applied to a non-biomimetic application, a delta wing, as a demonstration of its robustness. It is hoped that these contributions both advance our understanding of biological behaviour, and provide tools necessary for improving engineered vehicles and machinery going forward.

Bibliography

Anders, J. B. (2000). "Biomimetic Flow Control". In: *18th AIAA Applied Aerodynamic Conference, Denver, CO, USA.*

Baik, Y. and L. Bernal (2012). "Experimental study of pitching and plunging airfoils at low Reynolds numbers". In: *Experiments in Fluids* 53, pp. 1979–1992.

Baik, Y., L. Bernal, K. Granlund, and M. Ol (2012). "Unsteady force generation and vortex dynamics of pitching and plunging aerofoils". In: *Journal of Fluid Mechanics* 709, pp. 37–68.

Bansmer, S. and R. Radespiel (2012). "Validation of unsteady Reynolds-Averaged Navier-Stokes simulations on three-dimensional flapping wings". In: *AIAA Journal* 50.1, pp. 190–202.

Beal, D. N., F. S. Hover, M. S. Triantafyllou, J. c. Liao, and G. V. Lauder (2006). "Passive propulsion in vortex wakes". In: *Journal of Fluid Mechanics* 549, pp. 384–402.

Beem, H., D. Rival, and M. Triantafyllou (2012). "On the stabilization of leading-edge vortices with spanwise flow". In: *Experiments in Fluids* 51, pp. 511–517.

Birch, J., W. Dickson, and M. Dickinson (2004). "Force Production and Flow Structure of the Leading Edge Vortex on Flapping Wings at High and Low Reynolds Numbers". In: *Journal of Experimental Biology* 207, pp. 1063–1072.

Birch, J. M. and M. H. Dickinson (2001). "Spanwise Flow and the Attachment of the Leading-Edge Vortex on Insect Wings". In: *Nature* 412, pp. 729–733.

Bomphrey, R. J., N. J. Lawson, N. J. Harding, G. K. Taylor, and T. A. L. (2005). "The aerodynamics of Manduca sexta: digital particle image velocimetry analysis of the leading-edge vortex". In: *The Journal of Experimental Biology* 208, pp. 1079–1094.

Borazjani, I. and M. Daghooghi (2013). "The fish tail motion forms an attached leading edge vortex". In: *Proceedings of the Royal Society B* 280, p. 20122071.

Bowlin, M. S. and D. W. Winkler (2004). "Natural variation in flight performance is rrelate to timing of breeding in tree swallows Tachycineta bicolor in New York". In: *The Auk: Ornithological Advances* 121.2, pp. 345–353.

Brachet, M. E., D. I. Meiron, S. A. Orszag, B. G. Nickel, R. H. Morf, and U. Frisch (1983). "Small-scale structure of the TaylorGreen vortex". In: *Journal of Fluid Mechanics* 130, pp. 411–452.

Brunton, S. L. and C. W. Rowley (2010). "Fast Computation of FTLE Fields for Unsteady Flows: A Comparison of Methods". In: *Chaos* 20, pp. 1–12.

Bunin, G. A., G. François, and D. Bonvin (2013). "From discrete measurements to bounded gradient estimates: A look at some regularizing structures". In: *Industrial & Engineering Chemistry Research* 52.35, pp. 12500–12513.

Burton, T., D. Sharpe, N. Jenkins, and E. Bossanyi (2001). *Wind Energy Handbook*. Wiley.

Canuto, C. G., M. Y. Hussaini, A. M. Quarteroni, and T. A. Zang (2007). *Spectral Methods: Evolution to Complex Geometries and Applications to Fluid Dynamics (Scientific Computation)*. Springer-Verlag New York, Inc.

Carruthers, A. C., A. L. R. Thomas, and G. K. Taylor (2007). "Automatic aeroelastic devices in the wings of a steppe eagle Aquila nipalensis". In: *Journal of Experimental Biology* 210.23, pp. 4136–4149.

Cheng, B., S. P. Sane, G. Barbera, D. R. Troolin, T. Strand, and X. Deng (2013). "Three-dimensional flow visualization and vorticity dynamics in revolving wings". In: *Experiments in Fluids* 54.1, pp. 1–12.

Clark, C. J. (2009). "Courtship dives of Annas hummingbird offer insights into flight performance limits". In: *Proceedings of the Royal Society B* 276, pp. 3047–3052.

Cleaver, D., D. E. Calderon, Z. Wang, and I. Gursul (2016). "Lift enhancement through flexibility of plunging wings and low Reynolds numbers". In: *Journal of Fluids and Structures* 64, pp. 27–45.

Cleaver, D. J., I. Gursul, D. E. Calderon, and Z. Wang (2014). "Thrust enhancement due to flexible trailing-edge of plunging foils". In: *Journal of Fluids and Structures* 51, pp. 401–412.

Combes, S. A. and T. L. Daniel (2003). "Into thin air: contributions of aerodynamic and inertial-elastic forces to wing bending in the hawkmoth Manduca sexta". In: *Journal of Experimental Biology* 206, pp. 2999–3006.

Conte, J., Y. Modarres-Sadeghi, M. Watts, F. Hover, and M. Triantafyllou (2010). "A fast-starting mechanical fish that accelerates at 40ms^{-2}". In: *Bioinspiration & Biomimetics* 5, pp. 1–9.

Correa, C. D., R. Hero, and K.-L. Ma (2011). "A comparison of gradient estimation methods for volume rendering on unstructured meshes". In: *Visualization and Computer Graphics, IEEE Transactions on* 17.3, pp. 305–319.

Dabiri, J. O. (2009). "Optimal Vortex Formation as a Unifying Principle in Biological Propulsion". In: *Annual Revew of Fluid Mechanics* 41, pp. 17–33.

Dial, K. P. (1992). "Avian forelimb muscles and nonsteady flight: Can birds fly without using the muscles in their wings?" In: *The Auk: Ornithological Advances*, pp. 874–885.

Didden, N. (1979). "On the Formation of Vortex Rings: Rolling-up and Production of Circulation". In: *Journal of Applied Mathematics and Physics* 30, pp. 101–116.

Doyle, C. E., J. J. Bird, T. A. Isom, J. C. Kallman, D. F. Bareiss, D. J. Dunlop, R. J. King, J. J. Abbott, and M. A. Minor (2012). "An Avian-Inspired Passive Mechanism for Quadrotor Perching". In: *IEEE/ASME Transactions on Mechatronics* 18, pp. 506–517.

Du, Z. and M. Selig (1998). "A 3-D stall-delay model for horizontal axis wind turbines performance prediction". In: *36th AIAA Aerospace Sciences Meeting and Exhibit, Reno, USA*. Vol. 98. 0021.

Ellington, C. P., C. van den Berg, A. P. Willmott, and A. L. R. Thomas (1996). "Leading-edge vortices in insect flight". In: *Nature* 384.6610, pp. 626–630.

Eloy, C. (2013). "On the best design for undulatory swimming". In: *Journal of Fluid Mechanics* 717, pp. 48–89.

Elsinga, G. E., F. Scarano, B. Wieneke, and B. W. van Oudheusden (2006). "Tomographic Particle Image Velocimetry". In: *Experiments in Fluids* 41, pp. 933–947.

Eslam Panah, A., J. M. Akkala, and J. H. J. Buchholz (2015). "Vorticity transport and the leading-edge vortex of a plunging airfoil". In: *Experiments in Fluids* 56, p. 160.

Fernando, J. N. and D. E. Rival (2016). "Reynolds-number scaling of vortex pinch-off on low-aspect-ratio propulsors". In: *Journal of Fluid Mechanics* 799.

Fisher, A., S. Ravi, S. Watkins, J. Watmuff, C. Wang, H. Liu, and P. Petersen (2016). "The gust-mitigating potential of flapping wings". In: *Bioinspiration and Biomimetics* 11, p. 046010.

Flammang, B. E., G. V. Lauder, D. R. Troolin, and T. Strand (2011). "Volumetric imaging of shark tail hydrodynamics reveals a three-dimensional dual-ring vortex wake structure". In: *Proceedings of the Royal Society B* 278, pp. 3670–3678. ISSN: 0889-9746.

Garmann, D. J., M. Visbal, and P. D. Orkwis (2013). "Three-dimensional flow structure and aerodynamic loading on a revolving wing". In: *Physics of Fluids* 25, p. 034101.

Gesemann, S., F. Huhn, D. Schanz, and A. Schröder (2016). "From noisy particle tracks to velocity, acceleration and pressure fields using B-splines and penalties." In: *18th international symposium on applications of laser and imaging techniques to fluid mechanics, Lisbon, Portugal.*

Gharib, M., E. Rambod, and K. Shariff (1998). "A Universal Time Scale for Vortex Ring Formation". In: *Journal of Fluid Mechanics* 360, pp. 121–140.

Glauert, H. (1935). "Aerodynamic theory". In: ed. by W. Durand. 3rd ed. Vol. IV. New York: Springer.

Graftieaux, L., M. Michard, and N. Grosjean (2001). "Combining PIV, POD and Vortex Identification Algorithms for the Study of Turbulent Swirling Flows". In: *Measurement Science and Technology* 12, pp. 1422–1429.

Harbig, R. R., J. Sheridan, and M. C. Thompson (2013). "Reynolds Number and Aspect Ratio Effects on the Leading-Edge Vortex for Rotating Insect Wing Planforms". In: *Journal of Fluid Mechanics* 717, pp. 166–192.

Hartloper, C. and D. Rival (2013). "Vortex development on pitching plates with lunate and truncate planforms". In: *Journal of Fluid Mechanics* 732, pp. 332–344.

Hartloper, C., M. Kinzel, and D. E. Rival (2013). "On the Competition between Leading-Edge and Tip-Vortex Growth for a Pitching Plate". In: *Experiments in Fluids* 54, p. 1447.

Hawkes, E. W. and D. Lentink (2016). "Fruit fly scale robots can hover longer with flapping wings than with spinning wings". In: *Journal of the Royal Society Interface* 13, p. 20160730.

Heathcote, S., Z. Wang, and I. Gursul (2007). "Effect of spanwise flexibility on flapping wing propulsion". In: *Journal of Fluids and Structures* 24, pp. 183–199.

Hemati, M. S., J. D. Eldredge, and J. L. Speyer (2014). "Improving Vortex Models via Optimal Control Theory". In: *Journal of Fluids and Structures* 49, pp. 91–111.

Jain, M. V., J. G. Wong, and D. E. Rival (2015). "A Model of Fluid-Structure-Interaction for Impulsively Started Spanwise-Flexible Wings". In: *Journal of Fluids and Structures* 54, pp. 466–478.

Jardin, T. and L. David (2014). "Spanwise gradients in flow speed help stabilize leading-edge vortices on revolving wings". In: *Physical Review E* 90, p. 013011.

Jeon, Y. J., L. Chatellier, and L. David (2014). "Fluid trajectory evaluation based on an ensemble-averaged cross-correlation in time-resolved PIV". In: *Experiments in Fluids* 55, p. 1766.

Jones, A. R. and H. Babinsky (2011). "Reynolds number effects on leading edge vortex development on a waving wing". In: *Experiments in Fluids* 51, pp. 197–210.

Jones, A. R., C. W. P. Ford, and H. Babinsky (2012). "Three-Dimensional Effects on Sliding and Waving Wings". In: *Journal of Aircraft* 48.2, pp. 633–643.

Kähler, C. J., S. Scharnowski, and C. Cierpka (2012). "On the Uncertainty of Digital PIV and PTV Near Walls". In: *Experiments in Fluids* 52.6, pp. 1641–1656.

Kang, C.-K. and W. Shyy (2014). "Analytical model for instantaneous lift and shape deformation of an insect-scale flapping wing in hover". In: *Journal of the Royal Society Interface* 11, p. 20140933.

Kang, C.-K., H. Aono, C. E. S Cesnik, and W. Shyy (2011). "Effects of Flexibility on the Aerodynamic Performance of Flapping Wings". In: *Journal of Fluid Mechanics* 689, pp. 32–74.

Karàsek, M., A. J. Koopmans, S. F. Armanini, B. D. W. Remes, and G. C. H. E. de Croon (2016). "Free flight force estimation of a 23.5 g flapping wing MAV using an on-board IMU". In: *IEEE/RSJ International Conference on Intelligent Robots and Systems, Daejeon, South Korea.*

Kim, J. and P. Moin (1985). "Application of a fractional-step method to incompressible Navier-Stokes equations". In: *Journal of computational physics* 59(2), pp. 308–323.

Kriegseis, J., M. Kinzel, and D. E. Rival (2013). "On the persistence of memory: do initial conditions impact vortex formation?" In: *Journal of Fluid Mechanics* 736, pp. 91–106.

Lee, S. J., E. J. Lee, and M. H. Sohn (2014). "Mechanism of autorotation flight of maple samaras". In: *Experiments in Fluids* 55:1718.

Lentink, D. and M. H. Dickinson (2009a). "Biofluiddynamic scaling of flapping, spinning and translating fins and wings". In: *Journal of Experimental Biology* 212, pp. 2691–2704.

— (2009b). "Rotational accelerations stabilize leading edge vortices on revolving fly wings". In: *Journal of Experimental Biology* 212, pp. 2705–2719.

Lentink, D., W. B. Dickson, J. L. van Leeuwen, and M. H. Dickinson (2009). "Leading-Edge Vortices Elevate Lift of Autorotating Plant Seeds". In: *Science* 324, pp. 1438–1440.

Levy, Y., D. Degani, and S. Arnan (1990). "Graphical visualization of vortical flows by means of helicity". In: *AIAA Journal* 28.8, pp. 1347–1352.

Liao, J. C., D. N. Beal, G. V. Lauder, and M. S. Triantafyllou (2003). "Fish exploiting vortices decreas muscle activity". In: *Science* 302, pp. 1566–1569.

Lilienthal, O. (1889). *Der Vogelflug als Grundlage der Fliegekunst*. Berlin: R. Gaertner Verlagsbuchhandlung.

Lissaman, P. B. S. (1983). "Low-Reynolds-Number Airfoils". In: *Annual Revew of Fluid Mechanics* 15, pp. 223–239.

Lucas, K. N., N. Johnson, W. T. Beaulieu, E. Cathcard, G. Tirrell, S. P. Colin, B. J. Gemmell, J. O. Dabiri, and J. H. Costello (2014). "Bending rules for animal propulsion". In: *Nature Communications* 5, p. 3293.

MacIver, M. A., E. Fontaine, and J. W. Burdick (2004). "Designing Future Underwater Vehicles: Principles and Mechanisms of the Weakly Electric Fish". In: *IEEE Journal of Oceanic Engineering* 29, pp. 651–659.

Maurer, B. A., J. H. Brown, T. Dayan, B. J. Enquist, S. M. Ernest, E. A. Handly, J. P. Haskell, D. Jablonski, K. E. Jones, D. M. Kaufman, S. K. Lyons, K. J.

Niklas, W. P. Porter, K. Roy, F. A. Smith, B. Tiffney, and M. R. Willig (2004). "Similarities in Body Size Distributions of Small-Bodied Flying Vertebrates". In: *Evolutionary Ecology Research* 6, pp. 783–797.

Maxworthy, T. (2007). "The formation and maintenance of a leading-edge vortex during the forward motion of an animal wing". In: *Journal of Fluid Mechanics* 587, pp. 471–475.

Meyer, H. T. H., M Eriksson, and R. C. Maggio (2001). "Gradient Estimation from Irregularly Spaced Data Sets". In: *Mathematical Geology* 33.3, pp. 693–717.

Milano, M. and M. Gharib (2005). "Uncovering the Physics of Flapping Flat Plates with Artificial Evolution". In: *Journal of Fluid Mechanics* 534, pp. 403–409.

Mohamed, A., S. Watkins, M. Abdulrahim, K. Massey, and R. Sabatini (2014). "Fixed-wing MAV attitude stability in atmospheric turbulencePart 2: Investigating biologically-inspired sensors". In: *Progress in Aerospace Sciences* 71, pp. 1–13.

Moore, J., R. Cory, and R. Tedrake (2014). "Robust post-stall perching with a simple fixed-wing glider using LQR-Trees". In: *Bioinspiration and Biomimetics* 9.2, p. 025013.

Neeteson, N. J. and D. E. Rival (2015). "Pressure-field extraction on unstructured flow data using a Voronoi tessellation-based networking alogrithm: a proof-of-principle study". In: *Experiments in Fluids* 56.44, p. 44.

Neeteson, N. J., S. Bhattacharya, D. E. Rival, D. Michaelis, D. Schanz, and A. Schröder (2016). "Pressure-field extraction from Lagrangian flow measurements: first experiences with 4D-PTV data". In: *Experiments in Fluids* 57, p. 102.

Nudds, R. L., G. K. Taylor, and A. L. R. Thomas (2004). "Tuning of Strouhal number for high propulsive efficiency accurately predictes how wingbeat frequency and stroke amplitude relate and scale with size and flight speed in birds". In: *Proceedings of The Royal Society: B* 271, pp. 2071–2076.

Ol, M. V. and M. Gharib (2003). "Leading-Edge Vortex Structure of Nonslender Delta Wings at Low Reynolds Numbers". In: *AIAA Journal* 41, pp. 16–26.

Ol, M. V., L. Bernal, C.-K. Kang, and W. Shyy (2009). "Shallow and deep dynamic stall for flapping low Reynolds number airfoils". In: *Experiments in Fluids* 46, pp. 883–901.

Onoue, K. and K. S. Breuer (2016). "Vortex formation and shedding from a cyber-physical pitching plate". In: *Journal of Fluid Mechanics* 793, pp. 229–247.

Orszag, S. A. (1969). "Numerical methods for the simulation of turbulence". In: *Physics of Fluids* 12(12), pp. II–250.

— (1971). "On the elimination of aliasing in finite-difference schemes by filtering high-wavenumber components". In: *Journal of the Atmospheric sciences* 28(6), p. 1074.

— (1972). "Comparison of pseudospectral and spectral approximation". In: *Studies in Applied Mathematics* 51(3), pp. 253–259.

Ozen, C. and D. Rockwell (2012). "Three-dimensional vortex structure on a rotating wing". In: *Journal of Fluid Mechanics* 707, pp. 541–550.

Pitt Ford, C. W. and H. Babinsky (2013). "Lift and the Leading Edge Vortex". In: *Journal of Fluid Mechanics* 720, pp. 280–313.

Poelma, C., W. B. Dickson, and M. H. Dickinson (2006). "Time-resolved reconstruction of the full velocity field around a dynamically-scaled flapping wing". In: *Experiments in Fluids* 41, pp. 213–225.

Polhamus, E. C. (1966). *A Concept of the Vortex Lift of Sharp-Edge Delta Wings Based on a Leading Edge Suction Analogy*. Tech. rep. NASA.

Raben, S. G., S. D. Ross, and P. P. Vlachos (2014). "Computation of Finite Time Lyapunov Exponents from Time Resolved Particle Image Velocimetry Data". In: *Experiments in Fluids*.

Raffel, M., C. Willert, S. Wereley, and J. Kompenhans (2007). *Particle image velocimetry: a practical guide*. 2nd ed. Springer, pp. 164–176.

Ramesh, K., A. Gopalarathnam, K. Granlund, M. V. Ol, and J. R. Edwards (2014). "Discrete-vortex method with novel shedding criterion for unsteady aerofoil flows with intermittent leading-edge vortex shedding". In: *Journal of Fluid Mechanics* 751, pp. 500–538.

Rival, D. and C. Tropea (2010). "Characteristics of Pitching and Plunging Airfoils Under Dynamic-Stall Conditions". In: *Journal of Aircraft* 47 (1), pp. 80–86.

Rival, D. E., T. Prangemeier, and C. Tropea (2009). "The Influence of Airfoil Kinematics on the Formation of Leading-Edge Vortices in Bio-Inspired Flight". In: *Experiments in Fluids* 46, pp. 823–833.

Rival, D. E., J. Kriegseis, P. Schaub, A. Widmann, and C. Tropea (2014). "Characteristic Length Scales for Vortex Detachment on Plunging Profiles with Varying Leading-Edge Geometry". In: *Experiments in Fluids* 55.1, pp. 1–8.

Rockwood, M. P., K. Taira, and M. A. Green (2016). "Detecting Vortex Formation and Shedding in Cylinder Wakes Using Lagrangian Coherent Structures". In: *AIAA Journal* 55, pp. 15–23.

Ronsten, G. (1992). "Static Pressure Measurements on a Rotating and a Non-Rotating 2.375 m Wind Turbine Blade. Comparison with 2D Calculations". In: *Journal of Wind Engineering and Industrial Aerodynamics* 39, pp. 105–118.

Roshko, A. (1954). *On the drag and shedding frequency of two-dimensional bluff bodies.* Tech. rep. National Advisory Comittee for Aeronautics.

Sane, S. P. (2003). "The aerodynamics of insect flight". In: *Journal of Experimental Biology* 206, pp. 4191–4208.

Sane, S. P. and M. H. Dickinson (2002). "The aerodynamic effects of wing rotation and a revised quasi-steady model of flapping flight". In: *Journal of Experimental Biology* 205, pp. 1087–1096.

Scarano, F. and P. Moore (2012). "An advection-based model to increase the temporal resolution of PIV time series". In: *Experiments in Fluids* 52, pp. 919–933.

Schanz, D., S. Gesemann, and A. Schröder (2016). "Shake-The-Box: Lagrangian particle tracking at high particle image densities". In: *Experiments in Fluids* 57:70.

Schneiders, J., P. Singh, and F. Scarano (2016). "Instantaneous Flow Reconstruction from Particle Trajectories with Vortex-in-Cell". In: *18th International Symposium on the Application of Laser and Imaging Techniques to Fluid Mechancs, Lisbon, Portugal.*

Schneiders, J. and F. Scarano (2016). "Dense velocity reconstruction from tomographic PTV with material derivatives". In: *Experiments in Fluids* 57, p. 139.

Shadden, S. C., J. O. Dabiri, and J. E. Marsden (2006). "Lagrangian analysis of fluid transport in empirical vortex ring flows". In: *Physics of Fluids* 18.4, 047105, p. 047105.

Shelton, R. M., B. E. Jackson, and T. L. Hedrick (2014). "The mechanics and behavior of cliff swallows during tandem flights". In: *Journal of Experimental Biology* 217, pp. 2717–2725.

Shipley, D. E., M. S. Miller, and M. Robinson (1995). *Dynamic stall occurrence on a horizontal axis wind turbine blade*. Tech. rep. National Renewable Energy Laboratory.

Stingu, E. and F. L. Lewis (2009). "A Hardware Platform for Research in Helicopter UAV Control". In: *Journal of Intelligent and Robotic Systems* 54, pp. 387–406.

Taylor, G. I. and A. E. Green (1937). "Mechanism of the production of small eddies from large ones". In: *Proceedings of the Royal Society of London. Series A, Mathematical and Physical Sciences* 158.895, pp. 499–521.

Taylor, G. K., R. L. Nudds, and A. Thomas (2003). "Flying and swimming animals cruise at a Strouhal number tuned for high power efficiency". In: *Nature* 425, pp. 707–710.

Tennekes, H. (2009). *The Simple Science of Flight*. Cambridge, MA: The MIT Press.

Tobalske, B. W. and K. P. Dial (1996). "Flight kinematics of black-billed magpies and pigeons over a wide range of speeds". In: *Journal of Experimental Biology* 199, pp. 263–280.

Tobalske, B. W., D. L. Altshuler, and D. R. Powers (2004). "Take-off mechanics in hummingbirds (Trochilidae)". In: *Journal of Experimental Biology* 207.8, pp. 1345–1352.

Torres, G. E. and T. J. Mueller (2004). "Low-Aspect-Ratio Wing Aerodynamics at Low Reynolds Numbers". In: *AIAA Journal* 42, pp. 865–873.

Triantafyllou, M. S., G. S. Triantafyllou, and R. Gopalkrishnan (1991). "Wake mechanics for thrust generation in oscillating foils". In: *Physics of Fluids A* 3, pp. 2835–2838.

Usherwood, J. and C. Ellington (2002). "The aerodynamics of revolving wings: I. Model hawkmoth wings". In: *Journal of Experimental Biology* 205, pp. 1547–1564.

Videler, J. (2005). *Avian flight*. New York: Oxford University Press.

Videler, J. J., E. J. Stamhuis, and G. D. E. Povel (2004). "Leading-Edge Vortex Lift Swifts". In: *Science* 306, pp. 1960–1962.

Wächter, M., M. Hölling, P. Milan, and P. Joachim (2011). "Wind Energy and the Turbulent Nature of the Atmospheric Boundary Layer". In: *AIAA 2011-3299; 6th AIAA Theoretical Fluid Mechanics Conference; Honolulu, Hawaii, USA*.

Weymouth, G. D., V. Subramaniam, and M. S. Triantafyllou (2015). "Ultra-fast escape maneuver of an octopus-inspired robot". In: *Bioinspiration and Biomimetics* 10, p. 016016.

White, F. M. (1999). *Fluid Mechanics*. 4th ed. New York: McGraw-Hill.

Widmann, A. and C. Tropea (2015). "Parameter influencing vortex growth and detachment on unsteady aerodynamic profiles". In: *Journal of Fluid Mechanics* 773, pp. 432–459.

Wojcik, C. J. and J. H. J. Buchholz (2014). "Vorticity transport in the leading-edge vortex on a rotating blade". In: *Journal of Fluid Mechanics* 743, pp. 249–261.

Wolf, M., M. Holzner, D. Krug, B. Lüthi, W. Kinzelbach, and A. Tsinober (2013). "Effects of mean shear on the local turbulent entrainment process". In: *Journal of Fluid Mechanics* 731, pp. 95–116.

Wong, J. G. and D. E. Rival (2015). "Determining the Relative Stability of Leading-Edge Vortices on Nominally Two-Dimensional Flapping Profiles". In: *Journal of Fluid Mechanics* 766, pp. 611–625.

Wong, J. G., J. Kriegseis, and D. E. Rival (2013a). "An investigation into vortex growth and stabilization for two-dimensional plunging and flapping plates with varying sweep". In: *Journal of Fluids and Structures* 43, pp. 231–243.

Wong, J. G., A. Mohebbian, J. Kriegseis, and D. E. Rival (2013b). "Rapid flow separation for transient inflow conditions versus accelerating bodies: an investigation into their equivalency". In: *Journal of Fluids and Structures* 40, pp. 257–268.

Worcester, S. E. (1996). "The scaling of the size and stiffness of primary flight feathers". In: *Journal of the Zoological Society of London* 239, pp. 609–624.

Young, J., S. M. Walker, R. J. Bomphrey, G. K. Taylor, and A. L. R. Thomas (2009). "Details of Insect Wing Design and Deformation Enhance Aerodynamic Function and Flight Efficiency". In: *Science* 325.5947, pp. 1549–1552.

Appendix A

The non-dimensionalization of Euler-Bernoulli beam theory and typical examples

The key non-dimensional parameters governing flapping-wing fluid-structure interaction were outlined by Kang et al. (2011). These parameters are as follows:

$Re = \rho U c/\mu$	Reynolds number,
$AR = R/c$	Aspect ratio,
$\rho^* = \rho_s/\rho$	Density ratio,
$\delta^* = \delta/c$	Thickness ratio,
$k = \pi f c/U$	Reduced frequency,
$St = h_0 k/\pi c$	Strouhal number,
$\Pi_1 = E\delta^{*3}/(12\rho U^2)$	Effective stiffness, and
$C_F = F/(\frac{1}{2}\rho U^2 c^2 AR)$	Force coefficient.

Many of the above terms are either standard aerodynamic parameters of Reynolds number Re, reduced frequency k, Strouhal number St, aspect ratio AR, and force coefficient C_F, or geometric parameters of chord c, span R, and thickness δ. However, the effective stiffness and density ratio must be recovered from the non-dimensionalization

of the Euler-Bernoulli Equation:

$$EI\frac{\partial^4 h}{\partial z^4} + m\frac{\partial^2 h}{\partial t^2} = C_F \tfrac{1}{2}\rho U^2 c \ . \tag{A.1}$$

Expanding the second moment of area I and linear density m, and dividing through by the dynamic pressure gives:

$$2\frac{E\delta^3}{12\rho U^2}\frac{\partial^4 h}{\partial z^4} + 2\frac{\rho_s}{\rho}\frac{\delta}{U^2}\frac{\partial^2 h}{\partial t^2} = C_F \ . \tag{A.2}$$

We can then make the following set of substitutions:

$$\begin{aligned} h &= h^* c \ , \\ \delta &= \delta^* c \ , \\ \tfrac{\partial}{\partial t} &= \tfrac{\partial}{\partial t^*} f \ , and \\ \tfrac{\partial}{\partial z} &= \tfrac{\partial}{\partial z^*}\tfrac{1}{R} \ , \end{aligned} \tag{A.3}$$

where h^*, t^*, and z^* are the non-dimensional versions of h, t and z, respectively. The beam equation now takes the following form:

$$2\frac{E\delta^{*3}}{12\rho U^2}\left(\frac{c^4}{R^4}\right)\frac{\partial^4 h^*}{\partial z^{*4}} + 2\frac{\rho_s}{\rho}\delta^*\left(\frac{\pi^2 f^2 c^2}{U^2}\right)\frac{1}{\pi^2}\frac{\partial^2 h^*}{\partial t^{*2}} = C_F \ . \tag{A.4}$$

As the effective stiffness Π_1 and the density ratio ρ^* are both now apparent, along with the reduced frequency k and aspect ratio AR, we can use the definitions of those

terms to clean up the non-dimensional Euler-Bernoulli equation:

$$\frac{2\Pi_1}{AR^4}\frac{\partial^4 h^*}{\partial z^{*4}} + 2\rho^*\delta^*\left(\frac{k}{\pi}\right)^2\frac{\partial^2 h^*}{\partial t^{*2}} = C_F(z,t)\ . \tag{A.5}$$

The coefficients in the above equation varies from the one presented by Kang et al. (2011) by the way in which the distributed force was defined, however the two are functionally identical.

Both the physical and dimensionless structural parameters for several insect species are presented in Table A.1. The stiffness EI, chord c, and span R are taken from Combes and Daniel (2003). Reference velocities are taken from the 'Great Flight Diagram' of Tennekes (2009), averaged with respect to insect order. There is no publication of the variation of thickness ratio with species, however Usherwood and Ellington (2002) give a general approximation of 1.6%, while Kang and Shyy (2014) give 2%. A value of 1.6% was used in the generation of the table below. A single density of $\rho_s = 1200\frac{kg}{m^3}$ was also used, as given by Combes and Daniel (2003), giving a uniform density ratio of $\rho^* = 1000$.

No similar table could be produced for either birds or aquatic animals. While some data on the flexural stiffness of flight feathers is available, notably by Worcester (1996) covering a broad range of bird sizes, there is not sufficient data to compute dimensionless parameters. Appropriate data for fish or cetaceans is similarly unavailable.

Table A.1: Structural properties of several insect species, organized by order: dragonflies, lacewings, bees and wasps, flies, and butterflies and moths.

Order	Name: Genus	Name: Common name	EI (Nm^2)	c (m)	R (m)	U_{ref} (ms^{-1})	Π_1	Re	AR	k
Odonata	Aeshna	Hawker dragonfly	1.13×10^{-4}	1.09×10^{-2}	4.28×10^{-2}	2.91	3.32	1.90×10^{3}	3.93	0.249
	Pachydiplax	Blue dasher dragonfly	3.91×10^{-5}	7.60×10^{-3}	3.16×10^{-2}		3.85	1.33×10^{3}	4.16	0.211
	Lestes	Emerald damselfly	1.04×10^{-5}	4.80×10^{-3}	2.34×10^{-2}		3.43	8.38×10^{2}	4.88	0.169
	Ischnura	Forktail damselfly	8.74×10^{-6}	4.20×10^{-3}	1.99×10^{-2}		5.48	7.33×10^{2}	4.74	-
Neuroptera	Hemerobius	Brown lacewing	6.70×10^{-7}	3.50×10^{-3}	9.00×10^{-3}	1.85	24.7	3.90×10^{2}	2.57	-
Hymenoptera	Pepsis	Tarantula hawk	1.64×10^{-5}	6.60×10^{-3}	2.20×10^{-2}	6.83	1.25	2.71×10^{3}	3.33	-
	Sceliphron	Mud dauber wasp	3.03×10^{-6}	3.70×10^{-3}	1.38×10^{-2}		1.49	1.52×10^{3}	3.73	-
	Bombus	Bumble bee	5.91×10^{-6}	4.70×10^{-3}	1.13×10^{-2}		3.58	1.93×10^{3}	2.79	0.238
Diptera	Tipula	Crane fly	3.35×10^{-6}	4.10×10^{-3}	1.66×10^{-2}	3.07	3.91	7.54×10^{2}	4.05	0.273
	Villa	Bee fly	3.71×10^{-6}	4.40×10^{-3}	1.34×10^{-2}		10.2	8.09×10^{2}	3.04	-
	Eristalis	Hover fly	3.79×10^{-6}	4.00×10^{-3}	1.13×10^{-2}		20.6	7.36×10^{2}	2.83	0.861
	Calliphora	Blowfly	1.23×10^{-6}	4.20×10^{-3}	9.40×10^{-3}		14.0	7.72×10^{2}	2.24	0.697
Lepidoptera	Manduca	Carolina sphinx	2.17×10^{-4}	2.17×10^{-2}	5.40×10^{-2}	3.03	2.31	3.94×10^{3}	2.49	0.450
	Ochlodes	Woodland skipper	2.56×10^{-6}	6.70×10^{-3}	1.30×10^{-2}		8.14	1.22×10^{3}	1.94	0.396
	Pieris	Cabbage white	1.18×10^{-5}	1.25×10^{-2}	2.16×10^{-2}		4.92	2.27×10^{3}	1.73	0.156

Based on the non-dimensional Euler-Bernoulli equation from Equation (A.5), a stiffness landscape can be produced as a function of the dimensionless stiffness Π_1 and density ratio ρ^*, as shown on the left-side of Figure A.1. Markers representing the approximate parameters exhibited by insects, birds, and swimmers are included, with the resulting time-trace of the tip amplitude (normalized by root amplitude) shown on the right of in Figure A.1. The particular magnitudes of the curves in this figure are also affected by the other dimensionless parameters presented at the beginning of this Appendix, however their general form remains the same. Utilizing only small changes in specific dimensionless stiffness Π_1 and density ratio ρ^*, the time-history of tip amplitudes can be made to collapse across all of this entire parameter space, as shown in Figure A.2.

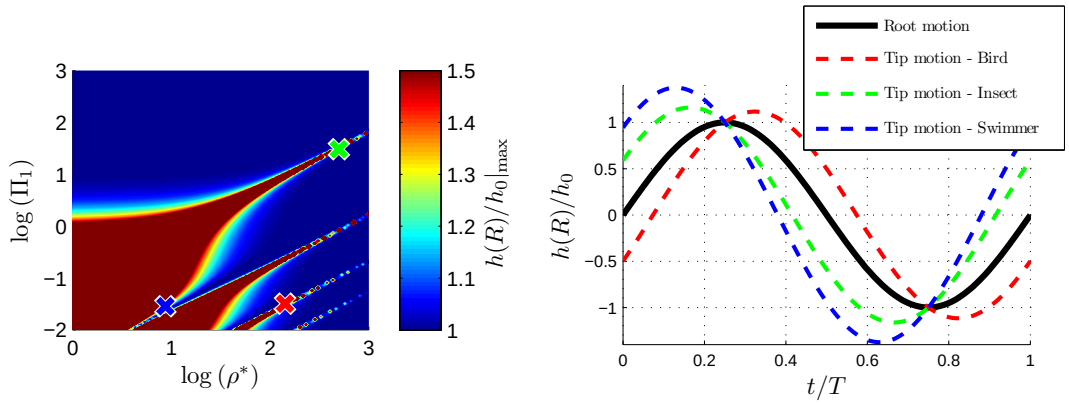

Figure A.1: The tip amplification can be parameterized in terms of dimensionless stiffness and density ratio, as shown on the left. Choosing stiffness and density ratios within the range of swimmers, birds, and insects, this tip amplification can be visualized by the tip path, shown on the right.

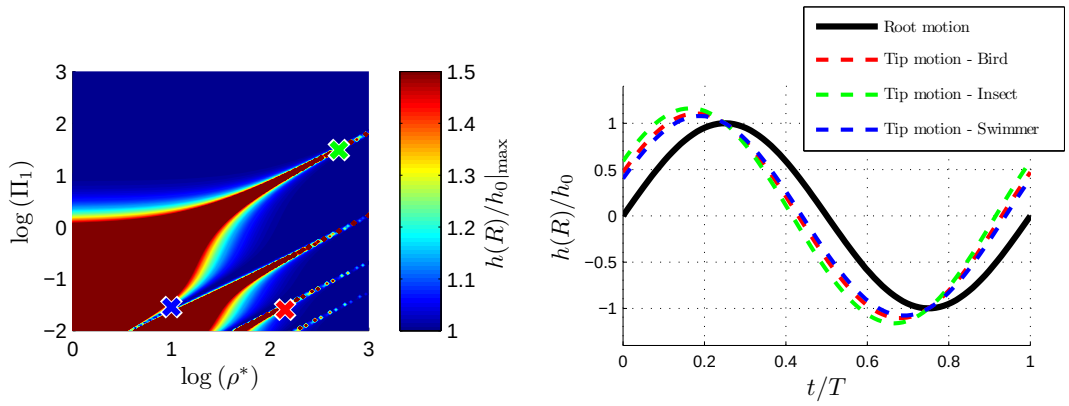

Figure A.2: Given the same stiffness landscape as in Figure A.1, small changes in the selection of stiffness and density can be chosen in order to collapse the resulting tip paths. Thus, regardless of the environment, it would be possible for animals to converge upon the same optimum gradient in effective incidence.

Appendix B

Comparing Optical Measurement Techniques

This thesis utilized a wide range of optical measurements, with frame rates ranging from 165 Hz to $10,000$ Hz, and measurement volumes ranging from $9E2$ mm^3 to $2E6$ mm^3. These volumes were selected based on the specific structures that needed to be captured. For instance, in the case of the PIV and PTV measurements in Chapter 2, both leading- and trailing-edge vorticity was to be captured on a 7.5 cm chord profile. This necessitated control volumes slightly larger than 7.5 cm. Meanwhile, the 30×30 mm^2 control volume for the PIV measurements in Chapter 6 needed to measure the fine-scale details of a separated shear layer, requiring a small control volume to maximize the spatial resolution of the camera sensor. To illustrate this optimization, the measurement systems used in each chapter have been compiled in Table B.1. Despite the large variation in frame rate and control volume, the pixel shifts of all systems are roughly similar, as this was the primary indicator used to determine frame rate. The slightly larger pixel shift used in the 3D-PTV measurements of Chapter 2 is due to the physically-limited frame rate of the cameras used in that study, which was accommodated for by using a lower particle seeding density.

Table B.1: Physical parameters of the optical measurement techniques used in this thesis.

Chapter	Technique	Frame Rate (Hz)	Resolution (px^2)	Control Volume	Re	Dimensional Velocity (m/s)	Particle Shift (px/frame)
2	3D-PTV	165	2560×1280	80×80×200 mm^3	7500	0.1	7.75
2	PIV	250	1024×1024	120×120 mm^2	7500	0.1	3.41
3	4D-PTV	1000	1024×1024	130×130×10 mm^3	100,000	0.3	2.36
4	4D-PTV	1000	1024×1024	130×130×10 mm^3	100,000	0.3	2.36
5	4D-PTV	900	1024×1024	100×100×30 mm^3	100,000	0.33	3.81
6	4D-PTV	1500	1024×1024	120×120×10 mm^3	250,000	0.833	4.74
6	PIV	10,000	1024×1024	30×30 mm^2	250,000	0.833	2.84